Blood and air flow multi-scale simulations based on real data

Irene Vignon-Clementel

▶ **To cite this version:**

Irene Vignon-Clementel. Blood and air flow multi-scale simulations based on real data. Biomechanics [physics.med-ph]. UPMC - Paris 6 Sorbonne Universités, 2016. tel-01418167

HAL Id: tel-01418167
https://inria.hal.science/tel-01418167

Submitted on 16 Dec 2016

HAL is a multi-disciplinary open access archive for the deposit and dissemination of scientific research documents, whether they are published or not. The documents may come from teaching and research institutions in France or abroad, or from public or private research centers.

L'archive ouverte pluridisciplinaire **HAL**, est destinée au dépôt et à la diffusion de documents scientifiques de niveau recherche, publiés ou non, émanant des établissements d'enseignement et de recherche français ou étrangers, des laboratoires publics ou privés.

Blood and air flow multi-scale simulations based on real data

Mémoire

présenté par

Irene E. Vignon-Clementel

en vue d'obtenir le diplôme

d'HABILITATION A DIRIGER DES RECHERCHES DE L' UNIVERSITÉ PIERRE ET MARIE CURIE

Spécialité : Mathématiques Appliquées

Soutenance publique le 31 mars 2016 devant le jury composé de :

Bertrand Maury, PhD	Rapporteur
Timothy Pedley, PhD	Rapporteur
Jean-Frédéric Gerbeau, PhD	
Pierre-Yves Lagrée, PhD	
Eric Vibert, MD, PhD	

Après avis favorables des rapporteurs: Bertrand Maury, Timothy Pedley et Alessandro Veneziani.

Acknowledgements

This journey in Biofluids started with Prof. Timothy Pedley (Cambridge University, UK). In his class in the Department of Applied Mathematics and Theoretical Physics I discovered how mathematical modeling could be a tool to understand physiological phenomena in health and disease. I was very honored when he accepted to be reviewer of this Habilitation and a jury member, after all these years.

Thanks to his recommendation, I did my PhD at Stanford University under Prof. Charles Taylor (at the time, in the Department of Mechanical Engineering and the Department of Surgery, then to the new Department of Bioengineering). I learned a lot in this multi-disciplinary environment. I first entered the field of Computational Mechanics. Through lab members, I was exposed to bioengineering. C. Taylor encouraged me to follow my interest for medical applications: I gained field experience by discussing with medical doctors of different specialties. In particular, I was very motivated by Dr. Feinstein's (Pediatric cardiologist, School of Medicine) 'questions to modelers', going to catheterization lab with him, to the radiological and surgical rooms with his colleagues, and attending clinical rounds. I thus would like to express my gratitude towards Charley and Jeff for having helped me to lay out the foundation of my work today, in between applied mathematics, bioengineering and medicine, and for continuing to support my work.

During my PhD, I started collaborating with colleagues, with whom I have continued to work, often through co-advising of students. I would like to thank them (in particular, A. Marsden now at Stanford University, S. Shadden now at UC Berkeley, and A. Figueroa now at U. of Michigan) for the opportunities it has given to me. For example exploring the new research field of respiration and particle transport. Through the associated team *Cardio* (INRIA-Stanford & former colleagues), I could link them to my environment in France, as a researcher at INRIA.

I joined the REO team-project at INRIA end of 2006. I am thankful to Jean-Frédéric Gerbeau, who created the team and believed in the expertise I could bring to the team. I value his leadership. We share a taste for working with the private sector. I have entered the respiratory and particle transport field with Céline Grandmont. May she be thanked for the shared opportunities. The other permanent members of REO also deserve a thankful mention for making a great team. I am also thankful to Dirk Drasdo, from MAMBA, who has seen our complementary strengths, and opened my eyes up to other research fields. Through him I met the surgeon Dr. Eric Vibert (Paul Brousse Hospital & INSERM), whose enthusiasm towards innovation has led me to new research grounds, closer to the bedside.

Collaborators from INRIA and at other institutions in France, Europe and the USA, have made this work truly multi-disciplinary and enriching. Too numerous to name, I trust they will recognize themselves. I am grateful for researchers whom paths I crossed and who have been supportive of my research, pushing the 'applied' part to real medical cases: Bertrand Maury (reviewer of this manuscript and jury member, U. Paris Sud), Alessandro Veneziani (reviewer of this manuscript, GeorgiaTech. U.), Pierre-Yves Lagrée (jury member, UPMC), Alfio Quarteroni (EPFL & Politecnico di Milano), Francesco Migliavacca (Politecnico di Milano), ...

This work was done with the power of younger minds. I have really enjoyed training and thinking with younger ones through postdocs, PhDs or internships - each student with her/his skills and character - and seeing them unfold each in their own paths.

Lastly, I am very grateful to my family, for their patience, support and care. In particular,

I would like to dedicate this manuscript to my late dad, who, although a literature major, always believed in and supported his first child in this scientific research track.

Contents

1 Introduction **1**

1.1 Cross-talk between mathematical models, numerical methods and biomedical applications . . . 2

1.2 Biomedical motivation: why modeling blood and air flow? . . . 3

1.2.1 Coupling of flow and growth . . . 3

1.2.2 Disease understanding . . . 3

1.2.3 Surgical planning . . . 5

1.2.4 Device design and optimization . . . 7

1.3 What do we need for an accurate analysis? . . . 7

2 Blood and air flow models at different scales **9**

2.1 Macro-scale flow modeling . . . 10

2.1.1 3D Navier-Stokes equations and fluid-structure interaction: the importance of boundary conditions . . . 11

2.1.2 1D equations of flow: wave propagation due to viscoelastic walls . . . 13

2.1.3 Reduced modeling of the entire system . . . 16

2.2 Tissue-scale (multiphysics) modeling . . . 19

2.2.1 Poromechanics: a different fluid-structure interaction model . . . 20

2.2.2 A poroelastic model valid for large strain . . . 20

2.2.3 Numerical results . . . 23

2.2.4 Conclusion . . . 26

2.3 Micro-scale flow modeling . . . 28

2.3.1 Tumor growth and angiogenesis modeling . . . 28

2.3.2 The multiscale model and numerical methods . . . 30

2.3.3 Numerical results . . . 31

2.3.4 Conclusion . . . 32

3 Numerical methods for multidomain coupling and instability treatment of multi-branched Navier-Stokes simulations **37**

3.1 Multidomain approaches . . . 38

3.1.1 3D model coupled to a 0D model of the heart and distal vasculature . 38

3.1.2 Predictability enhanced by 3D-closed loop model of the entire circulation 39

3.2 Numerical coupling strategies . . . 40

3.2.1 The multidomain formulation and its monolithic resolution . . . 40

3.2.2 A strongly coupled iterative multidomain formulation . . . 41

3.3 Analysis and handling of numerical instabilities . . . 44

3.3.1 Possible origins for boundary instabilities . . . 44

3.3.2 Comparison of numerical instability treatments . . . 45

3.3.3 A novel method: a modified Navier-Stokes equation . . . 48

4 Data-driven model parametrization **53**
4.1 Simplest model when data is scarce: application to better understanding of emphysema . . . 54
4.1.1 Parameter estimation for homogeneous emphysema . . . 54
4.1.2 Parameter estimation for heterogeneous emphysema . . . 59
4.2 Inverse problem for constant non-local targets - application to surgical planning in single ventricle physiology . . . 64
4.2.1 Parameter estimation for constant but distributed targets . . . 65
4.2.2 Results . . . 68
4.2.3 Discussion . . . 71
4.2.4 Application to surgical planning in single ventricle physiology . . . 71
4.3 Data assimilation for time-varying observations - applications to congenital heart diseases . . . 73
4.3.1 Data assimilation for time-varying observations . . . 73
4.3.2 Sensitivity analysis and model complement . . . 75
4.3.3 Loosely coupled 3D-0D strategy for coarctation pressure gradient estimation . . . 77
4.3.4 Perspectives . . . 79

5 Outlook **81**
5.1 Towards a better understanding of non-invasive imaging data: parameter estimation of which model? . . . 82
5.2 Modeling a new area: surgical planning in liver . . . 83
5.3 Hybrid modeling for lung disease understanding . . . 83
5.4 Validation and uncertainty quantification . . . 84
5.5 Conclusion . . . 86

"Work in physiological fluid dynamics needs very close and intimate collaboration between specialists in physiological science and specialists in the dynamics of fluids. The necessary collaboration has to be preceded by a process of mutual education sufficiently prolonged to bring about on each side an adequate understanding of the other side's language and modes of expression, as well as recognition of which are the main areas where the other discipline has developed a particularly extensive and intricate body of knowledge and skills which can be called upon when required. After this, real communication between the different specialisms becomes possible, and can lead to effective research progress."

Sir James Lighthill [Lighthill, 1975].

1 Introduction

This work is the result of 10 years of collaboration with clinicians. It is an attempt to both *bring about [...] an adequate understanding of the other side's language* and to bring new bricks into the *intricate body of knowledge and skills* necessary for *effective research progress* [Lighthill, 1975]. Medicine itself is a science that is increasingly becoming quantitative. This new direction calls for sophisticated mathematical models and engineering approaches to unearth deep (patho-)physiological understanding and propose targeted interventions. Such development is supported by recent progress in data acquisition in medicine and biology.

1.1 Cross-talk between mathematical models, numerical methods and biomedical applications

The contribution of my work is to bridge frontiers between applied mathematics, bioengineering and biology or medicine. The interactions between these different components are both interesting and challenging. They are challenging, as the fluid mechanics of the application is sometimes so complex that existing numerical methods to solve e.g. the Navier-Stokes equations may be insufficient and necessitate targeted numerical developments (chap. 3). Also the hemo/respiratory in vivo data may not have been acquired with a precision that is high enough to impose coherent boundary conditions in fluid simulations (chap. 4). They are interesting in the sense that applications can drive the development of numerical methods. E.g. blood flow simulations in patient specific geometries and under physiological conditions often led to numerical divergence ten years ago. Ad-hoc strategies first palliated the problem, such as adding more or longer vessels. However this was not always desirable (increase of computational time) or possible (image data resolution), and thus this led the numerical community to revisit stability analysis and stabilization strategies in this context (chap. 3). The physiologically realistic respiratory flow simulations that appeared a few years later than in blood flow, further demonstrated this numerical need. The numerical handling of such complexity in turn made possible for me to simulate pathophysiological conditions that would not have been possible otherwise (chap. 4).

In other words, a characteristic of this work is that it is a *dynamic loop*. The starting point is the goal of answering a biomedical question. This drives the development of mathematical models or numerical tools (applied mathematics/computational mechanics). They are then transferred to the specific application (selection of relevant parameters, inputs from real data, generation of first answer to the biomedical question - bioengineering aspect) to a point where the biomedical question can be addressed (robustness of results assessed based on multiple cases - medicine/biology), thus closing the loop. In this context, my contributions involve adapting or developing models of blood and airflow, at different scales or degrees of precision (chap 2): 3D Navier-Stokes for flow in large conduits, 3D poroelastic formulation compatible with large strain for heart perfusion, 1D equations of blood flow, 0D electric analog for macro or micro-circulation of blood and for respiratory mechanics. Moreover, I have worked on developing numerical methods that are necessary to couple these different models (multidomain or multiscale coupling, with monolithic or robust iterative strategies) and to handle instabilities (contributions in numerical instability analysis, treatment - with or without stabilization - and comparison of different methods, chap. 3). I have also devised strategies to parameterize models from real experimental (animal) or clinical data (depending on the type and amount of data available, based on variational or Kalman filter approaches - chap. 4). Each time, these models and methods are illustrated by a specific biomedical application (contributions in applying these numerical methods to circulation understanding of systemic, in particular coronary, and pulmonary blood circulations, to surgical planning and device design for several congenital heart diseases, to better understanding of emphysema airflow and particle transport in the lung). At the microscale level, my contribution is in the coupling of multiphysics/multiscale systems for modeling the dynamic interplay between

tumor cells and their environment, which includes blood perfusion. The manuscript ends with an outlook on topics that necessitate further research (chap 5).

This work could not have been done without collaboration with students and colleagues in Applied Mathematics/Engineering from INRIA (REO, MAMBA, M3DSIM, Asclepios), from the USA (Stanford U., U. of California Berkeley, U. of California San Diego, U. of Michigan, Cornell U.), UK (UCL), Italy (Politecnico di Milano) and Germany (DKFZ/Heidelberg U., Leipzig U.), and with medical doctors from France (Necker-Enfants Malades hop., Paul Brousse hosp.), Germany (Thorax Klinik Heidelberg, U. Heidelberg Clinics), UK (GOSH), the USA (Lucile Packard Children's Hospital Stanford, MUSC, U. of Michigan Health System). The names of these colleagues appear in the cited references. For non-published work, individuals are listed. Funding sources are also gratefully acknowledged in the references and here for work in progress. They include: Whitaker foundation, NSF (American national science foundation), American Heart Association, Fondation Leducq, INRIA national and international seed funding, France-Stanford Center for Interdisciplinary Studies, BMBF (German national research agency), ANR (French national research agency).

1.2 Biomedical motivation: why modeling blood and air flow?

Flow is interesting to model because of its mechanistic link to biological or medical aspects. In biofluids, a traditional example which has become a matter of vascular biology research, is the one of endothelial cells (cells lining blood vessels): if exposed to higher shear, they elongate in the direction of flow, have an increased barrier integrity, and change their gene expression [Kamiya and Togawa, 1980, Levesque and Nerem, 1985, Abaci et al., 2014]. These modifications have important implications for disease understanding and treatment in cardiovascular (atherosclerosis) and cancer research. In the next sections, we show several examples of how blood and air flows are intimately linked to tissue growth and disease understanding (sections 1.2.1 and 1.2.2). Moreover we explain why their study can be a basis for surgical planning (section 1.2.3) and device design (section 1.2.4).

1.2.1 Coupling of flow and growth

Embryo development (morphogenesis in tetrapods) has been proposed to be the result of vortices formation [Fleury, 2012]. Vasculogenesis, the formation of the heart and primitive blood vessels, and angiogenesis, the remodeling and expansion of the existing network of blood vessels during or after development [Patan, 2004], are also thought to be the outcome of inner flow, flow demand and tissue biomechanics forces [Boselli et al., 2015, Lindsey et al., 2014a]. The normal human blood circulation is shown in fig. 1.1. Abnormal vasculogenesis of the precursor arteries is associated with over 50% of clinically presented congenital heart defects [Go et al., 2013] (see fig. 1.4). These defects are among the most severe congenital abnormalities [Pradat et al., 2003], accounting for nearly 30% of deaths from developmental abnormalities in the USA [Lloyd-Jones et al., 2010]. Yet their etiology remains to be fully understood in order to prevent or palliate them. Even though chick embryo experiments of flow perturbation lead to altered vasculogenesis [Yashiro et al., 2007, Nomura-Kitabayashi et al., 2009, Lindsey et al., 2014a], the hemodynamics triggers to these alterations still need to be unraveled. Blood flow simulations in normal and occluded aortic arches may help shed some light on this question (see fig. 1.2 for our ongoing work with Stephanie Lindsey coadvised with Jonathan Butcher (Cornell U.), following [Lindsey et al., 2014b]). Coupling of flow and growth is further discussed in the context of vascularized tumor modeling (section 2.3).

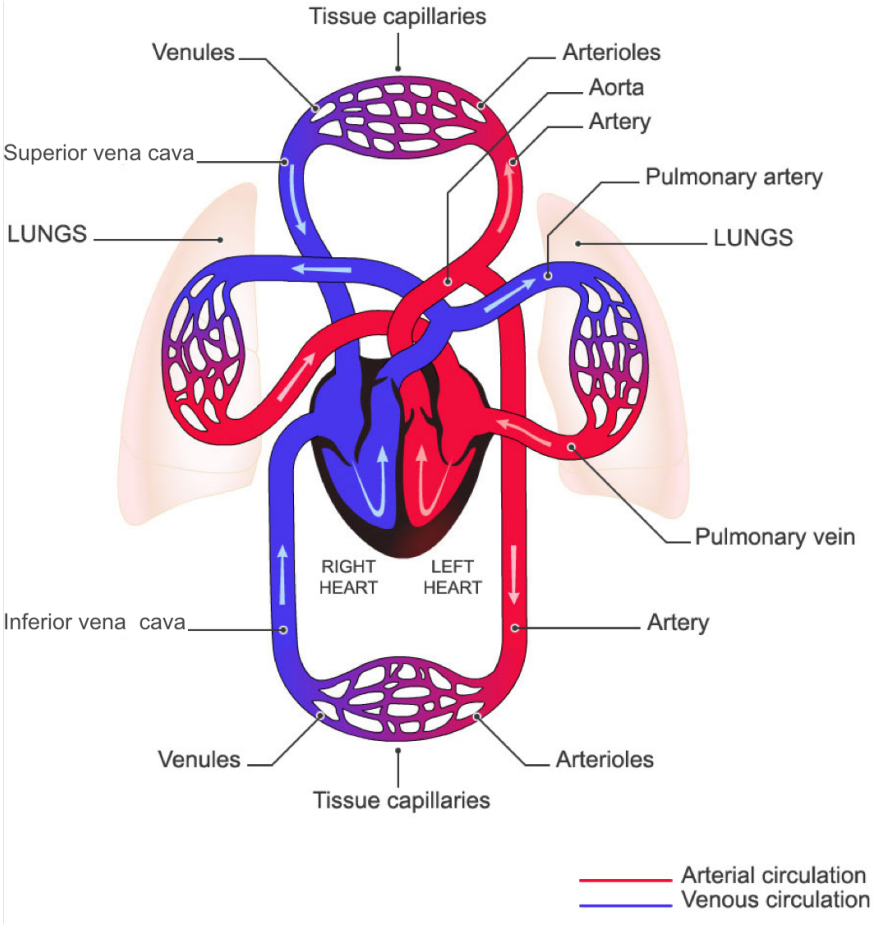

Figure 1.1: Normal human blood circulation (direction given by arrows), with the four heart chambers, the main arteries (oxygen rich blood = red) and veins (oxygen poor blood - blue), and the branching into vascular trees leading to capillary beds where functional exchanges occur. Adapted from `http://www.urgo.co.uk/260-the-venous-system-within-the-cardiovascular-system`. The time-scale of the heart-beat is 1s in an adult at rest. The ventricles muscle contracts and blood is expelled from the ventricles into the aorta and the main pulmonary artery during systole; when the valves in-between close, diastole begins and blood fills in the ventricles.

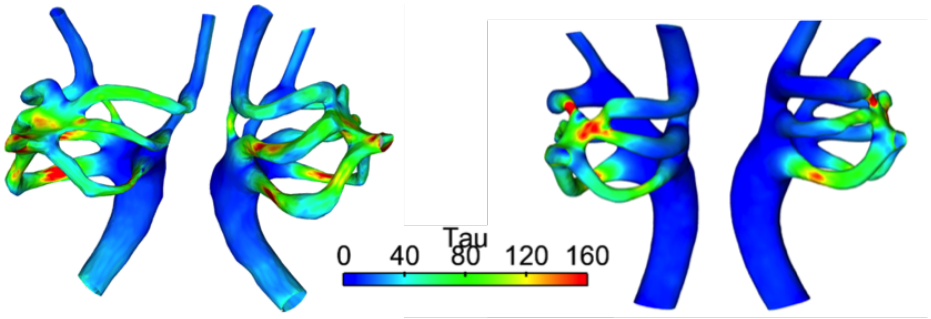

Figure 1.2: Wall shear stress in dyn/cm^2 computed in normal (left) versus one day after occlusion of the IVth right arch (right) chick embryo pharyngeal aortic arches (precursor to great arteries).

1.2.2 Disease understanding

In vascular biology, it has been shown that flow modulates diameter [Lee and Langille, 1991, Kamiya and Togawa, 1980] and pressure controls wall thickness [Wolinsky and Glagov, 1969]. These mechanisms entail vascular adaptation to functional changes or demands. However, they can also promote disease progression. Computational fluid dynamics (CFD) is a complementary tool to in-vitro or in-vivo experiments to better understand the link between hemodynamics and disease development. For example in [1], we have seen a decrease of infrarenal aortic wall shear stress in spinal cord injury patients compared to normal subjects, that may explain why these patients are more prone to abdominal aneurysm development. Similarly, the fact that their legs atrophy, and consequently their downstream arterial impedance changes is likely to favor aneurysm development due to the computed sustained high pressure during the cardiac cycle. These two factors, which are the results of computer simulations, would not have been easily measured in patients. Note that such simulations can only be carried out if appropriate boundary conditions are used (see sections 2.1.1, 2.1.2, 3.1).

An example in respiratory flow of how CFD can shed light on diseases, is the one of particle fate in emphysematous ventilation. This disease is characterized in part by expanded alveoli volume (fig. 1.3) and enlarged tissue compliance [Thurlbeck and Muller, 1994]. Empirical models, in-vitro experiments and in-vivo data give conflicting information on impact of the disease for aerosol deposition in the lungs. Numerical simulations of air flow and particle transport and deposition in rat airways have shown the asynchronous breathing dynamics between normal and diseased regions, and that emphysematous regions are more ventilated and thus delivered more particles during inspiration (see section 4.1).

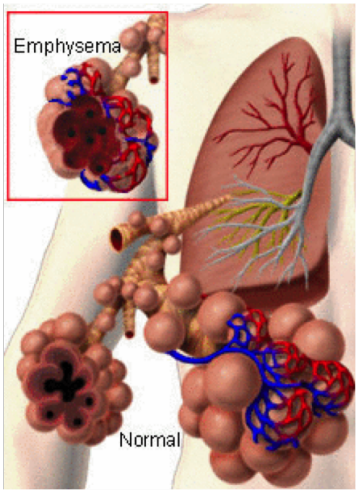

Figure 1.3: The respiratory system of mammals. During inspiration (∼2s for an adult patient at rest), air goes into the lung through the trachea that branches into smaller and smaller airways in the different lung zones, called *lobes*. The smaller airways lead to the functional units, the compliant balloons called *alveoli*. In expiration (∼3s for an adult patient at rest), air goes out in the reverse direction. In emphysema, alveoli volume is increased due to inner wall damage, leading to reduced exchange surface with the blood. From `http://www.pdrhealth.com/patient_education`.

These two cases are examples among many studies that have been carried out in the biofluid dynamics community to explain underlying mechanisms to disease symptoms and progression (e.g. [Olufsen et al., 2012, Kheyfets et al., 2013, Sanchez et al., 2014, Milner et al., 1998, Taylor et al., 1998a, Peeters et al., 2015] [2]). This field has especially focused on understanding acquired cardiovascular diseases, i.e. diseases that develop after birth, in contrast with congenital heart diseases (CHD) which revenue market is much smaller. Yet, better treating these diseases can affect patients for a lifetime.

1.2.3 Surgical planning

Single ventricle physiology (SV), e.g. hypoplastic left heart (see fig. 1.4) or tricuspid atresia, is one of the most complex and least understood forms of CHD. These babies are born with only one functional pump in the heart and require the systemic and pulmonary circulations to be placed in series through several operations performed during early childhood (see fig. 1.4).

The first operation, the Norwood procedure, replaces the neonatal ductus arteriosus with a stable source of pulmonary blood flow and insures unrestricted flow from the single ventricle to the aorta (studied in sections 2.1.3, 3.3.3, 4.2, 4.3). The second of three stages in the usual palliative approach, the cavopulmonary connection or Glenn procedure involves disconnecting the superior vena cava (SVC), which drains oxygen-poor blood of the upper body, from the right atrium and connecting it directly to the pulmonary circulation, namely to the right pulmonary artery (RPA) (studied in section 4.2). However, the proportion of systemic venous return from the lower body increases with age. The generally final operation, the total cavopulmonary connection (TCPC) or Fontan procedure, connects then the inferior vena cava (IVC) directly to the pulmonary arteries as well (studied in section 2.1.1). These connections form artificial junctions. As flow to the lungs is then passive in nature, optimal architecture and physiology are paramount for successful long-term clinical outcomes. Despite the increasing effort in trying to understand the physiology at each stage, reasons why the procedures fail or succeed are still not clear [DeGroff, 2008]. Furthermore, even if the surgical procedures and patient management have much improved the prognosis of the patients, significant morbidities still remain, such as arrythmias, exercise intolerance, pulmonary thrombotic events, liver dysfunction, heart failure, etc. [de Leval and Deanfield, 2010].

Physicians have expressed the need for a better understanding of the hemodynamic conditions in subjects with congenital heart defects, pre- and postoperatively. Experimental, clinical and numerical methods have been used to study different aspects of the anatomic and physiologic conditions [Taylor and Figueroa, 2009, Taylor and Steinman, 2010], before and after interventions (see [DeGroff, 2008] for a comprehensive review of these different techniques developed over the last decades to study this multistage procedure, and references therein). Integrating patient specific clinical information into numerical simulations is critical to yield results which accurately represent a patient's specific condition as we have shown e.g. in [3]. Predictive modeling for surgical planning has first been demonstrated in [3] for a Fontan patient: pressure in the SVC, which if too high can lead to cognitive development issues, has been well predicted. Prediction of clinically critical hemodynamics quantities however is still in its infancy. Moreover each surgical stage described above can be in fact performed in different ways, which are matter of clinical debate (fig. 1.4). The power of simulation is here its ability to test different surgical options, which obviously is not possible on a patient [4].

1.2.4 Device design and optimization

Previous studies have demonstrated that the artificial graft geometry and anastomosis shape play an important role in Fontan hemodynamics. A novel Y-shaped design was proposed to improve upon traditional designs, and results have shown promising hemodynamics [Marsden et al., 2009]. Multidomain simulations (section 3.1) have permitted us to study how geometry and boundary conditions affect the performance of these virtual surgical designs under rest and exercise conditions [5]. In particular, we have investigated if and how the IVC flow (which contains an important biological factor from the liver) can be optimally distributed among both lungs [6]. This Y design has been successfully implanted on patients in a pilot study at Stanford Children's hospital [Martin et al., 2015].

The effect of implanted device is also studied by subject-specific CFD [Bazilevs et al., 2009a, Prasad et al., 2013, Caputo et al., 2013, Auricchio et al., 2014]. More generally, device design is increasingly performed with CFD and fracture simulations. The Food and Drug Administration is integrating computational modeling into its evaluation and testing processes with increasing frequency and mandate [Stewart, 2008]. The European Council is currently working on a Medical Device text that includes requirement of modeling and simulation for market authorization [euR, 2015]. In this context, we have recently predicted hemodynamics changes due to a new device that has only been tested in animals, in a Tetralogy of Fallot patient, another important CHD [7] (fig. 1.5). We hope such

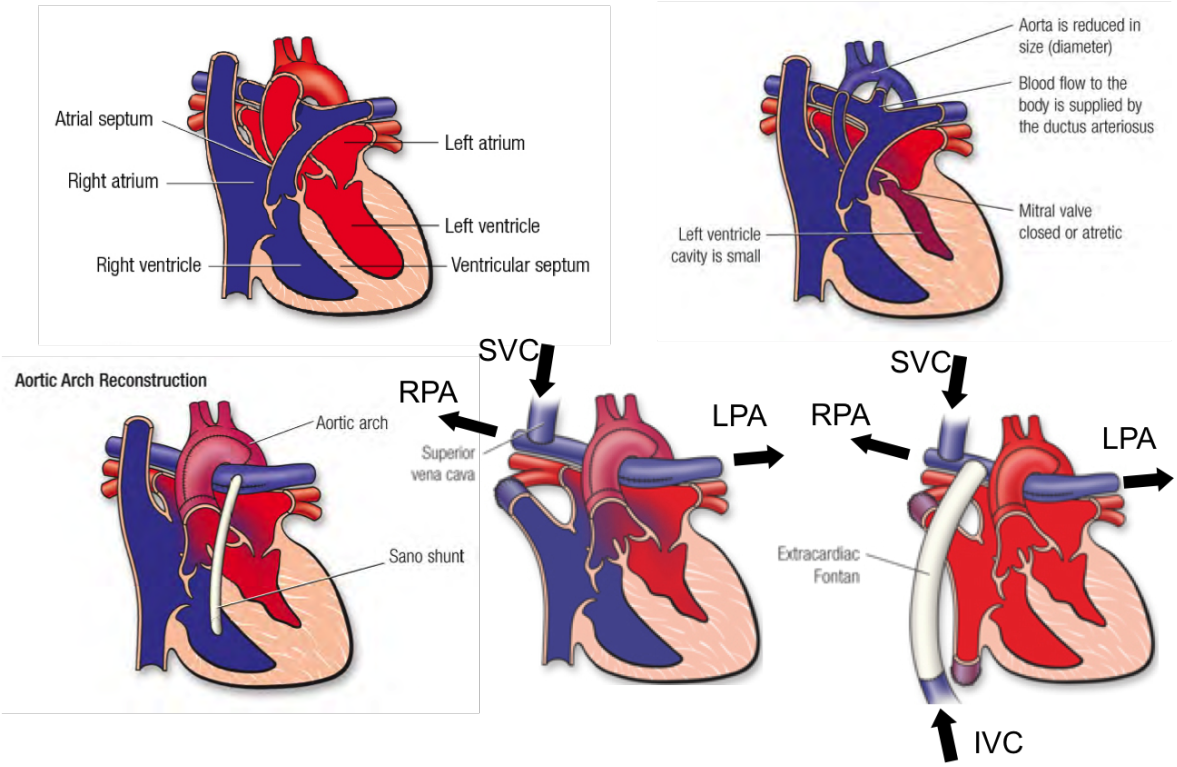

Figure 1.4: Top: normal heart and heart with congenital defect (here HLHS). Bottom: the 3 surgical stages. Stage 1: Norwood palliation with Sano (shown here) or Blalock-Taussig shunt, stage 2: Glenn (shown here) or Hemi-Fontan conversion, stage 3: Extra-cardiac (shown here) or lateral tunnel Fontan conversion. The lower-oxygen content blood is in blue, while the higher-oxygen content blood is in red. Pale pink indicates the heart muscle, the myocardium. From `http://www.heart.org`.

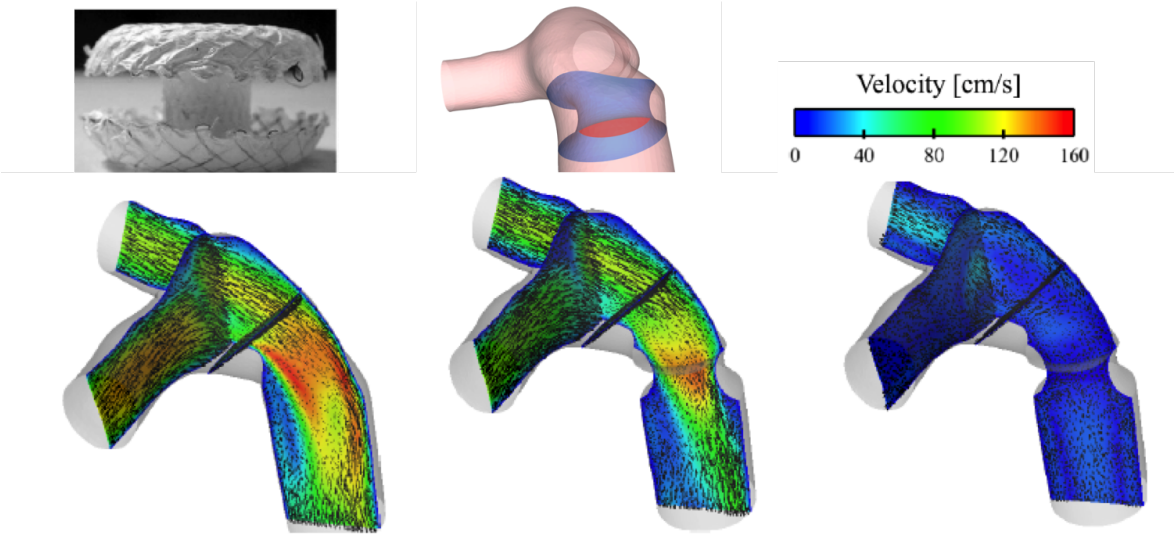

Figure 1.5: Top: new device (percutaneous valved reducer), geometrical model, velocity magnitude scale. Bottom: diastolic computed velocity without the device (left, strong regurgitation), with the reducer only (middle, lower regurgitation), with the full device (right, no regurgitation).

simulations can help design device before clinical testing.

1.3 What do we need for an accurate analysis?

We have shown above why simulating blood and air flow is interesting. The question is then how to do it, and what it means to perform an accurate analysis. The use of computational simulation to examine common clinical problems is more and more appearing in clinical journals. In practice, such collaboration can only work if both communities understand each other's methods and their limitations. Thus, we have written an article in a clinical journal [3], intended to facilitate this communication by presenting, in the context of CHD, the main steps involved in performing computational simulation - from the selection of an appropriate clinical question/problem to the understanding of computational results, and all of the *black boxes* in between. An important step is the selection of mathematical models that are appropriately refined given the question at hand, for the flow and its interacting components (muscle, device, cells, molecules, etc.) [D'Angelo et al., 2011] [8]. This paper [3] thus describes the main steps of a successful collaboration, presenting state of the art simulation tools and clinical data incorporation. Although conceptually more general, this article is illustrated by (at the time) novel predictive computer simulations in congenital heart disease.

A second question that emerged from collaboration with clinicians, pertains to the choice of these black boxes. Commercially developed numerical codes have increased the availability of such tools to a wider range of research, design, and clinical users. In parallel, but independently, a number of research specific codes have been developed, some of which have been made available as open sources. A few studies [Pekkan et al., 2005] [9], *benchmarks* [Stewart, 2008, Boileau et al., 2015] and *simulation challenges* [Radaellia et al., 2008, cha, , Steinman et al., 2013] have thus emerged to compare codes or simulation approaches to ascertain the validity and accuracy of these various codes for a specific application. To achieve effective solution, there are several necessary steps to numerically simulate blood or air flow:

- geometry definition (from image data when possible), which leads to different components/compartments (for ODE models) or geometrical mesh generation including mesh adaptation (for PDE models) (see fig. 1.6)
- choice of driving terms or boundary conditions
- choice of numerical algorithm to solve the equations

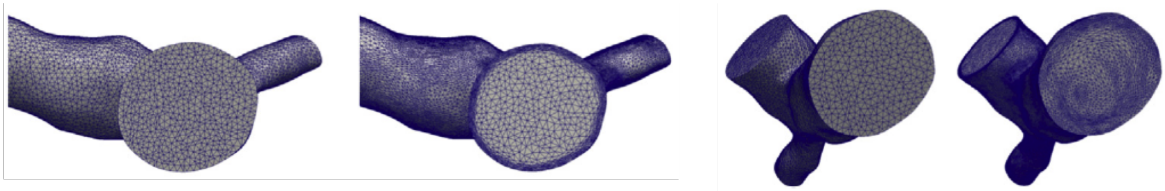

Figure 1.6: Examples of mesh adaptation: isometric inlet (1rst) and outlet (3rd) meshes, and corresponding adapted meshes to a thin boundary layer profile (2nd) and a complex swirling flow (4th) [9].

These steps will be defined in the next chapter according to the model at hand. Any misstep or inaccurate performance along the simulation algorithm can lead to erroneous results and potentially misleading conclusions. Therefore, we sought to systematically examine the choices of each of these step to assess whether the choice of solver code remains an important determinant on the reliability and accuracy of the solution [9]. We have demonstrated the

importance of defining accurate boundary conditions as a prerequisite for accurate simulation [3]. The main conclusions are the following [9]. The precise setup of the numerical cases has more influence on the results than the choice of numerical codes. The need for detailed construction of the numerical model that requires high computational cost depends on the precision needed to answer the biomedical question at hand and should be assessed for each problem on a combination of clinically relevant geometry and physiological conditions.

2

Blood and air flow models at different scales

The objective of this chapter is to present fluid dynamics models of cardiovascular (fig. 1.1) and respiratory (fig. 1.3) flows at different scales, to which I contributed in developments or simulations. Blood and air flow through an architecture of branching networks from larger to smaller conduits (arterial side, inspiration), arrive to micro-units designed to ensure proper functioning of the body (capillaries, alveoli), and flow back from small to large conduits (venous side, expiration) into a pressure chamber (the heart, outside air). Numerical simulations shed light on some deregulations in order to better palliate them (see sections 1, 4). Flow in the larger conduits can be modeled in detail by Navier-Stokes equations solved in 3D domains reconstructed from non invasive patient-imaging data, possibly with fluid-solid interaction of the conduit. Section 2.1.1 highlights in particular the importance of boundary conditions. The integration of these equations over a cross-section gives rise to the so called *1D equations* (PDEs). Although they cannot model the detailed 3D structure of the flow, their advantages are that less geometrical information is needed and they can capture wave-propagation phenomena and fluid dynamics over a more extended domain, owing to their lighter simulation costs. Section 2.1.2 presents this model, including the effect of vessel wall viscoelasticity. A further integration over the axial dimension leads to the so called *lumped models* or *0D models*, a system of ODEs describing air or blood flow with electric analogy. Spatial differences are only represented by the number of *compartments*. But these models are fast to solve. They can thus represent the time dynamics of the entire blood circulation, including different organs and heart chambers, or of the entire respiratory system, including the effects of the elastic tissues and diaphragm. Section 2.1.3 illustrates blood circulation and respiratory models of varying complexity.

The models above are usually referred to as *macro-scale models* since they describe flow or fluid-solid interaction in large conduits or their effect at the organ or body scale. However, to better understand organ perfusion, i.e. the delivery of blood and what it transports through the vascular trees of the tissue, porous media models are sometimes favored. These 'sponge-like' models describe at the *mesoscale* how blood flows through a tissue, without explicitly representing the geometry of each vessel. Poroelasticity takes into account the fluid interaction with the elastic tissue but each constitutes a different *phase* of the tissue seen as a continuum. Section 2.2 describes the development of such a perfusion model valid for large strain in the beating heart. In respiratory modeling the effect of air in alveoli connected within the parenchyma, i.e. lung tissue, by the respiratory tree has been taken into account via explicitly or effectively poroelastic tissue models [Berger et al., 2015, Cazeaux and Grandmont, 2015].

Finally, *microcirculation* of the blood is sometimes necessary to model due to its cross-talk with tissue cells, e.g. in the understanding, diagnosis or treatment of cancer. Since spatial gradients play a role, vessels are explicitly represented but with statistically representative distributions. Cells are also explicitly represented, but molecular scales are treated with continuum reaction-diffusion models. An example of such a system is presented in section 2.3.

2.1 Macro-scale flow modeling

The macro-scale flow models mentioned above are defined more precisely in this section. Each type (3D, 1D, 0D) has been the matter of numerous works. In model derivation and mathematical/fluid-mechanics study, this has been the case particularly for 1D models of blood flow since the '60s [Barnard et al., 1966, Anliker et al., 1971, Hughes and Lubliner, 1973, Pedley, 1980] after the seminal work of Womersley [Womersley, 1955] and Lambert [Lambert, 1958]. In numerical analysis, the question of boundary conditions at artificial boundaries for Stokes or Navier-Stokes equations in different formulations has been studied in the '90s [Heywood et al., 1996, Begue et al., 1988, Bruneau and Fabrie, 1994]. 3D blood flow simulations started to emerge as a field then, and

very rapidly led to revisit this question since patient-data gives rise to defectuous boundary conditions. To take into account the rest of the circulation in modeling flow in the domain of interest emerged as a need to achieve physiological simulations: this lead to numerous numerical analysis works on *multi scale* or *multidomain* coupling of 3D or 1D models with reduced models (1D or 0D), both in terms of coupling conditions and stable and efficient algorithms (see sections 3.1, 3.2). Numerical instabilities due to complex flow have become more crucial to tackle for both patient-specific hemodynamics modeling and respiratory modeling, and matter of intense research in the last 10 years (see section 3.3). In the meantime, 1D and 0D models have begun to answer clinical questions based on patient data [Ottesen et al., 2013, Bode et al., 2012], driving the field into parameter estimation (see section 4) and inclusion of larger time-scale phenomena than the heart or respiratory beat (see section 5). For more complete recent perspectives on these models for blood flow see e.g. [Nichols et al., 2011, Formaggia et al., 2010] and for respiratory flow see e.g. [Bates, 2009, Maury, 2013].

2.1.1 3D Navier-Stokes equations and fluid-structure interaction: the importance of boundary conditions

The simplest three-dimensional description of blood flow only considers the fluid motion as an internal flow in a rigid solid, the wall, where a no-slip condition is applied if the fluid is considered as viscous (which is generally the case for blood flow) [10, 11]. We refer to [12, 13] for the extension to fluid-solid interaction at that level. Blood is besides assumed to be a Newtonian fluid. The incompressible Navier-Stokes equations are thus solved in the domain Ω_1 with no-slip condition on the wall Γ and with a Dirichlet boundary condition on the velocity at the inlet Γ_{in} (the notation is defined in Figure 2.1):

$$\rho\frac{\partial \boldsymbol{u}}{\partial t} + \rho(\boldsymbol{u}\cdot\nabla\boldsymbol{u}) + \nabla p - 2\mu\nabla\cdot\boldsymbol{\varepsilon}(\boldsymbol{u}) = 0 \tag{2.1}$$

$$\nabla\cdot\boldsymbol{u} = 0 \tag{2.2}$$

$$\boldsymbol{u}_{|\Gamma} = 0 \tag{2.3}$$

$$\boldsymbol{u}_{|\Gamma_{\text{in}}} = \boldsymbol{u}_{\text{in}} \tag{2.4}$$

where $\boldsymbol{u} : \Omega_1 \times \mathbb{R}^+ \to \mathbb{R}^3$ is the velocity, $p : \Omega_1 \times \mathbb{R}^+ \to \mathbb{R}$ is the pressure, and $\boldsymbol{\varepsilon}(\boldsymbol{u}) = \frac{1}{2}(\nabla\boldsymbol{u} + \nabla\boldsymbol{u}^T)$ denotes the strain rate tensor. The initial conditions for this problem are given by a divergence free velocity vector field.

Here the names 'inlet' and 'outlet' are chosen for convenience, but any of these can have some positive or negative flow rate over time. They can each refer to a single planar conduit face or a set of them. We refer to [3] for different ways of defining $\boldsymbol{u}_{\text{in}}$ based on the available clinical or experimental data (PC-MRI flow data, ultra-sound Doppler velocity data, etc.). The system (2.1)-(2.4) has to be complemented with boundary conditions at the outlet Γ_{out} which take into account the rest of the vessels.

Remarkable progress has been made in simulating blood flow in realistic anatomical models constructed from three-dimensional medical imaging data. Arguably, accurate anatomic models are of primary importance in simulating blood flow. However, as we demonstrate in [11], realistic boundary conditions are equally important in computing velocity and pressure fields. Yet, at the time this subject has received far less attention than image-based model construction for three-dimensional simulations. Three-dimensional numerical methods have been used to compute velocity fields and quantify shear forces acting on the surface of blood vessels. However, since most three-dimensional models of blood flow use zero or constant pressure, zero traction, or prescribed velocity profiles as outlet boundary conditions, blood pressure is not computed accurately and notably absent from reports of hemodynamic investigations. For simulations of blood flow in large arteries, the outlet boundary conditions

represent the downstream vasculature including smaller arteries, arterioles, capillaries, venules and veins returning blood to the heart. Clearly, the vast extent and complexity of the circulation precludes a three-dimensional representation of the entire circuit, yet ignoring the effect of the downstream circulation results in grossly inaccurate predictions of velocity and pressure fields for many problems where the distribution of flow between the major arteries is unknown. If equal pressures or tractions are used for different outlets, the flow split is dictated solely by the resistance to flow in the domain of interest, neglecting the effect of the resistance or flow demands of the downstream vascular beds. In most cases, this effect is however dominant. An alternative approach is to utilize 3D models for the major arteries where high-fidelity information is needed, and reduced order models to represent the remainder of the system (see sections 3.1 and 4 for modeling aspects and 3.3.3 for typical Navier-Stokes Neumann boundary conditions).

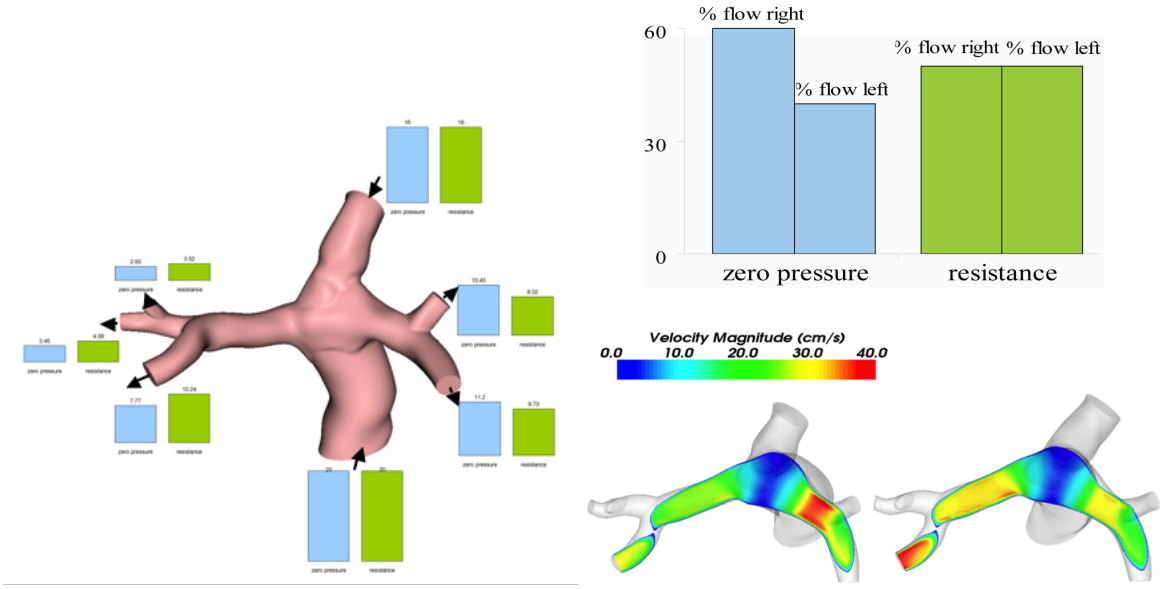

Figure 2.2: Left: detailed inflow and outflow distributions for homogeneous pressure (blue) versus resistance (green) PA outlet boundary conditions. Arrows indicate the direction of blood. Velocity is prescribed on the 2 inlets (SVC and IVC). Right: overall lung flow distribution (top) and corresponding velocity magnitude for (bottom left) zero pressure and (bottom right) resistance outlet boundary conditions [3].

We illustrate the importance of boundary condition on a Fontan patient case (see section 1.2.3 and fig. 1.4). The resulting geometry in the shape of a 'cross' is peculiar for the cardiovascular system: flows from the two venae-cavae merge and get distributed into the two pulmonary trees, sometimes creating very complex flow and unique hemodynamics that are at the time of [10, 14, 3] not well understood. In this context, we analyze the influence of different boundary conditions on flow and pressure. First, let us compare the zero pressure boundary condition case to a simulation where resistances (defined in section 2.1.3) are prescribed at each outlet proportional to their areas, enforcing a 50%/50% flow distribution between the two lungs. The simulations are run with rigid wall and steady input flows based on MRI data [3]. Despite the fact that this is a resting, steady regime, the resulting flow distribution between the left and the right lungs varies significantly with the type of boundary condition, as shown in fig. 2.2. Patient-specific blood flow distribution cannot be taken into account when imposing the same pressure at all the outlets. Furthermore, this has a direct impact on the velocity field (see fig. 2.2), and thus on the wall shear stress, as well as on the level of pressure in the system (which is particularly important for fluid-solid interaction applications) and the energy losses. This example illustrates the impact of outlet boundary conditions, but several studies

have also demonstrated that taking into account the (cardiac [Shandas, 2002] or respiratory [14]) pulsatility of the inflow as opposed to prescribing a steady value also significantly affects the results. For our more thorough study of boundary conditions impact, we refer to the paper [11] for pressure, resistance and impedance boundary conditions in blood flow, [13] for Windkessel boundary conditions in hemodynamics FSI simulations considering periodic assumption versus fully transient phenomena emerging from natural heart-rate variability or flow complexity in restricted geometries, and [15] comparing RC versus homogeneous constant pressure for respiratory flows. All these outlet reduced models are defined in section 2.1.3.

In terms of formulation, although in this thesis (and in most cited articles), the advective form has been primarily used, the conservative form has also been tested for multidomain coupling in [11] as well as other formulations for the natural emergence of different Neumann boundary conditions [16]. Numerically, it is only with the development of computer methods that the three-dimensional equations have been solved in their generality, i.e. for both steady and pulsatile flow, in single tubes, bifurcations and patient-specific complex multi-branched geometrical models, for rigid and then moving walls. Finite-volume methods (e.g. [Lagana et al., 2005] or other articles using commercial codes such as ANSYS CFX, ANSYS Fluent) have been widely used to discretize the spatial domain, especially for fluid simulations in simple domains, in conjunction with standard time-integration methods. Finite element methods have been used for both fluid and solid discretizations, in space e.g. [Perktold and Rappitsch, 1995, Lagana et al., 2002, Cebral et al., 2003, Taylor et al., 1998b, Moore et al., 1999, Stuhne and Steinman, 2004, Quarteroni et al., 2000, Gerbeau et al., 2005] or in space and time [Torii et al., 2006]. In this work - except when the commercial code Fluent is indicated (e.g. in [9]), stabilized finite element methods have been used either in the code PHASTA (see references and complete formulation in [11]) that is included in the open source code Simvascular [Schmidt et al., 2008, sim, 2015], or in the code FELiScE [fel,] [17]. Adaptative meshing has also been generally necessary for the different applications, particularly when flow is complex, such as in multi branched geometries [9]: MeshSim [Muller et al., 2005, Sahni et al., 2006] has been used with PHASTA (e.g. [13, 18, 9, 19]) and *feflo* [Loseille and Löhner, 2010] has been used with FELiScE [16, 17, 20].

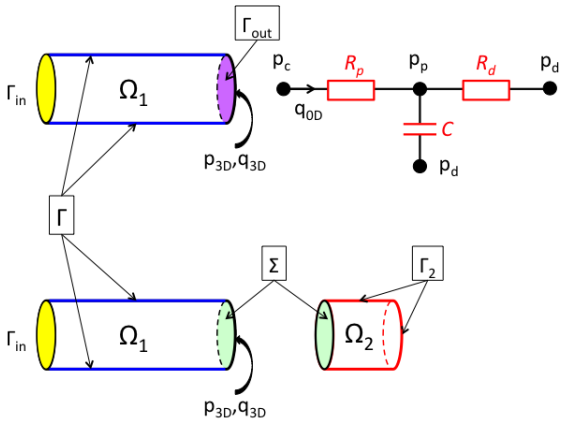

Figure 2.1: Top: 3D domain of a Navier-Stokes model (section 2.1.1) coupled to a Windkessel model (section 2.1.3), corresponding to the 3D-0D coupling scheme in section 3.3.3). Bottom: 3D-3D coupling scheme in section 3.3.3).

2.1.2 1D equations of flow: wave propagation due to viscoelastic walls

Of the flow models cited above, lumped-parameter models do not capture wave propagation phenomena, which are in some diseases of clinical importance. On the other hand, 3D methods are anatomically accurate but computationally expensive. A good compromise may be found with 1D models of blood flow that enable the study of wave propagation phenomena while being computationally inexpensive compared to 3D fluid-structure interaction models.

The one-dimensional equations for the flow of a Newtonian, incompressible fluid in a deforming, elastic domain consist of the continuity equation, a single axial momentum bal-

ance equation, a constitutive equation, and suitable initial and boundary conditions. The governing equations have been derived in a general form (i.e. without assuming axisymmetry or shape of the cross-sectional area, and allowing for permeable walls) by Hughes [Hughes and Lubliner, 1973]. This theory assumes that the velocity u is mostly in the axial direction, the vessel is longitudinally tethered between two fixed planes, the no-slip condition holds at the wall and that the axial velocity can be separated in a profile function times the mean velocity. As a consequence pressure is uniform in a given cross sectional area. The partial differential equations for mass and momentum balance are given by (z is the axial coordinate along a segment between two fixed planes, or the union of such segments Ω – see [Peiró and Veneziani, 2009] for curved cases)

$$\frac{\partial S}{\partial t} + \frac{\partial Q}{\partial z} = -\psi \tag{2.5}$$

$$\frac{\partial Q}{\partial t} + \frac{\partial}{\partial z}((1+\delta)\frac{Q^2}{S}) = -\frac{S}{\rho}\frac{\partial P}{\partial z} + N\frac{Q}{S} + \nu\frac{\partial^2 Q}{\partial z^2} \tag{2.6}$$

The primary variables are the cross-sectional area $S : \Omega \times \mathbb{R}^+ \to \mathbb{R}^+$, the pressure $P : \Omega \times \mathbb{R}^+ \to \mathbb{R}$, and the volumetric flow rate $Q : \Omega \times \mathbb{R}^+ \to \mathbb{R}$ defined from the 3D velocity as $Q := \int_{S_{(z,t)}} \boldsymbol{u} \cdot \boldsymbol{n}$, $\boldsymbol{n}$ being the normal to the cross-section at axial position z. The density of the fluid is given by ρ (assumed constant), the kinematic viscosity by ν (assumed constant) and $\psi : \Omega \times \mathbb{R}^+ \to \mathbb{R}$ is an outflow function at the wall (taken to be zero for impermeable vessels, which will be the case thereafter). In the momentum equation, inertia (left of the equation) is balanced by the pressure force and two viscous losses. The parameters δ and N are dependent upon the choice of a profile function for the velocity over the cross-section [Hughes and Lubliner, 1973]. For a parabolic profile, $\delta = \frac{1}{3}$ and $N = -8\pi\nu$. Note that mean axial velocity $U := Q\backslash S$ is sometimes chosen as variable instead of Q. The flow rate or the pressure are typically specified at the inlets or outlets, but other conditions are considered later as well. Initial conditions need to be given. In order to complete the above system, a constitutive relationship for the vessel wall is chosen that relates pressure and cross-sectional area. For example in the case of a linearly elastic thin wall assuming independent radial movement of the different sections [Olufsen, 1999]:

$$P(S,z) = P^0(z) + \frac{4Eh}{3r^0(z)}(1 - \sqrt{(}\frac{S(z,t)}{S^0(z)})) \tag{2.7}$$

where the Young's modulus E and the wall thickness h relate to the nominal radius $r^0 = \sqrt{(}S^0/\pi)$, ^{0} denoting a reference configuration. But other choices can be made [Pedley et al., 1996, Quarteroni et al., 2000, Formaggia et al., 2003] and in particular we will study viscoelasticity later in this section. The flow through bifurcations, where three segments join, is governed by conservation of mass and balance of momentum or continuity of pressure. Note that balance of momentum is more desirable energetically, but a difference has not been seen in practice [Formaggia et al., 2003]. This set of equations cannot, in general, be solved analytically. Therefore, a numerical approximation is needed. Often, the viscous term $\nu\frac{\partial^2 Q}{\partial z^2}$ is neglected in equation 2.6 due to its magnitude. The resulting equations are then hyperbolic and can be solved using the method of characteristics ([Lambert, 1958, Anliker et al., 1971] and many others at that time and later). The finite difference method is often used to numerically solve these equations [Stergiopulos et al., 1992, Curcio et al., 2004, Pontrelli, 2002], and in particular the two step Lax-Wendroff finite difference scheme [Smith et al., 2002, Olufsen et al., 2000, Canić, 2002]. Sherwin et al. [Sherwin et al., 2003b, Sherwin et al., 2003a] compared the combination of the discontinuous Galerkin finite element spatial discretization and the Adams-Bashforth time integration scheme with a Taylor-Galerkin scheme, finite element counterpart of the two-step Lax Wendroff finite difference scheme, which was also developed by Formaggia et al.

[Formaggia et al., 2002b]. The comparison, verification and validation of numerical methods has recently regained some attention [Wang et al., 2015, Boileau et al., 2015], and we refer to these papers for pros and cons of these methods. The conclusion is that, except for rare shock-like phenomena, these different schemes give very similar results. Following Hughes [Hughes and Lubliner, 1973], the Taylor group [Wan et al., 2002, Steele et al., 2007] [21] included the viscous term $\nu\frac{\partial^2 Q}{\partial z^2}$. The system becomes parabolic, which is well known to exhibit better regularity properties than hyperbolic systems [Curcio et al., 2004]. This also happens in certain viscoelastic formulations [Quarteroni et al., 2000]. A space-time finite element method, treating time as a space variable was developed to numerically solve these equations as this scheme had been shown to yield stable and time-accurate solutions for advective-diffusive systems in fluid-mechanics [Wan et al., 2002].

The size and complexity of the cardiovascular system necessitate a multidomain approach (see sections 2.1, 3), with *upstream* regions of interest (large arteries) coupled to reduced-order models of *downstream* vessels. Previous efforts to [21] to couple upstream and downstream domains in 1D have included specifying resistance and impedance outflow boundary conditions for the nonlinear 1D wave propagation equations, but the theoretical framework to couple these different domains is missing. In [21] we propose such a multidomain framework. Numerically, we solve the 1D nonlinear equations of blood flow in conservative form utilizing a space-time finite element method with Galerkin Least Square stabilization for the upstream domain, and a boundary term to couple to the downstream domain. The motivation to work with the conservative form rather than the advective form as in previous work [Wan et al., 2002], is to be able to integrate by part the convective term and obtain a non-negligible flux through which the multidomain coupling can be performed. The outflow boundary conditions are derived following an approach analogous to the Dirichlet-to-Neumann (DtN) method (see 3.2). In the downstream domain, we solve simplified zero/one-dimensional equations to derive relationships between pressure and flow accommodating periodic and transient phenomena with a consistent formulation for different boundary condition types. In this work, we also present a new boundary condition that accommodates transient phenomena based on a Green's function solution of the linear, damped wave equation in the downstream domain. Results show minimal artificial wave reflection. Alternative downstream models are compared by solving idealized and patient-specific problems. We demonstrate that a DtN map can be calculated for the impedance of complex vascular trees and that this approach incorporates naturally occurring wave reflections from a downstream bed. Wave propagation in transient and periodic states is simulated and the importance of selecting appropriate boundary conditions is demonstrated for one-dimensional simulations of blood flow (see fig. 2.3). We find that the best boundary condition for cardiovascular applications is not the one that exhibits no wave reflection, since wave reflections naturally arising from downstream beds (from bifurcations, tapering, and variations in wall properties) should propagate back upstream into the numerical domain. We conclude that, at present, impedance-based boundary conditions (computed on linearized 1D equations integrated on fractal trees) are the best approach for incorporating natural sites of wave reflection in the downstream vasculature.

However it is well known that blood vessels exhibit viscoelastic properties ([Learoyd and Taylor, 1966] and other references in [22]), although most 1D models of blood flow, have employed elastic constitutive behaviors. Vessel wall viscoelasticity introduces a phase difference between pressure and wall deformation. This leads to the well-known hysteresis loop where the region within the loop is representative of the energy dissipated by the vessel wall under periodic loading. Viscoelasticity of the vessel wall is an important source of physical damping and its presence is usually attributed to smooth muscle cells. It affects clinically relevant quantities such as flow and pressure in normal and pathological conditions. Studies have shown that viscous properties of the vessel wall are altered by hypertension,

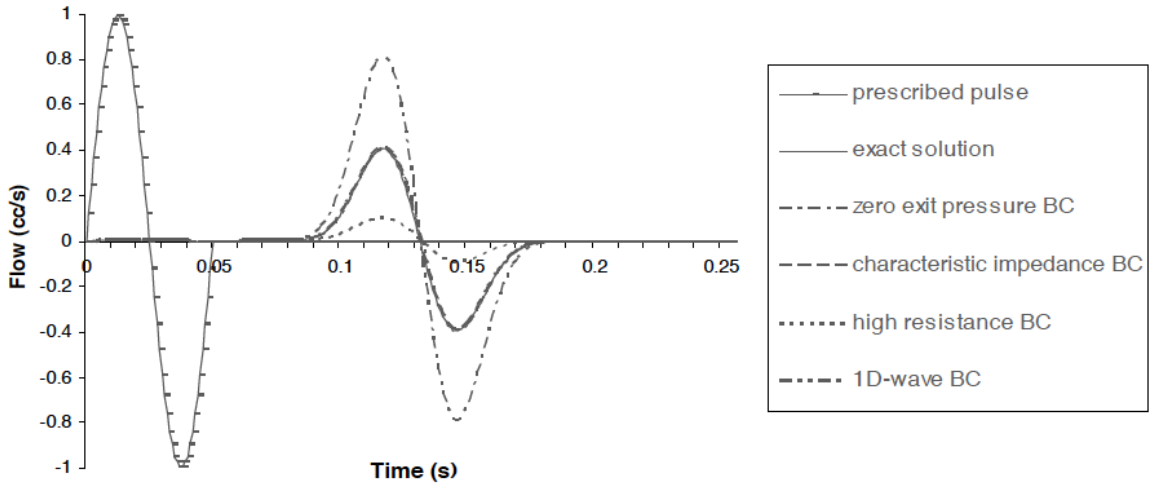

Figure 2.3: Effect of boundary conditions on wave reflection. An inlet flow pulse and a transient flow rate at the outlet were presented for an elastic vessel with a radius of 0.3 cm and a length of 80 cm. Results at the outlet are shown for different outlet boundary conditions. Note that the outlet flow rate for the characteristic impedance BC and the 1D-wave BC curves coincide with the *exact* solution. The zero exit pressure BC gives rise to a large spurious reflection, whereas the high resistance case overly damps the pulse.

which in turn is a risk factor for atherosclerosis and aneurysm disease. For instance, viscous energy dissipation in the carotid artery was reported to be higher under hypertension conditions.

When taken into account, viscoelastic equations of blood flow are modeled in the literature with different mathematical forms and experimental bases. The wide range of existing viscoelastic wall models may produce significantly different blood flow, pressure, and vessel deformation solutions in cardiovascular simulations. In this work [22], we present a novel comparative study of two different viscoelastic wall models modifying the nonlinear 1D equations of blood flow described above. The viscoelastic models are from papers by Holenstein et al. in 1980 (model V1) [Holenstein et al., 1980] and Valdez-Jasso et al. in 2009 (model V2) [Valdez-Jasso et al., 2009]. The static elastic or zero-frequency responses of both models are chosen to be identical. The 1D blood flow equations incorporating wall viscoelasticity are solved using a space-time finite element method and the implementation is verified with the *Method of Manufactured Solutions*.

Simulation results using models V1, V2 and the common static elastic model are compared in three examples of increasing complexity: (i) wave propagation study in an idealized vessel with reflection-free outflow boundary condition; (ii) carotid artery model with non-periodic boundary conditions; and (iii) subject-specific abdominal aorta model under rest and simulated lower limb exercise conditions 2.4. In the wave propagation study the damping and wave speed are largest for model V2 and lowest for the elastic model. In the carotid and abdominal aorta studies the most significant differences between wall models are observed in the hysteresis (pressure-area) loops, which were larger for V2 than V1, indicating that V2 is a more dissipative model. The cross-sectional area oscillations over the cardiac cycle are smaller for the viscoelastic models compared to the elastic model. In the abdominal aorta study, differences between constitutive models are more pronounced under exercise conditions than at rest. Inlet pressure pulse for model V1 is larger than the pulse for V2 and the elastic model in the exercise case. In this work, we have successfully implemented and verified two viscoelastic wall models in a nonlinear 1D finite element blood flow solver and analyzed differences between these models in various idealized and physiological simulations, including exercise.

The computational model of blood flow presented here can be utilized in further studies of the cardiovascular system incorporating viscoelastic wall properties, although comparison to experimental data would be needed to delineate the domain of validity of each model.

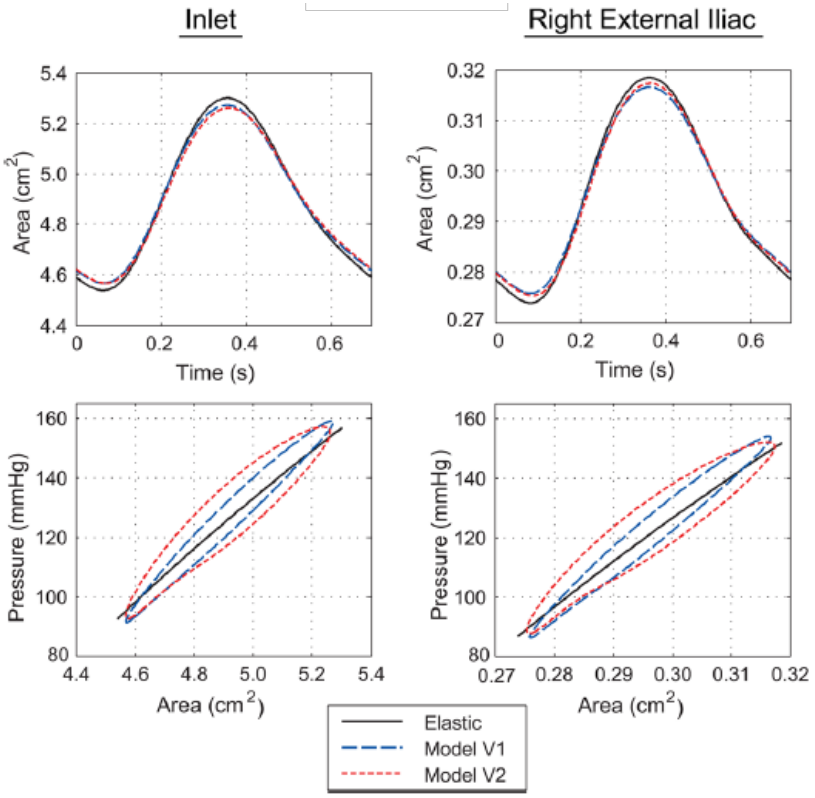

Figure 2.4: Cross-sectional area over one heart beat and pressure-area hysteresis under lower limb exercise conditions at the inlet and right external iliac outlet of the subject-specific abdominal aorta model [22].

2.1.3 Reduced modeling of the entire system

The concept of peripheral resistance and the notion of the arterioles and capillaries constituting the major vascular resistance was probably first described by Hales in his book *Haemostatics* in 1733. Around 1838, the physician Poiseuille (and Hagen in 1939) then related the resistance (R) to steady flow in a cylindrical tube to the fluid viscosity μ and the dimensions of the tube (length L and radius r): $R = \frac{8\mu L}{\pi r^4}$. The so called *(Hagen-)Poiseuille relation* which linearly relates the pressure loss ΔP to the flow Q and resistance as $\Delta P = RQ$, can be derived from the Navier-Stokes equations assuming steady, axisymmetric, uniaxial, developed flow of a Newtonian fluid in a cylindrical, straight and rigid tube. As a consequence, the pressure is uniform on a given cross section. An equivalent resistance to flow, or resistance operator, in a 3D domain or a network of branching tubes can also be defined under some assumptions [Maury, 2014]. The case of a dyadic tree, and its convergence when infinite, is studied in [Grandmont et al., 2006].

The RCR or *Windkessel* model is an electric analog that has a proximal resistance R_p in series with a parallel arrangement of a capacitance C and a distal resistance R_d (see fig. 2.1, 4.15). A downstream pressure potentially varying in time, can be used, e.g. to represent the pressure in the right atrium. The Windkessel model was originally derived by the German physiologist Otto Frank in an article published in 1899 to describe the afterload of the heart related to pumping blood through the pulmonary or systemic arterial system. The proximal

Table 2.1: Pressure and flow-rate relationship for various components: p represents pressure and q represents flow-rate

component	p-q relationship	component	p-q relationship
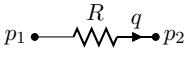	$p_1 - p_2 = R\, q$	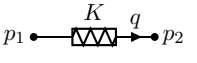	$p_1 - p_2 = K\, q\|q\|$
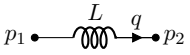	$p_1 - p_2 = L\, \dot{q}$	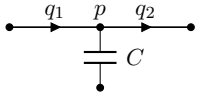	$q_1 - q_2 = C\, \dot{p}$

resistance represents the resistance to flow in the major arteries that have the capacity due to their wall elasticity to store blood during systole and restore it during diastole. It is assumed that after these major arteries, the rest of the vascular bed is purely resistive, represented by R_d. The end pressure of the circuit is assumed to be a known function of time (typical values are zero for the systemic side and the left atrium pressure for the pulmonary side). This model retains the same spatial assumptions as for Poiseuille flow.

Respiration on the other hand is a dynamic process where air flows in (inspiration) and out (expiration) through a resistive tree of airways terminated by elastic alveoli and surrounding tissue (fig. 1.3), which simplest model (the 'pipe-balloon' model or RC model) is a resistance R in series with a capacitance C [Bates, 2009, Maury, 2013]. Note that the resistance effectively also represents dissipation due frictional forces in the lung tissue.

These models are the simplest forms of a lumped parameter model, i.e. flow description as a dynamical system. It is also called *0D* model as it neglects the spatial variation of the parameters and variables, and thus the only variable is time. If the model is distributed, these parameters and variables are assumed to be uniform in each spatial compartment. Therefore, a lumped parameter model is described by a set of coupled ordinary differential equations representing the dynamics of the variables in each compartment. By electric analogy, the blood circulation and the respiratory system are described as networks, where pressure plays the role of voltage and flow rate the role of current. The impedance of a compartment can represent conduits *explicitly* - such as in arterial, venous and respiratory systems modeled as structured or morphometric trees [Olufsen, 1999, Spilker et al., 2007, Oakes et al., 2012] [21, 11] and in explicit microcirculation representation (see section 2.3, [8]) -, or *effectively*, e.g. lung lobe by lung lobe for respiration (fig. 4.1, 4.4), entire vessel trees distal to a vessel of interest ([13, 23, 19] and fig. 4.8) or even groups of organs in blood circulation [24, 25, 26].

Resistance, capacitance and inductance (representing fluid inertia) relations to conduit geometry and fluid properties can be derived by spatial integration of the 1D equations of section 2.1.2 [Peiró and Veneziani, 2009]. But in case of effective network representations, their values are not easy to define (see chap. 4). Nonlinear components are rather phenomenological descriptions of a more complex behavior, e.g. for nonlinear lung capacitance [Bates, 2009, Martin and Maury, 2013], for nonlinear resistance in the aorta ([20] and fig. 4.15) or in shunts [Migliavacca et al., 2001], for heart chambers [Suga and Sagawa, 1974, Arts et al., 1991, Migliavacca et al., 2001, Caruel et al., 2014], for a new regurgitant valve model [26]. Shown in fig. 2.5 is an example of a *closed-loop* model of the circulation (recall fig. 1.1), meaning where the only driving source term of the dynamical system is the activation of the heart, and neither pressure nor flow are given at a certain node. Table 2.1 gives the algebraic relations or ODEs representing the most common components.

The resulting model is a coupled system of ODEs and algebraic equations, usually quite stiff due to the heart model. It can be solved with libraries such as the IDA solver, a part of SUNDIALS (Suite of Nonlinear and Differential/Algebraic Equation Solvers) [Hindmarsh, 2000, Hindmarsh et al., 2005]. But other methods (Runge-Kutta 4, etc.) have been used and we refer to the above cited papers for more information.

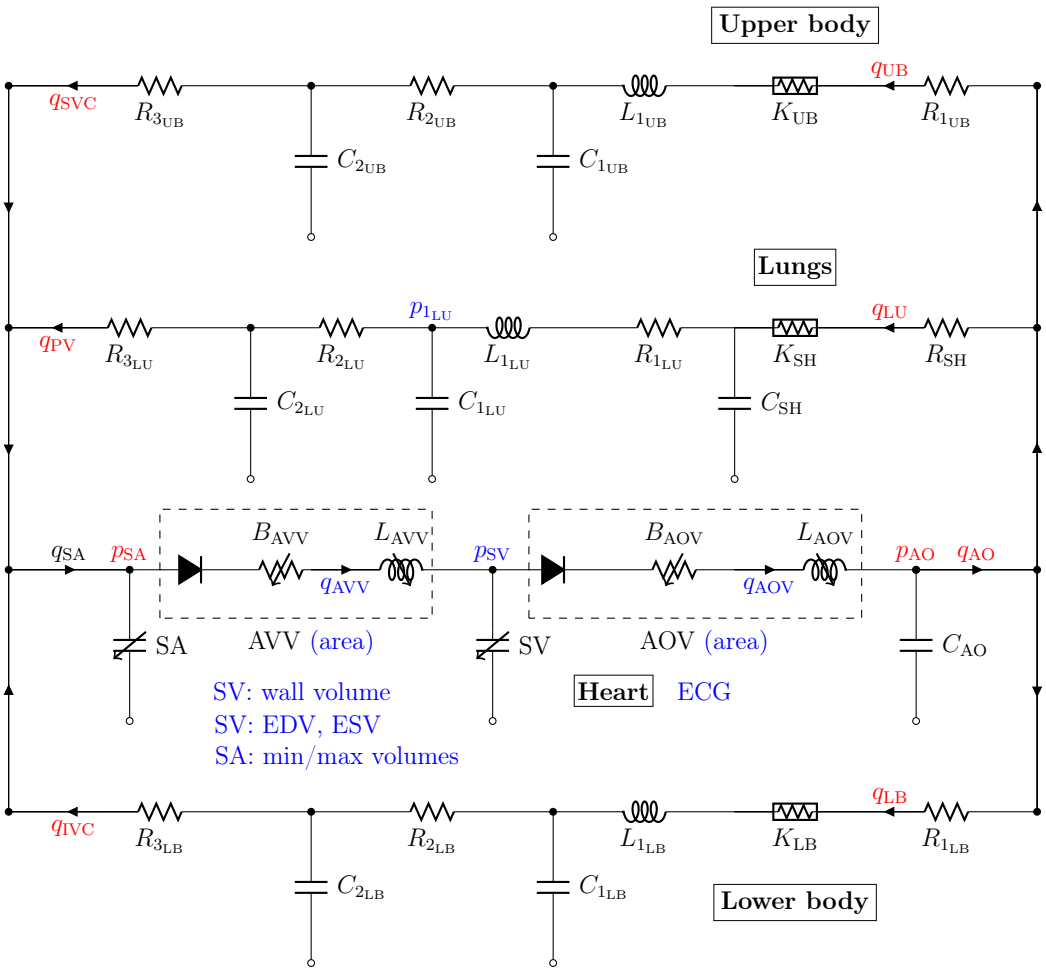

Figure 2.5: Closed-loop 0D model for single-ventricle circulation with heart, lungs, lower and upper body compartments. Measurements are shown in red for parameter estimation and in blue for validation (see section 4.3 or [26]).

2.2 Tissue-scale (multiphysics) modeling

Blood and air flow can be affected by the surrounding elastic wall and tissue. The interaction between the fluid and the surrounding structure (FSI) can be modeled by different approaches, which has been the subject of intense research in the last 10 years (see references in the cited papers next). In [12], we took into account the vessel elasticity as a membrane, simulating for the first 3D FSI in the aorta. This permitted to study repair effects in coarctation of the aorta, an aortic narrowing which is a common CHD [2, 27]. We studied vessel wall viscoelasticity in 1D models of blood flow [22] (see section 2.1.2). These works were later extended by others to add the surrounding tissue effect and their parameter estimation [Moireau et al., 2012, Moireau et al., 2013].

All these works are based on the detailed 1D or 3D representation of the vessel geometry. If the latter is not known explicitly but that FSI effects are important, poroelasticity is an alternative option. This is what will now be developed in this section, as a summary of our work in [28]. This work is motivated by the modeling of blood flows through the beating myocardium, namely cardiac perfusion. The main contribution of this study is the derivation of a general poroelastic model valid for a nearly incompressible medium which experiences finite deformations. A numerical procedure is proposed to iteratively solve the porous flow and the nonlinear poroviscoelastic problems. Three-dimensional numerical experiments are presented to illustrate the model. The first test cases consist of typical poroelastic configura-

tions: swelling and complete drainage. Finally, a simulation of cardiac perfusion is presented in an idealized left ventricle embedded with active fibers. Results show the complex temporal and spatial interactions of the muscle and blood, reproducing several key phenomena observed in cardiac perfusion.

2.2.1 Poromechanics: a different fluid-structure interaction model

Despite recent advances on the anatomical description and measurements of the coronary tree – see e.g. [Spaan et al., 2008, Horssen et al., 2009] – and on the corresponding physiological, physical and numerical modeling aspects – see e.g.[Westerhof et al., 2006, Smith and Kassab, 2001, Smith, 2004] – the complete modeling and simulation of blood flows inside the coronaries from the arteries to the veins via the capillaries is still out of reach. Therefore, in order to model blood perfusion in the cardiac tissue, we must limit the description of the detailed flows at a given space scale, and simplify the modeling of the smaller scale flows by aggregating these phenomena into macroscopic quantities, by some kind of 'homogenization' procedure. To that purpose, the modeling of the fluid-solid coupling within the framework of porous media appears appropriate.

Poromechanics is a simplified mixture theory where a complex fluid-structure interaction problem is replaced by a superposition of both components, each of them representing a fraction of the complete material at every point. It originally emerged in soils mechanics with the work of Terzaghi [Terzaghi, 1943], and Biot [Biot, 1956, Biot, 1972] later gave a description of the mechanical behavior of a porous medium using an elastic formulation for the solid matrix, and Darcy's law for the fluid flow through the matrix. Finite strain poroelastic models have already been proposed [May-Newman and McCulloch, 1998, Almeida and Spilker, 1998, Yang and Smolinski, 2006, Borja, 2006], albeit with *ad hoc* formulations for which compatibility with thermodynamics laws and incompressibility conditions is not established. Poroelastic models have also been considered in the framework of fluid-structure interaction, e.g. to model blood vessel walls [Badia et al., 2009], with some extensions including lipid (LDL) [Koshiba et al., 2007] and drug [Calo et al., 2008, Feenstra and Taylor, 2009] transport. Other formulations have been proposed with multiple fluid compartments – or a continuum of such compartments – coupled with each other and with the solid medium [Huyghe and van Campen, 1991a, Huyghe and van Campen, 1991b, Cimrman and Rohan, 2003], and with applications to the modeling of living tissues [Vankan et al., 1997], but of course such models are extremely difficult to validate with experimental evidence in practice.

2.2.2 A poroelastic model valid for large strain

We introduce a general poroelastic formulation valid for finite strains and compatible with incompressibility, as these two features are deemed to be important in the modeling of living tissues. We follow the strategy – presented in [Coussy, 1995] in a linear framework – of deriving the formulation from an appropriate free energy functional, which is crucial to guarantee that fundamental thermodynamics principles are satisfied. In this section, we first introduce kinematical and conservation laws of the porous medium. Based on thermodynamics considerations we then develop the constitutive laws that characterize the solid phase, the fluid phase and their interaction. The saturated porous continuum consists of a solid part – referred to as the "skeleton" – and a fluid part that accounts for fraction ϕ of the combined volume in the deformed configurations. The subscript "0" will be used to refer to the reference configuration. Let $\underline{y}$ be the displacement field of the skeleton as defined in a Lagrangian formulation, namely, given with respect to a fixed reference configuration. Then as classically in mechanics

$$\underline{\underline{F}} = \underline{\underline{1}} + \underline{\nabla}_{\hat{x}}\, \underline{y}, \quad J = \det \underline{\underline{F}}, \quad \underline{\underline{C}} = \underline{\underline{F}}^T \cdot \underline{\underline{F}}, \quad \underline{\underline{e}} = \frac{1}{2}\big(\underline{\underline{C}} - \underline{\underline{1}}\big)$$

are respectively the deformation gradient, local volume change, right Cauchy-Green deformation tensor and the Green-Lagrange strain tensor. Denoting indifferently by a dot symbol or by $\frac{d.}{dt}$ the Lagrangian time derivatives – namely, obtained when following "solid particles" – geometrical considerations lead to

$$J\nabla \cdot \underline{u}^s = \frac{dJ}{dt}, \tag{2.8}$$

where $\underline{u}^s = \underline{\dot{y}}$ is the velocity of a solid particle. The divergence is here considered in Eulerian form. Denoting by m the change in fluid mass per unit volume of the reference configuration, by definition,

$$m = \rho^f J\phi - \rho_0^f \phi_0, \tag{2.9}$$

where ρ^f is the fluid mass per unit of fluid volume. Furthermore, conservation of fluid mass is in Eulerian form:

$$\frac{\partial}{\partial t}(\rho^f \phi) + \nabla \cdot (\rho^f \phi\, \underline{u}^f) = \rho^f s, \tag{2.10}$$

with $\underline{u}^f$ the velocity of a fluid particle, and s a general sink or source term. Combining the equations (2.8) and (2.10) with the definition of the perfusion velocity $\underline{w} = \phi(\underline{u}^f - \underline{u}^s)$, and of the added mass m in (2.9), we obtain the general conservation of fluid mass in porous media

$$\nabla \cdot (\rho^f \underline{w}) + \frac{1}{J}\frac{dm}{dt} = \rho^f s. \tag{2.11}$$

In addition, conservation of mass of the solid phase can be written as

$$J\rho^s(1-\phi) = \rho_0^s(1-\phi_0). \tag{2.12}$$

The balance of momentum of the porous medium written in Lagrangian form:

$$(\rho_0 + m)\,\underline{\ddot{y}} = \nabla_{\hat{x}} \cdot \big(\underline{\underline{F}} \cdot \underline{\underline{\Sigma}}\big). \tag{2.13}$$

In the inertia term, we have neglected the discrepancy between the fluid and solid accelerations, and ρ_0 denotes the total mass per unit volume in the reference configuration, i.e. $\rho_0 = \phi_0\rho_0^f + (1-\phi_0)\rho_0^s$. We then propose some constitutive equations to adequately represent poromechanics in finite strain in a formulation compatible with the incompressible limit.

Thermodynamics considerations [Coussy, 1995, de Buhan et al., 1998] entail the existence of a Helmholtz free energy $\Psi = \Psi(\underline{\underline{e}}, m, T)$, where T denotes the temperature. In the absence of internal dissipation we then have

$$\underline{\underline{\Sigma}} = \frac{\partial \Psi}{\partial \underline{\underline{e}}}, \quad g_m = \frac{\partial \Psi}{\partial m}, \tag{2.14}$$

where $\underline{\underline{\Sigma}}$ denotes the second Piola-Kirchhoff stress tensor and $g_m(p,T)$ the free enthalpy (also called Gibbs free energy) of the unit fluid mass, which characterizes the fluid constitutive behavior through

$$\frac{1}{\rho^f} = \frac{\partial g_m}{\partial p}, \tag{2.15}$$

where p is the fluid pressure – also called *interstitial* pressure. The constitutive behavior of the poroelastic material is then entirely characterized by the choice of the functionals Ψ and g_m. Assuming an isothermal regime, we propose to extend the linear theory of [Coussy, 1995] by considering

$$\Psi = W^{hyp}(\underline{\underline{e}}) - Mb\frac{m}{\rho_0^f}(J-1)f(J) + \frac{1}{2}M\left(\frac{m}{\rho_0^f}\right)^2 f(J), \tag{2.16}$$

$$g_m = \frac{p - p_0}{\rho_0^f}. \tag{2.17}$$

In the expression (2.16), W^{hyp} denotes some hyperelastic potential to be chosen, M is the so-called Biot modulus, b a parameter characteristic of the skeleton and f a function to define. Note that the choice (2.17) directly implies with (2.15) that the fluid considered is incompressible. Concerning (2.16) the most straightforward extension of the linear theory would correspond to $f(J) = 1$, but this choice as demonstrated in [28] is in general incompatible with incompressible conditions, by which we now mean incompressibility of the fluid and the solid individually. With the choices (2.16)-(2.17) the direct application of (2.14)-(2.15) then gives

$$\underline{\underline{\Sigma}} = \frac{\partial W^{hyp}}{\partial \underline{\underline{e}}} - Mb\frac{m}{\rho_0^f}\big(f + (J-1)f'\big)J\underline{\underline{C}}^{-1} + \frac{1}{2}M\left(\frac{m}{\rho_0^f}\right)^2 f' J\underline{\underline{C}}^{-1}, \tag{2.18}$$

$$p - p_0 = Mf(J)\left(b(1-J) + \frac{m}{\rho_0^f}\right). \tag{2.19}$$

In order to be consistent with incompressibility, the singularity arising from the hyperelastic stress in the incompressible limit – associated with a "large" bulk modulus – must be compensated by the second term in the right-hand side. Indeed, in the poroelastic material incompressibility does not induce constraints on the strains *per se*, as added fluid can change the apparent volume without violating the incompressible assumption. Hence, we need to adapt the expression of $f(J)$ according to the specific hyperelastic potential considered. In particular, when using the modified Ciarlet-Geymonat expression (see [Ciarlet and Geymonat, 1982] for the original formulation, J_1 and J_2 being the first two invariants of the left Cauchy-Green deformation tensor)

$$W^{hyp} = \kappa_1(J_1 - 3) + \kappa_2(J_2 - 3) + K(J-1) - K\ln J, \tag{2.20}$$

where nearly-incompressible materials are obtained by taking the bulk modulus K large compared to the other material parameters κ_1 and κ_2, we obtain

$$\underline{\underline{\Sigma}} = \frac{\partial W^{MR}}{\partial \underline{\underline{e}}} + \left[K - Mb^2 J\big(f + \tfrac{1}{2}(J-1)f'\big)\right](J-1)\underline{\underline{C}}^{-1} - b(p-p_0)J\underline{\underline{C}}^{-1} + \frac{1}{2}\frac{(p-p_0)^2}{M}\frac{f'}{f^2}J\underline{\underline{C}}^{-1}, \tag{2.21}$$

where we denote by W^{MR} the Mooney-Rivlin type potential $W^{MR} = \kappa_1(J_1 - 3) + \kappa_2(J_2 - 3)$. In the form (2.21) we can see that a necessary and sufficient condition for canceling the singularity is to ensure

$$J\big(f + \tfrac{1}{2}(J-1)f'\big) = 1, \quad \forall J, \tag{2.22}$$

and have $\kappa_s = K - Mb^2$ remain finite when K grows large. This leads to

$$f(J) = \frac{2(J - 1 - \ln J)}{(J-1)^2}, \quad f(1) = 1, \tag{2.23}$$

κ_s can be interpreted as an elasticity modulus for the skeleton; it also plays the role of the apparent bulk modulus of the drained material, which remains finite in the incompressible limit when K tends to infinity, since the drained poroelastic material can freely absorb or expel some fluid.

With the above poroelastic constitutive law, we may encounter some difficulties with the evolution of the porosity ϕ which is simply deduced from m and J by (2.9). This may indeed lead to the violation of the constraint $0 < \phi < 1$ which should always hold. Here we slightly modify the free energy (2.16) by considering

$$\Psi = W^{hyp}(\underline{\underline{e}}) - Mb\frac{m}{\rho_0^f}(J-1)f(J) + \frac{1}{2}M\left(\frac{m}{\rho_0^f}\right)^2 f(J) - \kappa_0 \ln\left(\frac{m}{\rho_0^f} + \phi_0\right), \tag{2.24}$$

where the additional term will result in $m/\rho_0^f + \phi_0 > 0$, hence $\phi > 0$ by (2.9). This leaves the constitutive equation (2.18) unchanged, while (2.19) is transformed into

$$p - p_0 = Mf(J)\left(b(1-J) + \frac{m}{\rho_0^f}\right) - \frac{\kappa_0}{m/\rho_0^f + \phi_0}. \tag{2.25}$$

This shows that $p - p_0$ can become arbitrarily large (in negative values) when m/ρ_0^f tends to $-\phi_0$ from above, as desired.

Finally, the second principle of thermodynamics – the dissipation associated with the transport of fluid mass [Coussy, 1995] – leads to the last equation needed to fully characterize the system, also known as Darcy's law:

$$\underline{w} = -\underline{\underline{K}} \cdot \nabla p. \tag{2.26}$$

$\underline{\underline{K}}$ being the permeability tensor, conceptually similar to a distributed inverse of a resistance to flow. The system of equations characterizing the porous media dynamics follows from (2.13), (2.11), (2.26) and (2.19): Find $\underline{y}$, $\underline{w}$, p and m such that

$$\begin{cases} (\rho_0 + m)\ddot{\underline{y}} = \nabla_{\hat{x}} \cdot \left(\underline{\underline{F}} \cdot \underline{\underline{\Sigma}}\right), \\ \nabla \cdot \underline{w} + \dfrac{1}{JMf}\dfrac{dp}{dt} - \dfrac{f'}{Mf^2}(p - p_0)\nabla \cdot \underline{u}^s = -b\nabla \cdot \underline{u}^s + s, \\ \underline{w} = -\underline{\underline{K}} \cdot \nabla p, \\ p - p_0 = Mf(J)\left(b(1-J) + \dfrac{m}{\rho_0^f}\right) - \dfrac{\kappa_0}{m/\rho_0^f + \phi_0}. \end{cases} \tag{2.27}$$

This system needs to be complemented by adequate boundary conditions, typical of solid and fluid equations. Finite-element codes tailored for the solid and fluid parts are iteratively coupled and the nonlinear system is solved through an accelerated fixed point algorithm on m. More information can be found in [28].

2.2.3 Numerical results

In this section we present two test problems to illustrate the behavior of this poroelastic model under large deformations: swelling and drainage of a cube. In the swelling test, no external force is applied on the skeleton but a fluid pressure gradient is imposed between two opposite faces whereas a null flux condition is applied on the four other faces (see fig. 2.6). As a consequence, fluid enters in the medium from the inlet face. Velocity increases as the inlet pressure rises. The cube swells like a sponge undergoing large deformation as shown in fig. 2.6. When the inlet pressure has reached its limit value, a steady state takes place: the elastic forces are in equilibrium with the pressure increase due the added fluid. Although pressure decreases roughly linearly with x, the added fluid mass decreases nonlinearly (see the plots of p and m over time for three points across the cube in fig. 2.6). The perfusion velocity goes mainly in the x direction, but unlike for a purely Darcy flow, it is not homogeneous in space (see the arrows on the deformed cube).

By contrast, in the drainage test, an external pressure P_{v} of the order of magnitude of the left ventricle pressure in systole 10 kPa is gradually applied on all the faces of the cube (skeleton part). For the fluid, a null flux condition is applied on all the faces but the pores are connected to a pressure sink term $s = -\beta(p - p_{sink})$. As a result, the fluid is drained out of the sponge and the cube shrinks. If the external pressure is high enough to drain all the fluid, the penalization introduced in equation (2.25) prevents ϕ from being negative. The results thus show two different phases (fig. 2.6). In the first phase, fluid is drained until the porosity is nearly zero, at which point $m \approx -\phi_0$. In the second phase, the skeleton behaves as its solid component (we only see the compressibility effects through the bulk K). The

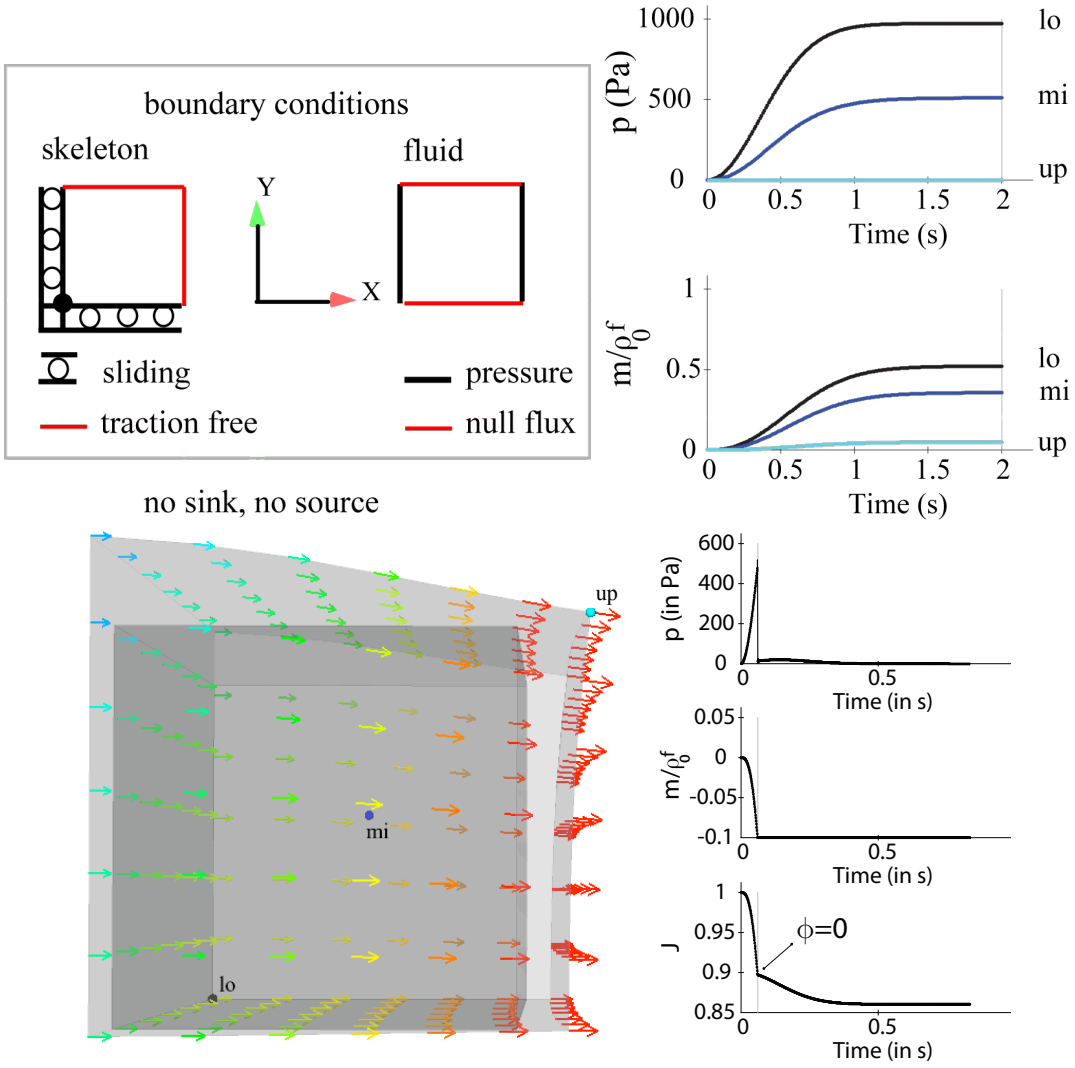

Figure 2.6: Swelling and drainage tests of a cube. *Left*: Swelling test boundary conditions and solution. Dark grey represents the initial cube, and light grey the deformed cube. The arrows are the velocity vectors, colored by their magnitude. *Upper right*: pressure and mass are plotted against time for three points (the lower point attached to the inlet face in black, the middle point in blue and the upper point attached to the outlet face in cyan). *Lower right graph*: drainage test of the porous medium by applying an external pressure on the exterior of the skeleton. Fluid is first drained out of the media until $\phi = 0$. Then the medium is compressed according to the compressibility of the solid phase.

theoretical steady state is thus given by the equilibrium of the volume terms in (2.18), i.e. $K(1-1/J) + Mb\frac{\phi_0}{\rho_0^f}\big(f + (J-1)f'\big) + \frac{1}{2}M\left(\frac{\phi_0}{\rho_0^f}\right)^2 f' = -P_{\mathrm{v}}$. The numerical results verify this analytical expression.

Finally, we present the application to cardiac perfusion. The active contraction of the myocardium forces blood into the aorta and the coronaries, which supply the myocardium with blood, and thus oxygen. Unlike most of the organs, this flow of blood occurs in a very dynamic network of vessels, due to the beating of the heart. Until now we have considered a passive poroelastic material. In order to represent the active behavior of the cardiac tissue, we extend the approach described in [Sainte-Marie et al., 2006] to incorporate porous flow. The complete expression of the 3D stress tensor reads

$$\underline{\underline{\Sigma}}_{heart} = \underline{\underline{\Sigma}}\big(\underline{\underline{e}}, m\big) + \eta\,\underline{\underline{\dot{e}}} + \sigma_{1D}\ \underline{n}\otimes\underline{n}, \tag{2.28}$$

where "$\otimes$" denotes tensorial product for the activation along the 1D fibers and η represents the viscosity of the tissue.

Heart perfusion consists of a flow through coronary arteries, arterioles, capillaries, venules and veins. Several compartments could be modeled individually by a porous medium flow and coupled through exchange terms (see *e.g.* [Vankan et al., 1997]). Our experience with this kind of approach is that it can be extremely difficult to parametrize each compartment in order to get meaningful behaviors in realistic 3D configurations, in particular to avoid non-physiological backflows. Here we use a single compartment poroviscoelastic model, which is supposed to only describe small arteries, capillaries and small veins. The venous network is modeled as a simple sink term in the porous flow equations. The porous flow is assumed for simplicity to be fed by a distributed arterial source term. Thus in the second equation of (2.27), $s = \beta_a(p_a - p) - \beta_v(p - p_v)$, where β_a, p_a and β_v, p_v are given constants, respectively characterizing the small arteries and small veins compartments.

We now present a simulation of the model described above on a 3D analytical geometry that mimics the left ventricle. Fibers are embedded with an orientation that varies nonlinearly across the wall [Sainte-Marie et al., 2006]. The activation of the muscle occurs during 0.25 s, after which the muscle relaxes so that the heart beat lasts 0.8 s. The contraction is such that the ejection fraction is normal (around 50%). The top part that would be attached to the atrium is constrained to zero displacement. On the epicardium, the effect of the pericardium is neglected and thus $P_{\mathrm{v}} = 0$. To investigate the effect of the contraction decoupled from the ventricular pressure, there is no valve in this model and the ventricle is unloaded ($P_{\mathrm{v}} = 0$ on the endocardium). On the fluid side, blood cannot enter into or leak from the ventricle (a null flux condition is applied on the whole boundary). Instead, blood enters in the myocardium from a distributed source with $p_a = 2.7\,\mathrm{kPa}$ which corresponds to a typical small artery pressure of 20 mmHg, and leaves through the venous side at a pressure of 10 mmHg modeled as a distributed sink with $p_v = 1.3\,\mathrm{kPa}$. The pressure differential across the capillary bed is thus of 10 mmHg. These values are consistent with literature data for the myocardium and skeletal muscles [Zinemanas et al., 1995, Kassab et al., 1999, Fronek and Zweifach, 1975]. The inverse of the volume resistance to flow from the small arteries and into the small veins is $3\,10^{-5}\,\mathrm{Pa^{-1}s^{-1}}$, chosen so that the average flow rate for the whole myocardium corresponds to 4% of a normal cardiac output [Berne and Levy, 2001]. The blood porosity ϕ_0 is 0.15 [Gonzalez and Bassingthwaighte, 1990, May-Newman et al., 2001], representing here the volume fraction of blood in the capillaries, which is ten times larger than the ones of the other small vessels [Ghista and Ng, 2007]. The permeability $\underline{\underline{K}}$ is isotropic and homogeneous with a scalar value of $2\,10^{-9}\,\mathrm{m^2Pa^{-1}s^{-1}}$ [Huyghe et al., 1992]. The simulation was run with a mesh of 15,000 elements.

The resulting time-averaged behavior is a system in which blood flows continuously from the small arteries into the capillaries, and from the capillaries into the small veins, at a

flow rate of $4\,\mathrm{mL\,s^{-1}}$, a mean pressure of 15 mmHg (2 kPa) and a muscle volume of 260 mL. Figure 2.7 shows the variation in time around this state. During contraction, myocardium volume decreases, while it increases during relaxation. This phenomenon has been reported in [Ashikaga et al., 2008] and references herein. Fibers contraction induces a rise of pressure. As a consequence, flow from the small arteries into the capillaries q_a is considerably reduced - which corresponds to the so called *flow impediment* ([Westerhof et al., 2006] and references herein) - and blood is squeezed out of the capillaries (lowering of m) into the small veins (rise of q_v). During relaxation, the opposite happens: m rises as q_a increases and q_v decreases, filling up the capacitance of the capillaries. The mainly systolic flow in the small arteries and mainly diastolic flow in the small veins are consistent with the measured velocities in small arteries and small veins in the left ventricle given in [Ghista and Ng, 2007].

Furthermore, as can be seen in Figure 2.8, pressure and mass vary nonlinearly across the myocardium wall. During contraction, pressure, and consequently flows as well, is more affected by the contraction in the subendocardium than in the subepicardium. The model is thus able to reproduce the fact that flow impediment is known to be higher in the subendocardium than in the subepicardium [Goto et al., 1991, Ghista and Ng, 2007]. In [28] we also show that the solution is heterogeneous in the different regions of the myocardium, which supports the choice of such a 3D model. During the cardiac cycle, the myocardium undergoes large deformation, e.g. here 24% at the apex.

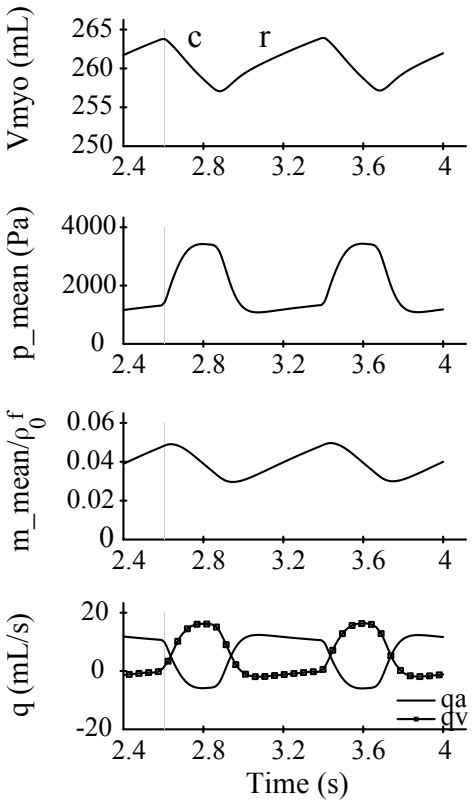

Figure 2.7: Variations over two cardiac cycles of myocardium volume with the contraction (c) and relaxation (r) phases, the pressure averaged over the volume, the added blood mass averaged over the volume, and the flow rates that come from the small arteries (q_a) and leave into the small veins (q_v).

2.2.4 Conclusion

We have proposed a poroelastic model accounting for large strains and compatible with incompressible conditions. The modeling, numerical implementation and some verifications were presented. A special emphasis was placed on the compatibility with thermodynamics principles (see [Chapelle and Moireau, 2014] for a more general formulation). The model has displayed an excellent behavior when used in the verification tests characteristic of essential poroelastic phenomena with large displacements and strains, including when undergoing complete drainage of the fluid. As far as cardiac perfusion is concerned, the major difficulty lies in the complexity of the physiological phenomena and the lack of sufficiently detailed measurements to validate the various modeling assumptions. Nevertheless, in spite of the relative simplicity of the model, the proposed numerical experiments have shown that important mechanisms of perfusion appear to be adequately captured. In particular, the results indicate that taking into account the ventricle cavity pressure is not necessary

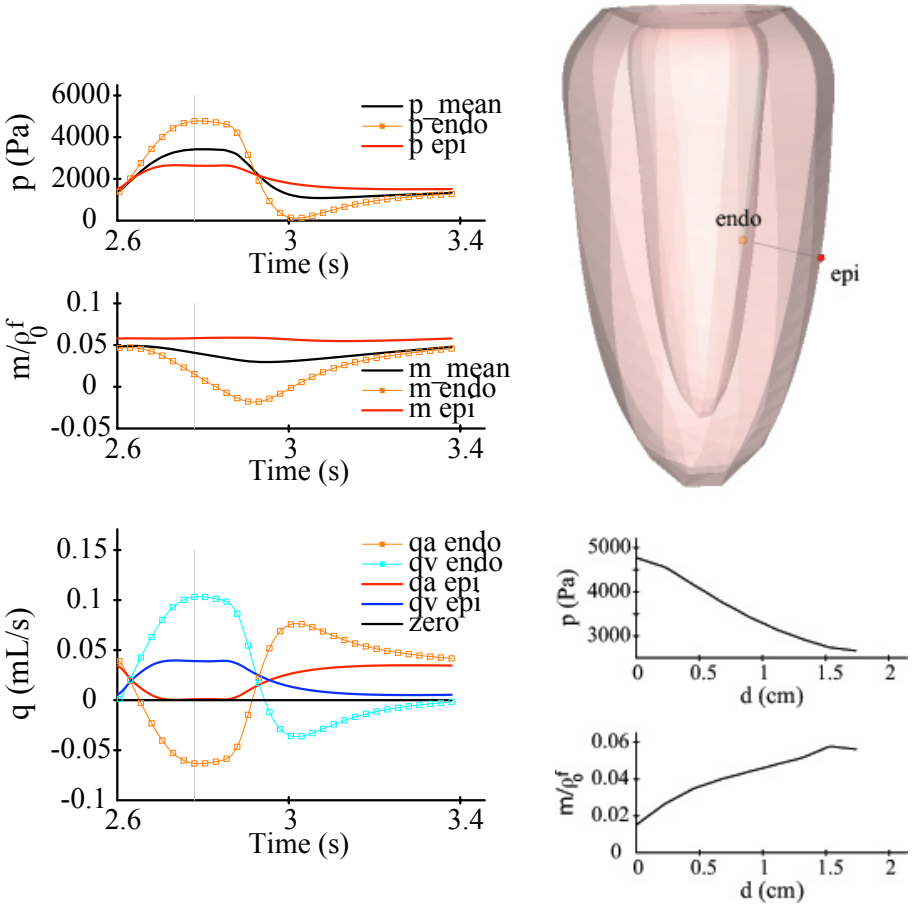

Figure 2.8: Mean pressure and mass traced over one cardiac cycle (upper left graphs). Pressure, mass, and arterial and venous flow rates traced for endocardium (endo) and epicardium (epi), at exact locations shown in the 3D figure. Pressure and mass gradients across the myocardium wall between these two points are represented on the lower right graphs (d is the distance from the endocardium point).

to model flow impediment during systole and to obtain a higher impediment in the endocardium than in the epicardium. At the time of [28], this 3D perfusion model represents a significant step forward of realistic simulations in a beating ventricle. We therefore believe that this model can be viewed as a tool to investigate the mechanisms of cross-talk between the myocardium and coronary flow, taking into account both the stresses generated by the contraction as in this study, as well as the effect of the left ventricular pressure. Cardiac perfusion modeling and simulation have since then gained more attention [Bradley et al., 2011, Cookson et al., 2012, Vuong et al., 2015].

The present study can be extended in many directions. For example: coupling of the porous flow with models representing the circulation in larger arteries (results not shown here); simulation of some characteristic pathologies, e.g. an infarcted area as reflected in a flow impediment combined with a decrease of local muscular contractility; modeling of the supply of the nutrients necessary for the cardiac muscle activity; transport and retention modeling of injected material [29, 30]; validation and calibration with clinical data.

2.3 Micro-scale flow modeling

At the micro scale, the exact vasculature geometry is even more difficult to access. Yet, if the spatial arrangement of tumor cells with their microenvironment is important, one may choose to explicitly represent the different components. Here, we focus on the blood vessels. One of the main steps from benign tumors to invasive cancer is a process called angiogenesis, i.e. the formation of new blood vessels. In this work [8], multiscale simulations of tumor growth are performed to study the influence of vascularization and angiogenesis on tumor cells development. The model includes the cellular (individual cells and vessels, development and death) and the molecular (oxygen, glucose and angiogenic growth factors reaction/diffusion) interplays. We show how experimental observations can be explained by the interplay of processes on the molecular and the cellular scale within a framework using individual-based models. More precisely, we explore the impact of angiogenesis on the growth dynamics of small tumors by direct comparison to situations where angiogenesis would not occur.

2.3.1 Tumor growth and angiogenesis modeling

In liquid suspension many tumor cells form multi-cellular spheroids. At small population sizes their radii grow exponentially as cell growth and division are unconstrained. They then show a transition from exponential to linear growth at a population size that vary with the cell types but at nutrient conditions similar to those in vivo. Such linear growth can also be found in-vivo, for example in xenografts of human NIH3T3 cells in the mouse model [Radszuweit et al., 2009] indicating a generic character of this growth law. In vitro growing multi-cellular spheroids form an approximately central spheroidal necrosis at about $400\mu m$ [Mueller-Klieser, 1987]. However, the linear expansion is almost unaffected by the formation of the necrotic core unless very unfavorable nutrient and oxygen conditions [Freyer and Sutherland, 1986]. This may be explained by a biomechanical form of contact inhibition as the key growth-limiting factor ([Drasdo and Höhme, 2003] and following papers). Freyer and Sutherland observed a significant slow down of the tumor expansion only if both, oxygen and glucose concentrations were low. Multicellular spheroids grow only up to about a millimeter in diameter. By contrast, tumors can grow to several centimeters. As the multicellular spheroids, the xenografts have a largely spherical shape but contrarily to spheroids they are well vascularized and in many cases show only modest necrotic and apoptotic figures. Hence the induction of new vessels permits growth of tumor cell population size up to about 3-4 magnitudes more than multi-cellular spheroids and, can avoid formation of a central necrotic core.

The in vivo situation is extensively described in [Marmé and Adam, 2008]. A tumor may grow up to a size of a few mm in diameter, nourished by oxygen and nutrients diffusing from the existing vasculature. This phase is often called the *avascular growth*; many aspects of this growth phase are extensively studied in-vitro by growing multicellular spheroids. A tumor can remain stable at that size. However, if as a consequence of their proliferation, tumor cells lack oxygen and nutrients, they can trigger several mechanisms to generate a higher density of blood vessels and thus increase their needed supply [Bergers and Benjamin, 2003], [Ribatti et al., 2003]. The main mechanism is the formation of new capillaries (angiogenesis), sprouting from existing vessels. Hypoxic and underfed tumor cells and other cells from the micro-environment secrete soluble factors, such as vascular endothelial growth factors (VEGF), that target the nearby blood vessels, make their endothelial cells proliferate, migrate, sprout and form a tube. In addition to these angiogenic factors, anti-angiogenic factors are also produced. The so called *angiogenic switch* occurs if growth factor promoters overbalance anti-angiogenic factors [Hanahan and Folkman, 1996]. New blood vessels are created towards the hypoxic regions of the tumor [Carmeliet, 2003]. Many cancer tissues have indeed extensive regions of hypoxia compared to normal tissue [Vaupel, 2004], usually associated with necrotic regions. This is due to the rapid growing of tumor mass that increases the distance between some cells and blood vessels, and to the non-functioning of some of the generated blood vessels (structural malformation, fluctuation in blood flow). A constant vessel network remodeling thus occurs, as the blood vessels inside the tumor may not be very functional (i.e. carry too low flow or experience too low wall shear stress), may collapse due to the high pressure generated by the surrounding proliferating tumor cells that cannot be counter balanced by a too unstable flow, or may die due to hypoxia or anti-angiogenic factors (see in addition the references to biological articles in [Bartha and Rieger, 2006] and [Mantzaris et al., 2004]).

Many aspects of tumor growth have been studied using mathematical models. In most cases deterministic models of the reaction-diffusion type or continuum mechanical models have been used (for comprehensive reviews see e.g. [Mantzaris et al., 2004, L.Preziosi, 2003, Roose et al., 2007]). They assume that growth is mechanically regulated [Ambrosi and Mollica, 2002, Byrne and Preziosi, 2003] or nutrient-limited (e.g. [Ward and King, 1997, Macklin et al., 2009]). They either describe how the solid tumor front grows (see e.g. [Byrne and Drasdo, 2009]), or how the density of the different components evolves in time and space (see e.g. [Wise et al., 2008, Preziosi and Tosin, 2009]). These are well suited to the description of large scale phenomena where the cell and tissue properties vary smoothly over a length scale of several cell diameters. In order to study small-scale phenomena or situations in which the properties of the cells vary over distances comparable to the size of a cell, single-cell-based models that describe each entity individually (for example, at the cellular level and individually how tumor and endothelial cells grow, divide, move and die) permit a higher degree of spatial resolution than models in which sub-cellular properties are replaced by locally-averaged quantities (for reviews, see e.g. [Drasdo, 2003, Anderson et al., 2007]). The different approaches have also been combined in hybrid or multiscale models, mostly in 2D. Examples include agent-based models for cells and continuum models [Schaller and Meyer-Hermann, 2005, Jiang et al., 2005, Alarcón et al., 2005, Kim et al., 2007, Welter et al., 2008] or simplified assumed profiles [Bartha and Rieger, 2006, Lee and Rieger, 2006] for diffusion of oxygen, nutrients and/or growth factors or inhibitors. Note that in [Kim et al., 2007] the different tumor zones were represented with either agent-based models or continuum models. The effect of the vasculature is explored with a given network [Alarcón et al., 2005] or includes angiogenesis and remodeling [Bartha and Rieger, 2006, Lee and Rieger, 2006, Macklin et al., 2009, Owen et al., 2009], angiogenesis being by itself an active subject of modeling (see e.g. [McDougall et al., 2006, Mantzaris et al., 2004, Capasso and Morale, 2009]).

The dynamic and the heterogeneous three-dimensional spatial structure of a tumor is thus

governed by a complex interplay of different components and scales (from gene expression changes to population competition at the tissue level). Here we model the key players of the first stages of the tumor growth: tumor cells, factors influencing them or secreted by them and the influence of and on the vascularization. The models consider the competition between contact inhibition-limited and nutrient/oxygen limited growth. For these questions it turns out to be sufficient to model individual cells within a cellular automaton model where the dynamics is rule-based. The advantage of this model type is that it permits efficient simulations at moderate computation time while the dynamics has been shown to be as for more detailed biophysically-related individual based models [Drasdo, 2005]. The subcellular scale of oxygen, nutrients and growth factors induces the choice of a continuum description of their respective conservation of mass. The diameter of a capillary is of the same order of magnitude as the size of the tumor cells. Therefore blood vessels are represented explicitly as discrete objects with a simplified hemodynamics reduced model relating flow and pressure inside them. Constitutive laws and threshold-based rules express the interplay between the different components of the system. This section aims at describing through modeling the key mechanisms of tumor growth rather than targeting a specific system for which more precise information would be needed to go beyond qualitative results, though parameters were chosen to be as realistic as possible to obtain relevant macroscopic behaviors.

2.3.2 The multiscale model and numerical methods

For the precise equations and parameters of this hybrid multiscale model, see [8]. We now briefly describe each model block (fig. 2.9). The stochastic agent-based model is a cellular automaton model defined by a set of rules on cell position, cell cycle and replication, growth, division and necrosis, affected by local oxygen and glucose concentrations. The time evolution of the system is computed using the Gillespie algorithm [Gillespie, 1977] assuming that the underlying system dynamics of the multi-cellular system can be modeled by a master equation for the multivariate probability distribution to find the configuration of the whole system at every time step X, where $X = \{x_1, x_2, ...\}$ denotes the state vector of the multicellular configuration. One way is to enumerate all lattice sites and denote by x_k the state vector of the cell localized at lattice site k. If this lattice site is empty, the state is zero. The dynamics is then formalized by

$$\frac{\partial \mathcal{P}(X,t)}{\partial t} = \sum_{X'} (\tau_{X' \to X})^{-1} \mathcal{P}(X',t) - (\tau_{X \to X'})^{-1} \mathcal{P}(X,t). \tag{2.29}$$

$\mathcal{P}(X,t)$ is the probability of the system being in configuration X at time t. The possible transitions from this X into another configuration X' are denoted by rates $(\tau_{X \to X'})^{-1}$ for each process (cell growth, division, and death). A process is then chosen with a probability that corresponds to its relative weight, calculated as the rate for this process divided by the sum of the rates for all other processes. To eliminate fluctuation effects that emerge from individual time evolution paths observables are averaged over many realizations.

The nearby vasculature releases oxygen and glucose that diffuse in the local environment and nourishes the tumor. This behavior is described by a reaction-diffusion equation, where the concentration is set at the blood vessel nodes, and cells represent distributed sinks. These cancer cells consumption rates of glucose and oxygen are coupled non-linear terms. Similarly, VEGF is released by the (hypoxic) necrotic cells and diffuses into the tumor environment.

The models for the vascularization and its adaptation to the micro-environment are largely inspired by the models of [Bartha and Rieger, 2006, Lee and Rieger, 2006], and part of the stochastic agent-based model above. The preexisting network of vessels is generated on the random lattice, common with the tumor cells. Flow through a vessel and pressure at the nodes are computed based on the simplest resistance law (Poiseuille law, see section 2.1.3).

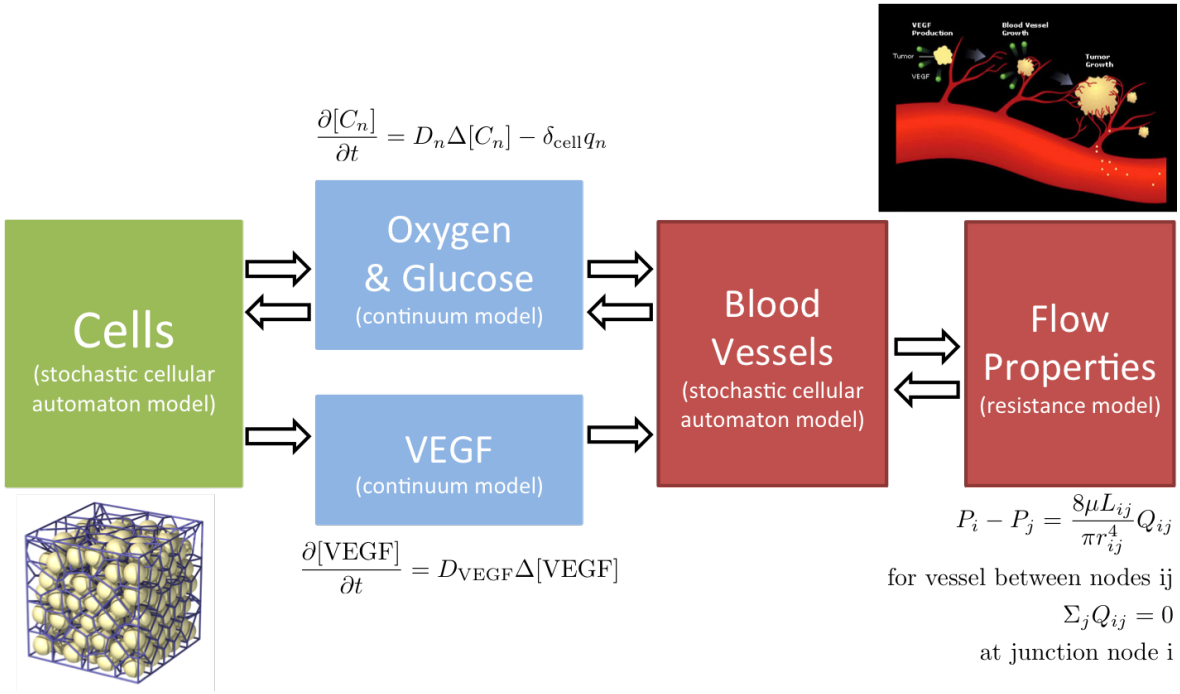

Figure 2.9: Components of the hybrid multiscale tumor model and their relations. Upper right: schematic showing tumor growth (yellow), sending growth factors (green) triggering growth of new blood vessels (from http://www.medivizor.com).

Pressure is prescribed as a boundary condition at the entrances and exits of the network, and solved at nodes using conservation of mass and continuity of pressure at each junction. Shear stress in the vessel is also calculated. A sprout can form from a blood vessel according to certain rules, and in particular if the growth factor concentration is higher than the threshold that characterizes the angiogenic switch. Within the living tumor zone (proliferating and quiescent zones), blood vessels cannot sprout but they can dilate due to proliferation induced by growth factors. In contrast, under-perfused vessels can also collapse due to the high pressure generated by the proliferation of tumor cells or disappear because they are not functional enough and thus experience themselves hypoxia, or are sensitive to the anti-angiogenic factors. This is modeled by the collapse of a vessel if its shear force is too low and the density of tumor cells is too large. The vessel can also be removed if the flow is zero and the local concentration of oxygen is too low. The vascular network responds to the changes of the local micro environment by angiogenesis or remodeling. The local radius, pressure, flow and shear values are thus continuously updated. In turn, the changing vascular network influences the growth of the tumor as explained in the cellular model above.

From an algorithm point of view, at each new event as defined by the Gillespie algorithm (i.e. cell death, vascular sprouting, etc.) the blood flow model is updated (pressure, flow, shear stress) and then the nutrients and growth factor reaction-diffusion equations are updated and solved. State transition probabilities are then computed for the vascular network and the cells, before a new event is computed to occur.

2.3.3 Numerical results

We study the interplay of biomechanically induced contact inhibition, i.e. inhibition of cell division by mechanical stress exerted from surrounding cells, and oxygen/nutrient limitation on the growth kinetics of tumors in three cases: (1) tumor growth that is not constrained by the lack of oxygen or nutrients as it can be partly observed in monolayers and the early

avascular phase of tumors or multi-cellular spheroids growing in-vitro, (2) tumor growth in a *static* vascular network, where neovascularization does not occur and, (3) tumor growth in case the tumor cells can induce the formation of new vessels.

In Figure 2.10 left, the radius of the tumor is plotted versus time for three cases: (1) with neither oxygen nor nutrient limitation, (2) with nutrient limitation but without the angiogenic switch, and (3) with nutrient limitation and angiogenesis. In the "no limitation" scenario, all cells can divide and the tumor thus first expands exponentially (zone a of Figure 2.10 left). After some time, the cells in the center cannot divide anymore due to contact inhibition and they become quiescent. When the proliferating rim reaches a constant thickness, the radius becomes a linear function of time (zone c of Figure 2.10 left). For the two other simulated scenarios there is *nutrient limitation*: oxygen and nutrients are supplied by sources (blood vessels) and diffuse out of them in the interstitial space but they are also locally consumed by the cells. As the tumor mass expands, there is a first period where demands are lower than supplies (as seen by the superposition of the three curves in zone a of Figure 2.10 left). Then, supplies cannot balance demands anymore, due to an increasing consumption: this is the *nutrient limitation* phase. This slows down the growth of the tumor, as can be seen by the decreasing slope in zone b of curves (2) & (3) of Figure 2.10 left. After some time, the angiogenic switch occurs and enables the tumor to expand with a higher speed as indicated by the higher slope of the curve (3) compared to curve (2) in zone c of Figure 2.10 left: its demands of oxygen and nutrients are better fulfilled. Note that this slope is here as high as the one of the *no limitation* scenario, since the latter constitutes an upper bound to the growth speed. If angiogenesis is not made strong enough, then lower slopes are obtained.

In addition to the tumor size, its structure varies significantly with the different environmental conditions. When there are neither oxygen nor nutrient limitations (Figure 2.10 1a&b&c, 2a, 3a), cells are either proliferating (yellow) or quiescent (green), but none of the cells are necrotic. In contrast, when oxygen or nutrients are lacking because their diffusions from blood vessels are not fast enough and their local concentrations are too low, necrotic cells (blue) appear in the center (Figure 2.10 2b&3b). As a response to hypoxia and hyponutrition, cells produce growth factors that diffuse through the tissue, reach the existing blood vessels and finally trigger sprouting from them to create new blood vessels (Figure 2.10 3c). If no new blood vessels are created, the necrotic zone increases (blue region in Figure 2.10 2c larger than in Figure 2.10 3c, where only little necrosis can be observed). Note the quiescent zones around the blood vessels inside the tumor (Figure 2.10 2c&3c): in these regions, there is enough oxygen and nutrients for the cells but they cannot divide due to contact inhibition of growth. As time goes, the case without limitation continues to grow with a spherical shape and without any necrosis (Figure 2.10 1c). In the limited case, the tumor continues to grow, although it tries to grow towards or along blood vessels (Figure 2.10 2c). In the angiogenic case, new vessels are forming towards and inside the tumor (Figure 2.10 3c) as it continues to grow with a speed closer to the no limitation case (Figure 2.10 left).

2.3.4 Conclusion

In all cases we found the tumors to grow approximately spherical so the expansion can be quantified by studying the time development of the tumor radius. The latter grows exponentially fast for small times changing to linear growth later on. This is precisely what could be observed in monolayers, multi-cellular spheroids and in xenografts. The existence of linear growth is closely related to a proliferating rim of constant size. In case (1) the speed of growth is controlled by a biomechanical form of contact inhibition (e.g. [Drasdo and Hoehme, 2005] and refs. therein) explained by the degree of compression of cells within the tumor caused by the local pressure within the tumor tissue. During tumor expansion this pressure profile

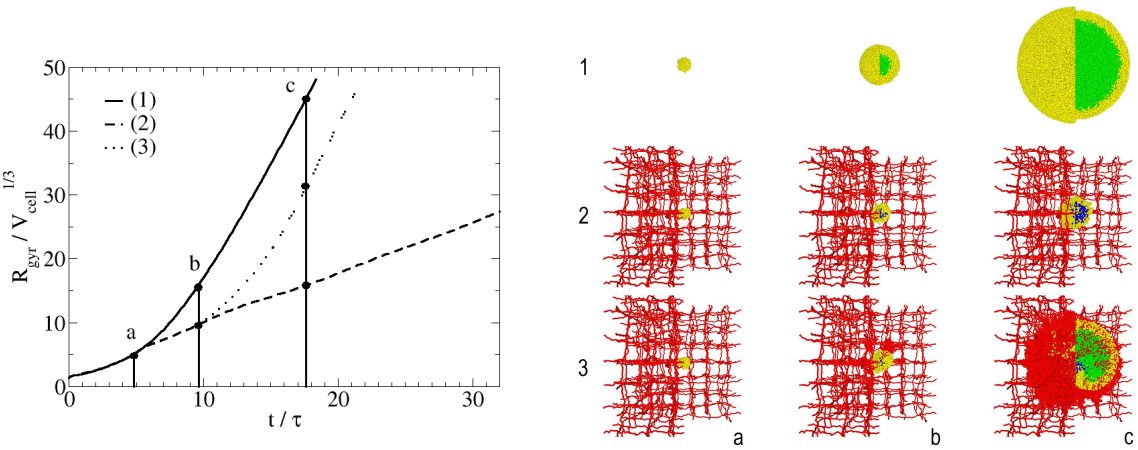

Figure 2.10: Left: time evolution of the radius of a tumor cell population for the three different scenarios. Right: screenshots from the simulations at times $t/\tau = 4.8$ (*left*), $t/\tau = 9.6$ (*center*) and $t/\tau = 17.6$, τ being the cell-cycle time (*right*). Each figure is composed by an exterior view on the left-hand side and a central-cropped view of the simulated domain on the right-hand side. The colors indicate proliferating (*yellow*), quiescent (*darkpastelgreen*) and necrotic cells (*blue*) as well as blood vessels (*red*). The upper sequence shows the reference simulation of growth without any nutrient limitation (1). The lower sequences show the scenarios of nutrient limited tumor growth in vascularized tissue without (*center*, (2)) and with angiogenesis (*bottom*, (3)).

increases from a small value at the tumor border (marking the outer border of the proliferating rim) towards a value at which cell proliferation is contact inhibited (marking the interior border of the proliferating rim). In case (2) the speed of growth is controlled by at which penetration depth the concentrations of the oxygen and nutrient fall below the value necessary to permit cell proliferation. This case is representative of an anti-angiogenesis drug, which lowers the growth speed but does not necessary stops tumor progression. In case (3) angiogenesis after its onset generates sufficient new blood vessels so that oxygen and nutrient supply is - after a short transient - not limiting: the tumor grows with the same speed as in the oxygen/nutrient-unlimited case (1). Moreover, in case (3) we find only modest mitotic figures. Both, the linear growth and the modest mitotic figures have been observed in xenografts of NIH3T3 cells which are well vascularized [Schiffer et al., 2003].

Although this work [8] reproduced known interplays between tumor cells and their microenvironment, in particular blood vessels, the parametrization of such model from in-vivo data remains a challenge. Recently we successfully parameterized the components that can be accessed in-vitro [31]. In this article, we develop a quantitative single cell-based mathematical model for multi-cellular tumor spheroids (MCTS) of SK-MES-1 cells, a non-small cell lung cancer (NSCLC) cell line, growing under various nutrient conditions: we confront the simulations performed with this model with data on the growth kinetics and spatial labeling patterns for cell proliferation, extracellular matrix (ECM), cell distribution and cell death. We start with a simple model capturing part of the experimental observations. We then show, by performing a sensitivity analysis at each development stage of the model that its complexity needs to be stepwise increased to account for further experimental growth conditions. We thus ultimately arrive at a model that mimics the MCTS growth under two conditions to a great extent (fig. 2.11). Interestingly, the final model, is a minimal model capable of explaining all data simultaneously in the sense, that the number of mechanisms it contains is sufficient to explain the data and missing out any of its mechanisms did not permit fit between all data and the model within physiological parameter ranges. Finally, the model is constructed on

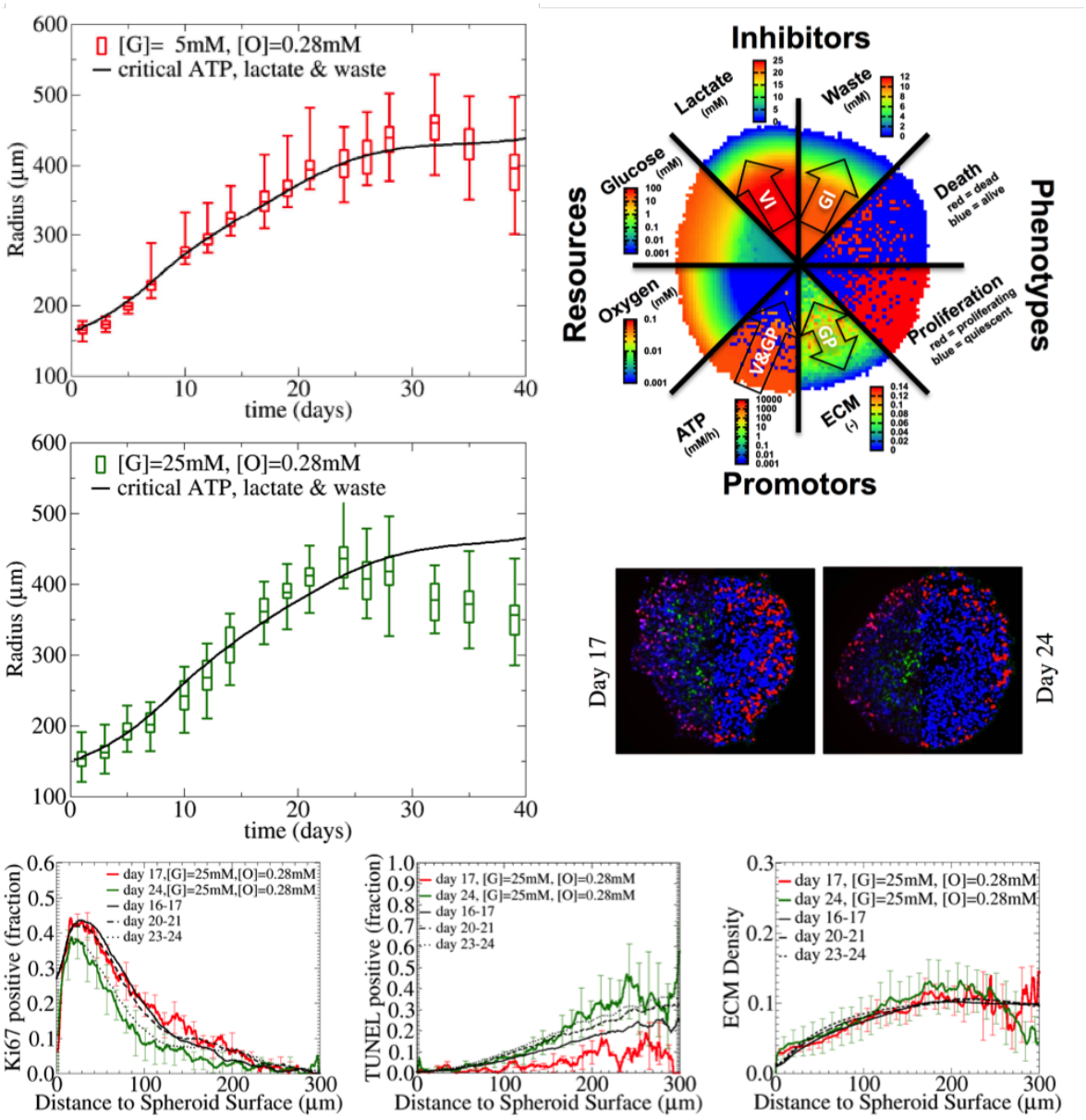

Figure 2.11: Growth dynamics (two left graphs) and spatial organization (bottom 3 graphs) found in experiments (labeled in legends with [G] and [O]) are well captured by the hybrid model. Simulations reveal spatio-temporal structures for cellular and sub-cellular contents (upper right picture) not easily measurable in experiments. Two spheroid cuts stained for Ki67 positive cell (proliferation, red), TUNEL positive cells (apoptotic cells, blue) and collagen V as a marker for extra-cellular matrix (ECM, green) are shown after image processing (middle right) as inputs for quantitative image analysis (red and green curves in the bottom graphs).

two nutrient conditions but further predict well growth of two other very different nutrient conditions (fig. 2.12).

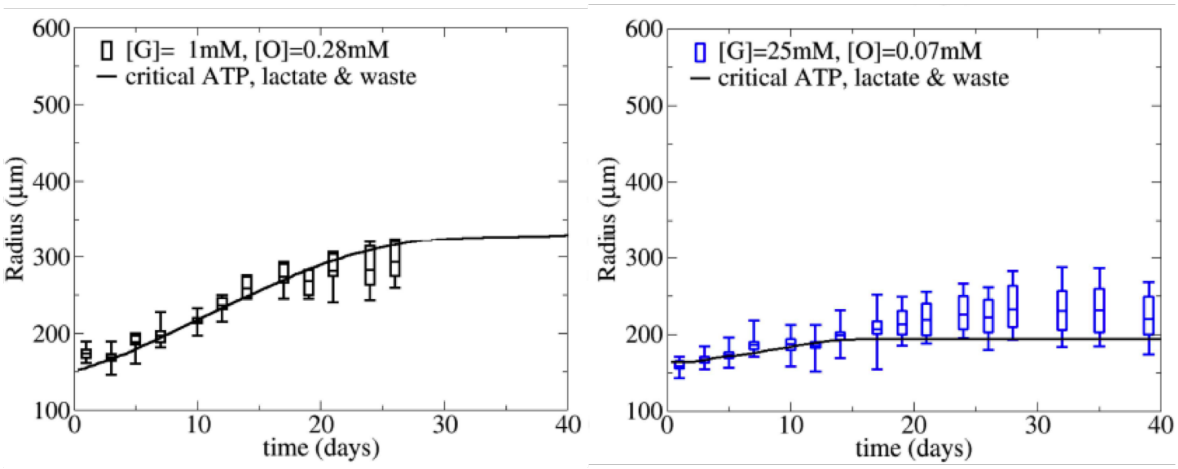

Figure 2.12: Predicted growth dynamics (solid line) of two very different nutrient conditions and validation with experimental data (labeled in legends with [G] and [O]).

Current work consists in understanding how to extract vascular parameters (architecture and function) from invasive histological information from biopsies or tissue resection and non-invasive in-vivo imaging (see 5.1). An extension of the model could be to take into account the fluid interaction between the vascular network and surrounding interstitial fluid, as well as transport phenomena [Cattaneo and Zunino, 2014]. Interesting questions are also how to derive continuum models (important to capture in-vivo tumor sizes) from agent-based models, and to mathematically study their different regimes [32].

3

Numerical methods for multidomain coupling and instability treatment of multi-branched Navier-Stokes simulations

Flow is simulated in branched geometrical models in a number of engineering applications, including the modeling of blood and air in their larger conduits. In these applications, 3D Navier-Stokes simulations (section 2.1.1) can only be realistically carried out in a few branches, while the rest of the circulation or respiratory system, represented by reduced models (section 2.1.3), must be taken into account through appropriate coupling conditions (section 3.1). Several strategies exist to couple these different models, and this topic constitutes a continuing matter of research. In this work, the coupling is done implicitly (with a monolithic solution strategy described in [21, 11]) or explicitly [24]. The former is numerically more stable while the latter more modular, especially for closed-loop models of the circulation. We have recently proposed an approach that combines these two features [33]: a quasi-Newton approach is devised such that the contribution of the reduced model to the 3D domain is taken into account in the tangent matrix of the nonlinear Navier-Stokes solver, without adding a new iteration loop. Section 3.2 concentrates on the proposed implicit approaches. Flow at the boundaries where the velocity profile is not prescribed, is often complex, an interplay between patient-specific geometry and fluid dynamics (Reynold number, inertia, ...). Due to this or to physiological flow rate time oscillations, flow reversal can occur at the coupling boundaries, inducing numerical instabilities. This is enhanced in airflow, where inflow occurs at the trachea during inspiration and a large flow reversal happens at the distal branches during expiration. The kinetic energy of the flow is not controlled at the continuous level and hence it might lead to numerical instabilities at the discrete level. Several remedies have been proposed and compared (section 3.3, [34, 16]), in particular the inertial boundary stabilization and a novel modified Navier-Stokes approach. These solution methods are tested on typical flow geometries and on realistic cardiovascular and airflow application cases.

3.1 Multidomain approaches

The three-dimensional Navier-Stokes simulation of blood or air flow in large conduits requires inlet and outlet boundary conditions that represent dynamics at these locations (section 2.1). However, in patient-specific settings, pressure or velocity are rarely clinically measured exactly there, or they can be part of the desired output [3]. Thus, boundary conditions are usually substituted for transmission conditions with reduced models of the rest of the circulation or respiratory system. This typically involves coupling to 1D models (e.g. [Formaggia et al., 2001, Blanco and Feijoo, 2013, Oshima et al., 2012, Ismail et al., 2014] [11]), themselves often coupled to 0D models, or directly to simple lumped parameter 0D models (e.g. [13, 5, 20, 19, 15] [Prasad et al., 2011, Fouchet-Incaux, 2014]) or airway tree based reduced respiratory model [Baffico et al., 2010, Ismail et al., 2014, Ismail et al., 2013a] and closed loop hemodynamics 0D models (e.g. [35, 25, 36], [Migliavacca et al., 2006, Blanco and Feijoo, 2013]). This coupling methodology transfers in various forms pressure and flow rate between 3D and reduced models, for which there is a loss of information (section 3.2).

The importance of applying proper boundary conditions to achieve physiological results is demonstrated in our work first in hemodynamics in 1D [21], then in 3D [11, 3]. In [13] we show several examples where taking into account non-periodicity changes the results. In mechanically ventilated respiratory flow, we make evident that the dynamics in the 3D domain is driven by the choice of reduced model, which permits to model diseases such as emphysema [15, 18]. The number of papers that have emerged in the last 10 years on boundary conditions in hemodynamics and respiratory flows highlights the importance of this topic.

3.1.1 3D model coupled to a 0D model of the heart and distal vasculature

These three papers [37, 38, 35] present a number of modeling and computational tools to simulate blood flow and pressure in deformable patient-specific models of the aorta and the

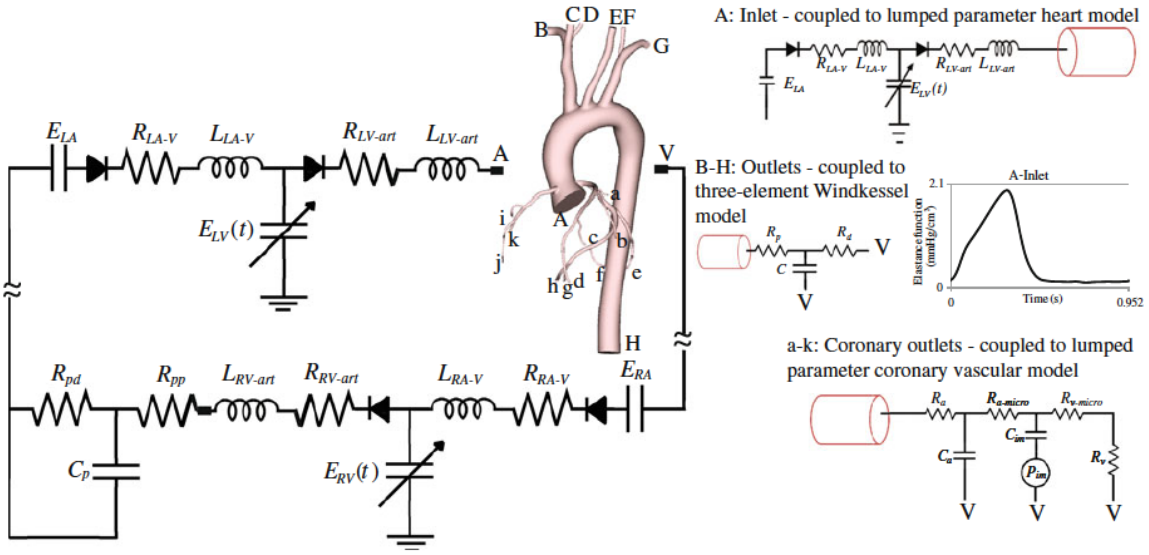

Figure 3.1: 3D-0D coupling for simulations of blood flow in a thoracic aorta model with coronary outlets driven by a heart model. Note that all the outlets of the three-dimensional computational model feed back in the 0D model at (V).

coronary arteries (feeding the heart). Using a 0D coronary vascular model along with the inflow boundary condition that couples the 0D heart model and the almost closed loop system of the circulation (fig. 3.1), we can predict coronary flow and pressure realistically using anatomic data obtained from medical imaging techniques and study how changes in cardiac and arterial properties affect coronary flow and pressure and vice versa. This could not have been studied without coupling of the 3D domain with heart and distal 0D models. Rest and exercise conditions are studied, and flow reduction due to stenosis severity predicted (fig. 3.2). It would be interesting to couple this model to the poroelastic model of the heart muscle studied in section 2.2, so that the heterogeneous action of the heart contraction on the vessels can be taken into account in the various coronary sub-trees.

3.1.2 Predictability enhanced by 3D-closed loop model of the entire circulation

In a first step to study different virtual surgical designs in congenital heart disease, simulations have been run with hypotheses on the boundary conditions [5]. Outlet boundary conditions are kept unchanged compared to preoperatively, state for which they are designed based on patient-specific clinical measurements as described in section 4.2. At the outlets, a relationship between pressure and flow is prescribed, so both could

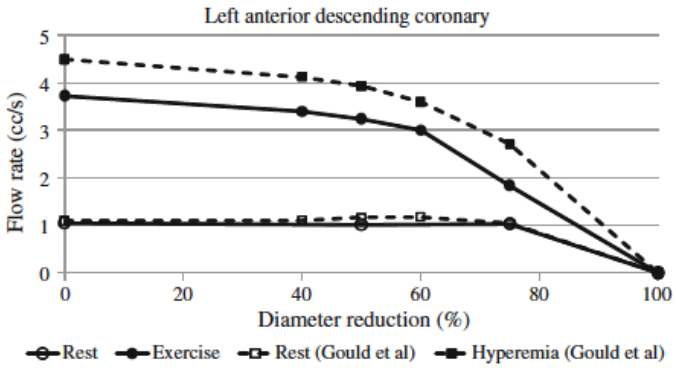

Figure 3.2: Prediction of flow changes with severity of coronary stenosis. Comparison with experimental data from Gould et al.

adapt to the virtual surgery where a graft was connected in different ways to the preoperative geometry and thus bringing additional flow. By contrast, flow rates are prescribed at the inlets based on preoperative PC-MRI measurements boundary conditions and hypotheses on how they might change from preoperatively to postoperatively. To rather predict these inflow changes, a closed-loop 0D model of the entire circulation is thus tuned for one patient to its MRI, ultrasound and catheterization pressure measurements and coupled to the 3D model [24]. Results show that flow rates at both inlets (SVC, IVC) changed from the preoperative to the postoperative states, in coherence with physiological knowledge. Of course, the closed-loop model presents many parameters that are not easy to tune based on clinical measurements section 4.3, and it remains to be validated that the parameters do not change significantly due to the surgery, but such an approach enhances the predictability potential of virtual surgeries. Other examples where a closed-loop model of the circulation has been necessary for the application at hand include optimization study of a shunt for single-ventricle stage 1 surgery [34], comparison between two different surgical approaches at the second stage [4] and surgical planning study of different patients [Kung et al., 2013, 40].

3.2 Numerical coupling strategies

The coupling between the 3D domain and the reduced order model must ensure conservation of mass – which imposes constraints on flow rates –, and continuity of pressure or normal stress. However, it is known that this can lead to the imposition of so called *defective* boundary conditions, i.e. where only mean values are known on a boundary [Formaggia et al., 2002a, Veneziani and Vergara, 2005, **?**]. Besides, it can generate problems of well-posedness [Formaggia et al., 2002a, Quarteroni and Veneziani, 2003]. Numerically, coupling between the 3D domain and a lower order 1D or 0D model can be solved using either a monolithic or a partitioned approach. We here summarize the approach in [21, 11] and the later discussion in [33].

3.2.1 The multidomain formulation and its monolithic resolution

In a monolithic approach, the complete coupled system is solved simultaneously, either by analytic implementation of the lower order model, or by numerical integration. A simple 0D model with a known analytical solution can be directly implemented inside the 3D solver as a *hard coded* boundary condition, with a monolithic implementation of the Dirichlet-to-Neumann operator [11].

The Dirichlet-to-Neumann (DtN) method [Givoli, 1992] is one method among many (substructuring, boundary integral and element methods, infinite elements, artificial boundary conditions, and filtering schemes) that reduces a very large or infinite problem to a bounded and numerically tractable domain. It has the main advantages of providing an exact boundary condition at the truncation of the domain, of being compatible with standard finite element or finite difference methods and of not requiring the original domain to be 'regular' (i.e. homogeneous, isotropic and governed by linear equations). The idea is the following. After having introduced an artificial boundary, the domain is cut into the domain of interest and the rest of the domain. In the latter, the PDE solution is solved analytically, providing a relationship at the artificial boundary between the Dirichlet and the Neumann conditions, defining the so called *DtN map* or *Steklov-Poincaré operator*. The PDE is then solved in the domain of interest with this DtN boundary condition.

We have applied this method to derive the *multidomain* method in 1D [21] and in 3D [11, 13]. Note that here the artificial boundary condition is not exact because the equations in the analytical domains are simplified versions of the ones in the numerical domains. In other words, in addition to the usual geometric complexities that are encountered in many physics

or engineering problems, we are facing mathematical complexities for blood and respiratory flow problems: neither the 1D nor the 3D equations of blood flow can be solved analytically in the far-field domains (arterial trees and rest of circulation). We therefore use simpler mathematical models that can be solved analytically or semi-analytically to represent the physics in these domains. For each model, we derive the equivalent to the DtN map, as a relationship between flow and pressure (in the 1D case) or between pressure (or normal traction) and velocities (in the 3D case).

Monolithic implementation of open-loop coupled boundary conditions, such as resistance, Windkessel (RCR), impedance, or simple heart models, in which the relation between the pressure and the flow rate of this boundary is precisely known, has been demonstrated for up to second order ODEs, including coronary artery models [13, 41, 38] & section 3.1. However from a practical point of view, any modification to these hard-coded boundary conditions requires detailed end-user knowledge of the 3D solver and intrusive implementation. A modular, and easily modifiable system for coupling an arbitrary 0D model network to a 3D solver is therefore desirable, as it increases applicability to a variety of disease applications, and does not require end-user modification of the 3D solver. Similarly, when the 0D network is more complex, leading to higher order or nonlinear networks of ODEs or coupling of multiple outlets the DtN operator must be computed numerically if there is no analytical solution for the ODE system. The monolithic coupling approach has been compared in detail to its explicit-in-time counterpart, in the context of fractional step methods [Bertoglio et al., 2013]. The monolithic solution of such a 3D-0D coupled system requires a significant change in the 3D solver, and may lead to an ill-conditioned numerical system, unless proper care is taken for its preconditioning [Urquiza et al., 2006, Blanco et al., 2007].

3.2.2 A strongly coupled iterative multidomain formulation

An alternative to the fully coupled monolithic schemes is the partitioned approach, which has been the focus of much work in the last decade. In the partitioned approach, having a separate solver for the 0D domain enables us to relate flow rates and pressures at the coupled boundaries for any arbitrary closed-loop, high order, nonlinear 0D model. Such an approach facilitates the use of existing solvers and allows for the use of different numerical schemes in the 0D and 3D domains. With the partitioned approach, coupling in time between the 3D and the reduced (0D or 1D) domains can be either explicit, at one extreme, or implicit at the other. This choice may be motivated by the time-step requirement of the Navier-Stokes solver, which must be sufficiently small to use an explicit method [Quarteroni et al., 2001], or by issues of numerical stability. Several recent studies have used a partitioned approach with implicit staggered schemes. Gauss-Seidel schemes has been found to require too many sub-relaxation steps for realistic values [Urquiza et al., 2006]. Some partitioned strategies have used a general heterogeneous coupling approach in which average quantities are passed at the interface [Leiva et al., 2010, Malossi et al., 2011], with two nonlinear iteration loops required in the former. These studies also advocated use of Newton methods to achieve convergence. In another previous study, a cycle by cycle open-loop simulation was used, and the outlet boundary conditions were corrected to re-balance outlet flow rates [Johnson et al., 2011]. Despite this recent work, the effectiveness of an iterative implicit coupled approach with complex closed-loop 0D models, in which simultaneous temporal data in the 0D model is required, has not been established yet. As noted in [Quarteroni et al., 2001], these systems may suffer from ill-conditioning, and special care must be taken to ensure numerical stability.

In this work [33], a time-implicit approach is proposed to couple the Navier-Stokes equations solved in the 3D domain, to complex closed-loop 0D models. This overcomes current limitations related to the numerical instability and restrictive time step choices. The contributions of the coupling to both the tangent matrix and the residual vector are evaluated with an independent code. The DtN operator is thus numerically, rather than analytically,

determined. With proper communication protocols between the two domains, this approach provides much higher flexibility for modeling the entire circulatory system, with no requirement for modification or intrusion into the 3D solver, once the coupling framework has been implemented. In particular it avoids invasive changes in the 3D solver when the reduced model is changed, both of which are difficult for end-users with complex reduced models that are becoming more and more common practice for cardiovascular and pulmonary applications. Hence this method incorporates attractive features of both monolithic and partitioned approaches. The adopted time discretization scheme is second order accurate or higher, and allows both domains to be marched in time simultaneously using a *predictor-corrector* algorithm. This facilitate use of an implicit integration scheme in the 0D domain. We also aim to overcome previous restrictions that required use of only Neumann boundary conditions in the 3D domain, by expanding our formulation to include Dirichlet coupling. This offers greater flexibility in choosing 0D model components, yet maintains the well-posedness of the problem. In previous partitioned approaches, coupling with Dirichlet boundary conditions used a Lagrange multiplier method, requiring appropriate numerical strategies to solve the 3D system, and increased computational cost [Kim et al., 2009], [34]. Here, the coupling is applied as a Dirichlet condition, with a chosen velocity profile. The coupling term in this case is not strictly a part of the variational formulation, since it is an essential boundary condition that changes at each nonlinear iteration of the 3D solver, according to the 0D numerical solution.

We therefore propose an implicit in time coupling algorithm (fig. 3.3). Depending on the reduced model, the coupling variables may vary. If flow information is received from the reduced model, it is applied to the 3D model as a Dirichlet boundary condition (defining η_g), and sends back pressure at this outlet to the reduced model at each nonlinear iteration of the Navier-Stokes quasi-Newton solver. If pressure information is received from the reduced model, it is applied to the 3D model as a 'Neumann' boundary condition (defining η_h), and sends back flow at this outlet to the reduced model. We note that due to the coupling this boundary condition is not strictly a classic Neumann condition. In fact in this case, a quasi-Newton approach is devised such that the contribution of the reduced model to the 3D domain is taken into account in the tangent matrix of the nonlinear Navier-Stokes solver. In our formulation these data are indeed exchanged between the two domains at each Newton iteration of the nonlinear Navier-Stokes solver to ensure convergence of both domains simultaneously. This contribution is computed by finite differences.

We present next the general idea of the algorithm (see [33] for more precisions on the implementation). At the start of the simulation, the 0D and 3D domains are initialized with the 0D state variables $\boldsymbol{\mathcal{X}}^1$ and 3D velocity and pressure $\{\boldsymbol{U}^1, \boldsymbol{P}^1\}$, respectively. In the generalized-α time discretization method, the solution at n is fixed and the solution at $n+1$ is corrected after each nonlinear Newton-Raphson iteration [Jansen et al., 2000]. In each time step, from n to $n+1$ in the 3D domain, the following steps are performed:

1. Predict unknowns at time step $n+1$ and iteration k^{th} in the 3D domain based on the solution at time step n,

$$k = 0, \boldsymbol{U}_{(k)}^{n+1} = \boldsymbol{U}^n, \boldsymbol{P}_{(k)}^{n+1} = \boldsymbol{P}^n.$$

2. Compute the flow rate, $\{Q_i^n, Q_{i(k)}^{n+1}\}\ \forall i \in \eta_h$, and averaged pressure of coupled boundaries, $\{\mathcal{P}_i^n, \mathcal{P}_{i(k)}^{n+1}\}\ \forall i \in \eta_g$, and pass them to the 0D domain.

3. After receiving the flow and pressure data at time steps n and $n+1$ in the 0D domain and retrieving $\boldsymbol{\mathcal{X}}^n$ as the starting point of integration, integrate the ODE's up to $n+1$.

4. After receiving $\mathcal{P}_{i(k)}^{n+1}\ \forall i \in \eta_h$ and $Q_{i(k)}^{n+1}\ \forall i \in \eta_g$ from the 0D domain, calculate the traction at the coupled Neumann boundaries and the nodal velocities at the coupled Dirichlet boundaries, respectively.

5. Compute the residual and tangent matrix coupling contributions below, and solve the linearized Navier-Stokes equations to find $\Delta \boldsymbol{U}$ and $\Delta \boldsymbol{P}$:

$$\begin{aligned} &(R_m)_{Ai} \leftarrow (R_m)_{Ai} + \textstyle\int_{\Gamma_j} N_A \mathcal{P}_j^{n+1} n_i \mathrm{d}\Gamma,\ j \in \eta_h, \\ &\tilde{K}_{AiBj} \leftarrow \tilde{K}_{AiBj} + \frac{\partial (R_m)_{Ai}}{\partial Q_l^{n+1}} \frac{\partial Q_l^{n+1}}{\partial U_{Ck}^{n+1}} \end{aligned} \tag{3.1}$$

where $N_A(\boldsymbol{x})$ is the shape function for node A and $i \in \{1, \cdots, \text{number of spatial dimensions}\}$.

6. Correct velocity and pressure in the 3D domain

7. Set $k \leftarrow k+1$ and go back to the second step if the residual is not small enough, $||\boldsymbol{R}|| > \epsilon$, or the number of iterations exceeds the maximum specified value, $k > k_{max}$.

8. Before going to the next 3D-domain time step, calculate $\boldsymbol{\mathcal{X}}^{n+1}$ based on the corrected flow rate and pressure. Then set $n \leftarrow n+1$ and go back to the first step.

Compared to the method implemented in [Quarteroni et al., 2001], the coupling in our approach is implicit in time (fig. 3.3). This framework offers thus the flexibility to use either an implicit or explicit time-integration method in the 0D domain. Note that for the Neumann-type coupling, the velocity profile is not enforced. Flow at these coupling boundaries is often complex, as a result of the interplay between geometry and flow conditions elsewhere in the 3D domain. Due to this or to physiological flow rate time oscillations, flow reversal can occur at the coupling boundaries that usually rapidly lead to numerical instabilities (see section 3.3).

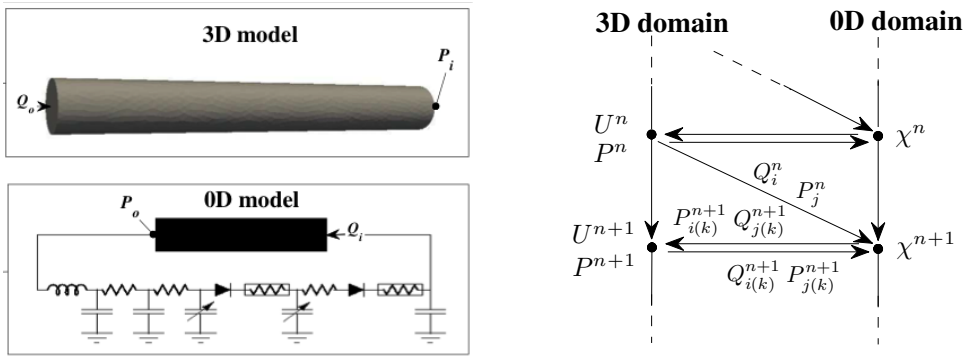

Figure 3.3: 3D-0D multiscale example. Left: 3D domain (1 inlet i with Neumann coupling, one outlet o with Dirichlet coupling), 0D model (closed loop). Right: implicit coupling algorithm at time step $n+1$, via Neumann (average normal traction related to the 0D pressure, P) or Dirichlet (velocity U imposed in the 3D domain, from the flux Q in the 0D domain) 3D domain boundary condition at iteration k. χ is the 0D state variable vector.

We summarize here the main results found in [42]. After a successful verification example by comparison to the analytic solution and the monolithic multidomain approach of [11], results for this multidomain framework then include a comparison of various contributions to the tangent matrix of the reduced model in the 3D-closed loop 0D example shown in fig. 3.3 left, but with Neumann couplings at both ends. A static contribution is found the best trade-off to obtain convergence with different meshes and time-steps. This indicates that the time-accumulated contribution of the nonlinear 0D components in a cardiac cycle is negligible compared to the linear components. Results also show that the Dirichlet coupling case (at both ends) is more robust, but it necessitates the prescription of the velocity profile at the

coupling boundaries. Besides, inductors have to be added at the coupling boundaries to obtain a stable coupling (the coupling pressure received from the 3D domain is then a source term for the 0D dynamical system). Finally, this iterative coupling strategy is successfully tested on realistic cardiovascular and airflow cases [42, 15]. Such a coupling permits to study the interaction between changes in the 3D domain and the rest of the circulation (see examples in section 3.1).

3.3 Analysis and handling of numerical instabilities

3.3.1 Possible origins for boundary instabilities

The occurrence of backflow divergence is a well-known but not sufficiently addressed problem in the field of cardiovascular or respiratory flow simulation. This problem usually arises in large tubes (blood vessels or airways) that are exposed to backflow in 3D and 2D flow simulations. There are three main situations that lead to numerical divergence caused by backflow. First, backflow divergence can result from bulk reversal of the flow through an inlet or an outlet, such that there is negative flow over the entire face. Second, there may be localized areas of flow reversal on a face with bulk outward positive flow. And third, the use of multidomain modeling (see section 3.2) may necessitate the passing of pressure and flow information for which there is a lack of velocity profile information, leading to numerical instabilities on either the coupled inflow or outflow faces. All of these numerical instabilities emanate from the use of Neumann boundary conditions on the outlet faces, for which velocity profile information is not specified [Heywood et al., 1996, Formaggia et al., 2002a, Formaggia et al., 2008, Taylor et al., 1998b]. For the second case, seminal work on robust artificial boundary conditions in the presence of strong vortices can be found e.g. in [Bruneau and Fabrie, 1994, Bruneau and Fabrie, 1996]. In fact, this physiological backflow divergence has led the biofluid community to revisit these fundamental numerical analysis contributions on robust boundary conditions for Navier-Stokes incompressible equations [Begue et al., 1988, Sani et al., 2006].

Bulk backflow (complete flow reversal at an outlet) is a physiologic and commonly occurring phenomenon in the cardiovascular system in both healthy and diseased states. It often occurs in vessels during diastole and flow deceleration, particularly in certain regions. Thus, accurately capturing backflow phenomenon is essential for reproducing realistic conditions in many cardiovascular problems. Examples of physiologic flow reversal include flow in the descending abdominal aorta during diastole [11], flow reversal in the brachiocephalic artery after the stage 1 repair for single-ventricle heart patients (BT-shunt surgery) [42] and reversed flow due to respiratory effects in Fontan patients [14]. In airflow, it occurs even more strongly, since flow necessarily reverses between inspiration and expiration. Inertial effects can even be exacerbated with mechanical ventilation [15, 18].

Backflow divergence due to local flow separation or flow recirculation is commonly caused by complex geometries such as the presence of stenoses, anastomoses, or increased cross sectional area, near the outlets of a model. These geometric features often lead to either steady or unsteady separation regions close to the outflow faces of a model, particularly at peak systolic flow. Similarly, geometric features can also lead to vortex shedding, and convection of vortices through the outflow faces, also leading to backflow divergence (see example in 3.3.3).

Multidomain modeling, in which a closed-loop 0D parameter network of ODEs is coupled to the inflow and outflow faces, usually requires 'Neumann' boundary conditions on both inflows and outflows (section 3.2). In these situations, it is common that flow reversal is dictated by the pressure passed to the 3D model, causing a bulk inward flow without prescribing velocity profile information. In these situations, instabilities can occur, particularly in cases

with rapidly changing dynamics that may alternate between positive and negative flow within a cardiac cycle.

Simulation divergence due to the above causes, requires careful consideration of the outflow boundary conditions. Use of a mixed boundary condition, while successful in air convection simulations [Tezduyar et al., 2008, Tezduyar et al., 2010], in which a Dirichlet boundary condition is used for the normal component of the velocity (either on the entire outlet or only in the region with backflow) along with a Neumann boundary condition for tangential velocity components, requires extra information about the velocity profile and the flow rate magnitude, which is generally unknown for the outlets.

The simplest solution to the backflow issue is to artificially elongate the outlets by adding long straight sections, thereby dissipating the vortices before they reach the outlet. While this has been commonly used in simulations [de Zelicourt et al., 2009, Marsden et al., 2008, Borazjani et al., 2010], this method poses several major problems. First, for the case of total flow reversal at the outlet, the instabilities occur at the boundary so there is no reason this solution should work. Second, the addition of artificial extensions to the outlets has potential to change local hemodynamics, particularly in patient specific models or in multiscale modeling networks, where information at the boundary faces is coupled to another system. And third, there is a non-negligible additional computational cost incurred by the need to mesh and simulate long outlet extensions. This added cost increases for high Reynolds number flows, since longer extensions will be needed to dissipate the vortices. Another option is to add additional vessels to the model until the flow becomes unidirectional and the Reynolds number at the outlet is reduced [10]. While this method has proven to be effective in patient-specific cases, it can only be used in a non-artificial way if the image resolution is adequate enough to permit inclusion of additional levels of branching. Additionally, this method increases the model generation and computational costs significantly. Due to these issues, we will not consider outlet extensions or additional branches as viable methods in the current work.

In the next section, the numerical exploration of outflow boundary treatments in different test cases with zero and non-zero traction boundary conditions, shows the inertial boundary stabilization as the most robust remedy [34]. This has set the stage for improved stability in coupled multidomain systems in succeeding works [42, 33, 15, 18]. In section 3.3.3, a new approach is devised for such coupling [16]. A more thorough numerical analysis of different natural boundary conditions is carried out, illustrated by typical cardiovascular cases in patient-specific geometries.

3.3.2 Comparison of numerical instability treatments

Simulation divergence due to backflow is a common, but at the time of [34], not fully addressed problem in three-dimensional simulations of blood flow in the large vessels. Because backflow is a naturally occurring physiologic phenomenon, careful treatment is necessary to realistically model backflow without artificially altering the local flow dynamics. In this study, we quantitatively compare three available methods for treatment of outlets to prevent backflow divergence in finite element Navier-Stokes solvers. The methods examined are:

1. Adding a convective stabilization term to the boundary nodes formulation (see [34] and section 3.3.3 for its efficiency origin and formulation)

2. Constraining the velocity to be normal to the outlet (see [34] for exact implementation)

3. Using Lagrange multipliers to constrain the velocity profile at all or some of the outlets (see [34] for exact implementation)

Three model problems, a short and long cylinder with an expansion, a right-angle bend, and a patient-specific aorta model, are used to evaluate and quantitatively compare these

methods. Detailed comparisons are made to evaluate robustness, stability characteristics, impact on local and global flow physics, computational cost, implementation effort, and ease-of-use. We only provide one illustrative example in the following figure; for all the other results see [34].

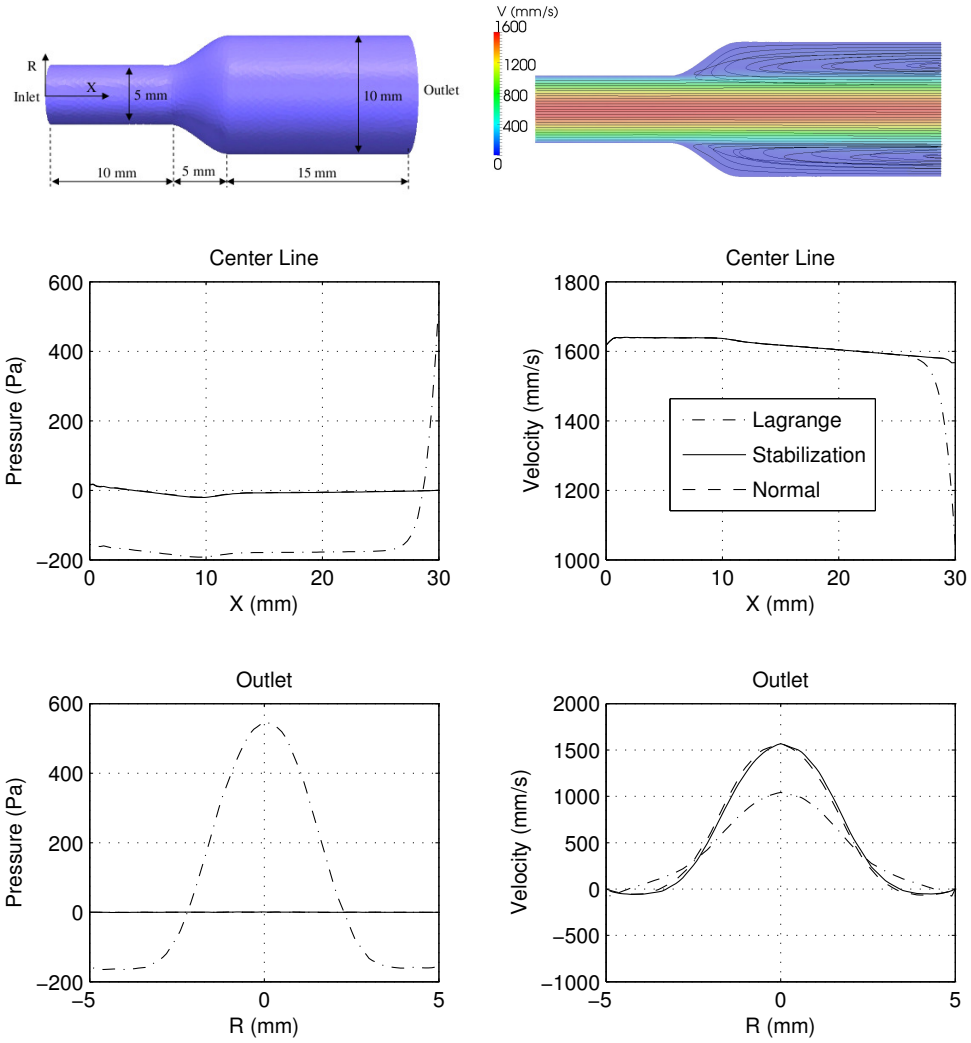

Figure 3.4: Geometrical model (upper left) and longitudinal cut showing streamlines color coded by velocity magnitude (upper right). Velocity and pressure on the centerline and at outlet section, at Re = 1000. Steady inflow and zero traction outflow boundary condition were imposed.

This simulation is done with a cylinder with expansion with an inlet Reynolds number of 1000 and a zero traction boundary condition. Contrary to a more elongated expansion, here without treatment, the simulation diverges. In fig. 3.4 we observe that the stabilization and normal constraint method results are very close. For the Lagrange multiplier method, although it does not change the velocity in the region far from the outlet, the velocity profile is changed significantly at the outlet. This induces changes in the outlet pressure as well. The reduction of velocity at the center and its increase in the peripheral region requires higher and lower pressure in those areas, respectively, to satisfy the momentum equations. This change in pressure is propagated throughout the model. The behavior on an elongated model is similar, failing to match the stable no-treatment solution contrary to the other methods.

Using identical numerics, models, and meshes, we have compared the methods of outlet stabilization, normal velocity constraint, and Lagrange profile constraints [34]. We show that the normal constraint can be safely used in the case of slight flow reversal, producing a stable result with little impact on the flow physics. However, this requires the constrained direction vector to be close to the direction of reversed flow and that only the part of the outlet with flow reversal be constrained. Our results show that the Lagrange method, while often successful in stabilizing the solution, suffers from high impact on the pressure field solution, high computational cost, and increased difficulty in both implementation and ease-of-use. While results with highly tuned outlet flows matched very well with the stabilized method results, a lack of tuning can produce drastically different results that are not confined to the vicinity of the outlet. The stabilization method is shown to have the highest robustness, and the least impact on the flow field, with no extra computational cost, and high ease of implementation and use. In addition, the stability of this method is improved to include a wider range of time steps by adding only a fraction of the convection term in our formulation. This implementation also reduces the impact of this method on the pressure field. To summarize, the addition of an outlet stabilization term provides an accurate, robust, and easy-to-use method that reliably prevents backflow divergence in numerical simulations of blood flow.

Recall that the stabilization only acts when velocity vectors point inwards at the coupling interface. It was introduced in [Bazilevs et al., 2009b] for cardiovascular applications with an energetically over-stabilizing effect as discussed in the next section 3.3.3, and successfully tested with a smaller energy-dissipative coefficient (a value of θ of 0.5 or less was found enough to ensure stability) in [34, 33, 15] in cardiovascular and respiratory contexts. In these papers, without this stabilization the simulations would have diverged. Next the version that exactly annihilates the energetically destabilizing convective term is considered. It leads in fact to a similar stabilizing behavior. The results highlight the robustness of this method under different conditions of complex and back flows. However such a coupling involves enforcing an ad-hoc inhomogeneous normal stress over the interface area and in practice generally induces an over-killing of the inward velocity vectors. Besides, as noted by [Porpora et al., 2012], this leads to a weak formulation that is not consistent with the original strong boundary condition of the reduced model coupling. A consistent formulation (with a value of θ of one) has been proposed by [Gravemeier et al., 2012] in respiratory mechanics (see this reference for earlier references about imposition of total momentum flux) but it requires to also prescribe the convective term and thus to know the velocity vectors at the coupling boundary or to make some further assumption on the velocity profile at the boundary [Gravemeier et al., 2012, Ismail et al., 2014]. It is interesting to note that in respiratory applications for which the back flow is very significant (whole expiration phase), the necessity to stabilize the convective term one way or another has been found crucial [Kuprat et al., 2013, Ismail et al., 2014] [15].

It is not a priori possible to predict which simulation will be stable throughout or diverge. Since divergence is typically observed with some inward and non-zero tangential velocity vector or complete back flow at the coupling interface, natural ideas are to enforce the tangential component to be zero or to even constrain the whole velocity profile. As these have been shown in this section to be non-ideal, in the next section only the convective stabilization method is retained among the three remedies to instability.

3.3.3 A novel method: a modified Navier-Stokes equation

When coupling a 3D domain with a 0D model, pressure is usually imposed as a uniform boundary condition on the 3D boundary. A first coupling method consists of enforcing a uniform pressure obtained from the reduced model at the coupling boundary. Without loss of generality, the reduced-order model providing the pressure p_c here, is assumed to result from

a standard RCR Windkessel model (see section 2.1.3) as sketched in fig. 2.1 (top):

$$C\frac{dp_p}{dt} + \frac{p_p - p_v}{R_d} = q \tag{3.2}$$

$$p_c - p_p = R_p q \tag{3.3}$$

where $q = \int_{\Gamma_{\text{out}}} \boldsymbol{u}\cdot\boldsymbol{n}$. For the sake of simplicity, we assume $p_d = 0$.

Multiplying (3.3) by q and (3.2) by p_p leads to the energy equation of the 0D model:

$$p_c q = C\frac{d}{dt}\left(\frac{p_p^2}{2}\right) + R_p q^2 + \frac{p_p^2}{R_d} \tag{3.4}$$

When a variational formulation is used, e.g. with the finite element method, it is more natural to replace the pressure with the normal component of the normal stress:

$$\boldsymbol{\sigma}\cdot\boldsymbol{n} = -p_{\text{c}}\boldsymbol{n}, \quad \text{on } \Gamma_{\text{out}}, \tag{3.5}$$

But stability analysis shows that the convective term on the boundary can be responsible for numerical instabilities in the presence of reverse flow:

$$\frac{d}{dt}E_{K_{\Omega_1}} + P_{V_{\Omega_1}} = P_{\text{in}} - \int_{\Gamma_{\text{out}}} p_{\text{c}}\boldsymbol{n}\cdot\boldsymbol{u} - \rho\int_{\Gamma_{\text{out}}}\frac{|\boldsymbol{u}|^2}{2}\boldsymbol{n}\cdot\boldsymbol{u}$$

Indeed in the presence of reverse flow at an outlet ($\boldsymbol{u}\cdot\boldsymbol{n} < 0$) the last term may thus have a destabilizing effect - denoting the kinetic energy, the viscous power and the energy entering the domain through Γ_{in}, respectively by:

$$E_{K_{\Omega_1}} = \int_{\Omega_1}\frac{\rho}{2}|\boldsymbol{u}|^2, P_{V_{\Omega_1}} = 2\mu\int_{\Omega_1}\varepsilon(\boldsymbol{u}):\varepsilon(\boldsymbol{u}), P_{\text{in}} = \int_{\Gamma_{\text{in}}}\boldsymbol{\sigma}\cdot\boldsymbol{n}\cdot\boldsymbol{u} - \rho\int_{\Gamma_{\text{in}}}\frac{|\boldsymbol{u}|^2}{2}\boldsymbol{n}\cdot\boldsymbol{u}. \tag{3.6}$$

Some Navier-Stokes formulations involve the total pressure in their natural boundary conditions (e.g. [Begue et al., 1988]):

$$\boldsymbol{\sigma}\cdot\boldsymbol{n} - \frac{\rho}{2}|\boldsymbol{u}|^2\boldsymbol{n} = -p_{\text{c}}\boldsymbol{n}, \quad \text{on } \Gamma_{\text{out}}. \tag{3.7}$$

This **3D-0D-Ptot** formulation has been shown to lead to an energetically stable coupling between 3D and reduced models of blood flow (e.g. [Formaggia et al., 2007, Formaggia et al., 2013]), since the potentially destabilizing term of (3.6) disappears in the energy balance:

$$\frac{d}{dt}E_{K_{\Omega_1}} + P_{V_{\Omega_1}} + C\frac{d}{dt}\frac{p_p^2}{2} + \frac{p_p^2}{R_d} + R_p\boldsymbol{q}^2 = P_{\text{in}} \tag{3.8}$$

Some of these authors have been expecting instabilities when the total pressure is not included in the transmission conditions but have not seen them numerically [Formaggia et al., 2013, Blanco et al., 2013]. In formulations based on static pressure, a dissipative stabilization (**3D-0D-Stab** coupling) has been proposed to counteract the destabilizing effect of the convective boundary term (see [Bazilevs et al., 2009b]), here written in a slightly more general form:

$$\boldsymbol{\sigma}\cdot\boldsymbol{n} = -p_c\boldsymbol{n} - \rho\theta(\boldsymbol{u}\cdot\boldsymbol{n})_-\boldsymbol{u}, \quad \text{on } \Gamma_{\text{out}}, \tag{3.9}$$

where $(\boldsymbol{u}\cdot\boldsymbol{n})_-$ is equal to $-(\boldsymbol{u}\cdot\boldsymbol{n})$ if $\boldsymbol{u}\cdot\boldsymbol{n} \le 0$, and is equal to 0 if not, and where θ has to be fixed. The energy balance thus reads:

$$\begin{aligned}&\frac{d}{dt}E_{K_{\Omega_1}} + P_{V_{\Omega_1}} + C\frac{d}{dt}\frac{p_p^2}{2} + \frac{p_p^2}{R_d} + R_p q^2 = \\ &\begin{cases} P_{\text{in}} - \frac{\rho}{2}\int_{\Gamma_{\text{out}}}|\boldsymbol{u}|^2(\boldsymbol{u}\cdot\boldsymbol{n}), \text{ if } \boldsymbol{u}\cdot\boldsymbol{n}\ge 0 \\ P_{\text{in}} - \rho(\frac{1}{2}-\theta)\int_{\Gamma_{\text{out}}}|\boldsymbol{u}|^2(\boldsymbol{u}\cdot\boldsymbol{n}), \text{ if } \boldsymbol{u}\cdot\boldsymbol{n} < 0 \end{cases}\end{aligned} \tag{3.10}$$

This formulation is therefore stable in the energy norm for $\theta \geq 0.5$. If $\theta = 0.5$, as in [34] [Porpora et al., 2012], the potentially destabilizing term of (3.6) is exactly balanced by the artificial dissipation when $\boldsymbol{u} \cdot \boldsymbol{n} < 0$. In some publications, a stronger dissipation is chosen (e.g. $\theta = 1$ in [Bazilevs et al., 2009b]). We also refer to [Bruneau and Fabrie, 1994, Bruneau and Fabrie, 1996] where similar ideas were introduced in a more general class of boundary conditions, revisited here in the context of physiological fluid dynamics. A boundary condition based on enforcing the continuity of pressure on the one hand and of a linear combination of flow and energy fluxes on the other hand, has been proven to be energetically stable, but it does not necessarily conserve mass [Dobroserdova and Olshanskii, 2013]. More recently, a local regularization of the fluid velocity along the tangential directions has been developed in [Bertoglio and Caiazzo, 2014]. In all these methods, the reduced model pressure is imposed as a uniform boundary condition for the Navier-Stokes equations. Note that this is not inherent to these methods, but more to the lack of knowledge of what else to prescribe. In fact in complex flow, such as when flow reverses, there is *a priori* no reason that the normal traction or the total pressure is uniform on a coupling boundary. For stabilized methods, the added term introduces some non-uniformity that has also no obvious reason to correspond to the physiological flow at hand.

In [16], we propose a new method to handle the outflow boundary conditions, by coupling the 3D Navier-Stokes equations with another 3D compartment. It consists of coupling system (2.1)-(2.4) to a modified Navier-Stokes system. Instead of a 0D model, an artificial 3D domain Ω_2 is added to the 3D domain of interest Ω_1 (bottom of fig. 2.1). In Ω_2, the Navier-Stokes equations are modified by adding terms to recover an energy balance similar to the one obtained with the **3D-0D-Ptot** formulation. The resulting system can be written in a compact form in $\Omega_1 \cup \Omega_2$:

$$\rho\frac{\partial \boldsymbol{u}}{\partial t} + \rho\boldsymbol{u}\cdot\nabla\boldsymbol{u} + \nabla p - 2\mu\nabla\cdot\boldsymbol{\varepsilon}(\boldsymbol{u}) + \gamma\boldsymbol{u} + \rho\frac{\boldsymbol{u}}{2}\nabla\cdot\boldsymbol{u} = 0 \tag{3.11}$$

$$\alpha\frac{\partial p}{\partial t} + \beta p + \nabla\cdot\boldsymbol{u} = 0 \tag{3.12}$$

$$\boldsymbol{u}_{|\Gamma\cup\Gamma_2} = 0 \tag{3.13}$$

where α, β and γ vanish in Ω_1, to recover the standard equations (2.1)-(2.4), and are positive in Ω_2. Parameter α is a distributed version of the capacitance (C) in the Windkessel model. Parameters γ and $1/\beta$ play the role of the proximal (R_p) and distal (R_d) resistances respectively. The additional term $\rho\frac{\boldsymbol{u}}{2}\nabla\cdot\boldsymbol{u}$ is necessary to ensure stability in the energy norm, because the fluid is no longer incompressible in the artificial domain Ω_2. The equations in the two domains Ω_1 and Ω_2 are coupled through the usual transmission conditions:

$$\boldsymbol{u}_1 = \boldsymbol{u}_2, \text{ and } \boldsymbol{\sigma}_1\cdot\boldsymbol{n} = \boldsymbol{\sigma}_2\cdot\boldsymbol{n}, \quad \text{on } \Sigma, \tag{3.14}$$

which are automatically satisfied when a standard variational formulation of equations (3.11)-(3.13) is set on the whole domain $\Omega_1 \cup \Omega_2$. Due to these transmission conditions (3.14), the energy balance of this modified Navier-Stokes formulation **3D-3D** is obtained:

$$\frac{d}{dt}E_K^{\Omega_1\cup\Omega_2} + P_V^{\Omega_1\cup\Omega_2} + \alpha\frac{d}{dt}\int_{\Omega_2}\frac{p^2}{2} + \beta\int_{\Omega_2}p^2 + \gamma\int_{\Omega_2}|\boldsymbol{u}|^2 = P_{\text{in}}^{\Omega_1}. \tag{3.15}$$

This formulation is therefore stable in the energy norm. Contrary to **3D-0D** coupling, an inequality can be proved to control the energy of the system. Compared to the **3D-0D-Stab** formulation, it can let energy enter into the system through Γ_{out} in the presence of a physical backflow. Compared to the **3D-0D-Ptot** formulation, it is not based on the total pressure, and is thus expected to avoid the associated spurious velocity behavior. Comparing (3.15) with (3.8), we notice an analogy between α, β, γ and the standard Windkessel parameters.

From this observation, we can set $\alpha \approx C/V$, $\beta = 1/(R_d V)$, and $\gamma \approx R_p S/L$, where V, S and L respectively denote the volume, the section and the length of the artificial domain Ω_2.

For the weak formulations of the different formulations and their numerical discretization, we refer to [16].

We present the results obtained on a child patient-specific pulmonary arteries with congenital heart disease. Figure 3.5 represents the complete geometrical model, that is used for the reference solution, a short geometrical model with cut pulmonary artery branches, that is used for **3D-0D** , **3D-0D-Ptot** and **3D-0D-Stab** methods, and a short model with its artificial parts at the outlet surfaces, that is used for **3D-3D** and a hybrid between **3D-3D** and **3D-0D** noted **3D-3D-0D**. The velocity is prescribed at the inlet with a plug profile, following a typical shunt flow tracing. The highest Reynolds number is 3000.

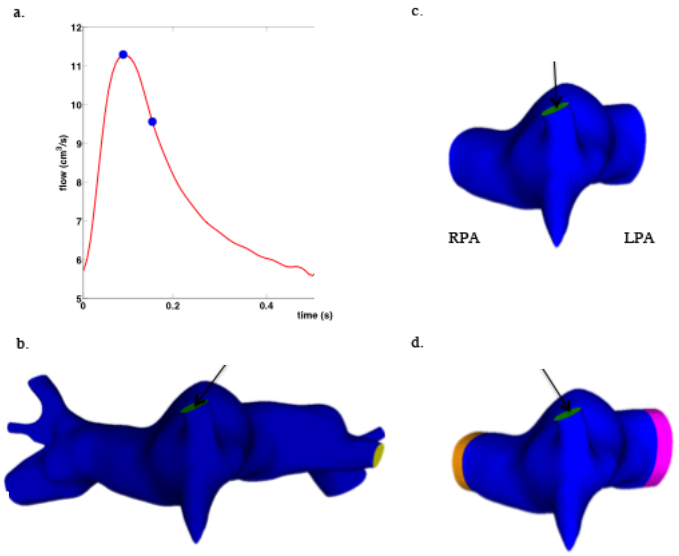

Figure 3.5: a. Imposed inlet flow, with the two dots representing maximum flow and decelerating flow respectively; b. Complete model (for reference solution); c. Short model (two outlets, RPA and LPA), and d. Short model with one modified Navier-Stokes part on each side. Arrows indicate the inlet.

In fig. 3.6 velocity fields in the RPA are compared between the different methods at the same location during maximal forward flow (left) and deceleration flow (right). The **reference** case was run with a **3D-0D** method. It presents no instability because the flow is smoother at its distal outlets, which is typical of bifurcations quite downstream of complex flow [23]. The other three methods were run in the cut model. At maximal forward flow, the **reference** model shows complex flow in the RPA. This behavior is retrieved with the **3D-0D** coupling method but with inwards velocity vectors. However, the computation is close to divergence. The **3D-0D-Stab** coupling method efficiently kills the reverse velocity vectors at the coupling surface so that a similar forward flow motion to the **3D-0D** coupling method is retrieved without backflow, and similarly for the **3D-3D-0D** result. Note that the **3D-3D** coupling leads to a velocity profile closer to the reference case.

Regarding blood flow behavior during the decelerating phase in fig. 3.6 (right column), there is reverse flow in **reference** case and a large proportion of the forward flow is located at the bottom of the surface area. With the **3D-0D** coupling method at outlet surfaces of the cut model, the computation is diverging, but the **3D-0D-Stab** coupling method leads to a blood flow behavior where velocity vectors are underestimated at the center and top of the coupling surface area. In the **3D-3D** coupling approach, flow motion is more homogeneous in terms of size and direction of the velocity vectors. For the **3D-3D-0D** coupling, the majority of flow is located at the bottom of the coupling surface and backflow is authorized in the upper part. The obtained flow behavior is thus close to the **reference** case.

In fig. 3.7 the velocity field for the **3D-0D-Ptot** coupling method behaves as in the previous patient-specific case of adult pulmonary arteries. Moreover, the computation is diverging.

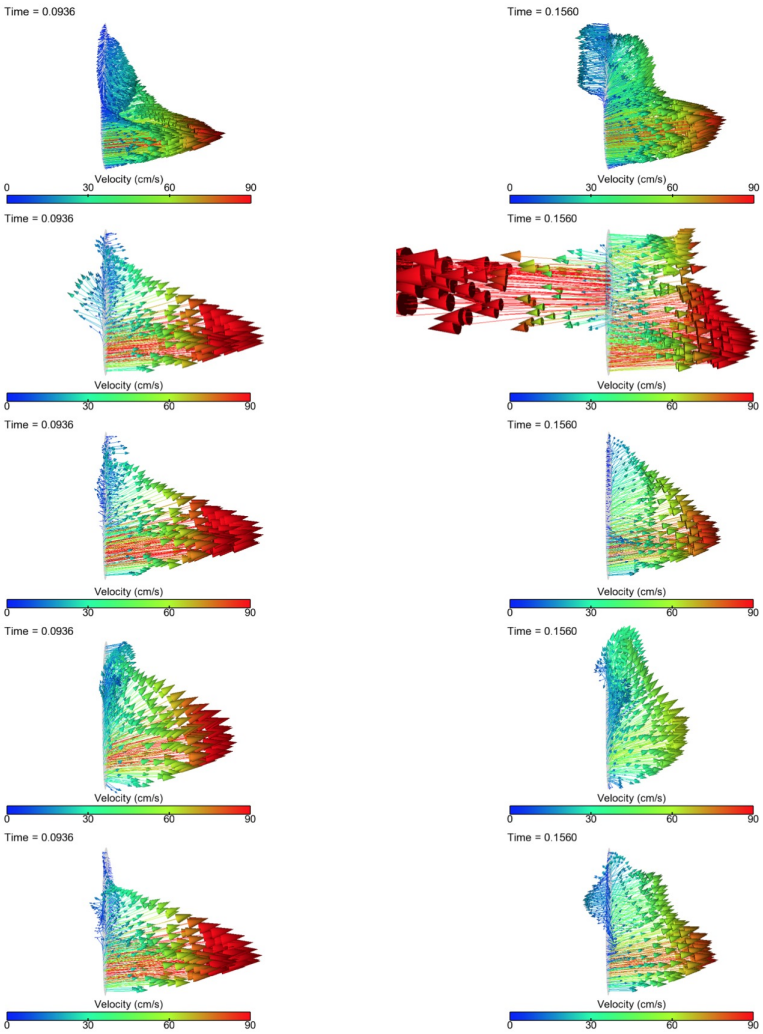

Figure 3.6: Velocity fields in RPA at peak inlet flow (left) and during decelerating flow (right) comparing the reference solution (**3D-0D** on the complete geometry), **3D-0D** and **3D-0D-Stab** (on the cut geometry), **3D-3D** and **3D-3D-0D** (on the extended cut geometry) coupling methods from top to bottom.

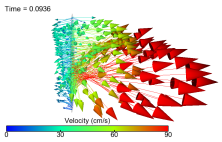

Figure 3.7: The RPA velocity field during peak flow with the **3D-0D-Ptot** coupling method.

These results are representative of the different test cases we ran, with inflow back flow or more extensive deceleration such as what is happening in the aorta [16]. For an in depth discussion about the results in the context of the existing literature, we also refer to [16].

In conclusion, our contributions with respect to the existing works considering a 3D compartment (e.g. [Maury et al., 2005]) are the following. First, our artificial compartment is more complex since it includes two different kinds of dissipation and one term representing an elastic potential energy. This allows us to mimic an RCR Windkessel model, which is important in our applications. Second, we have investigated how this artificial compartment affects outflow instabilities typically encountered in hemodynamics; third, we made a numerical comparison of different outflow boundary conditions in realistic hemodynamics test cases. The advantages of such an approach are that the coupling 1) does not enforce a uniform traction at the interface, 2) is energetically close to the usual 3D Navier-Stokes - Windkessel solution, without the potentially destabilizing convective boundary term (or, in the hybrid variant, stable in numerical practice), 3) is provably stable in the energy norm without needing a total pressure formulation, 4) the strategy of adding an artificial 3D part can be very useful in a commercial code that does not allow the users to implement any 0D boundary conditions.

Qualitative and quantitative comparisons of existing coupling methods of three-dimensional Navier-Stokes equations to 0D reduced models with this modified Navier-Stokes approach have been made in three patient-specific cases of healthy adult and diseased child pulmonary arteries and healthy adult descending aorta (all of them can be found in [16]). The **3D-0D** and **3D-0D-Ptot** methods are sensitive to instabilities, depending on where the 3D domain is artificially cut, while the other methods remain stable in all tests. Results from earlier coupling methods match those from the literature. Numerical results from the modified Navier-Stokes approach are especially less invasive during deceleration or reverse flow. The hybrid form of this new method, the **3D-3D-0D** method, is particularly promising as it effectively stabilizes the simulations, without significantly affecting forward flow but allowing more freely inward velocity vectors than the **3D-0D-Stab** method. The comparison of the cut-models with the reference, more extended model highlights the importance of including enough downstream geometry to not affect hemodynamics in the area of interest of the three-dimensional part in biomedical applications.

The dynamics accuracy of the proposed method can be increased by better tuning parameters to match clinical data. This method could also be improved with a space-varying dissipative term. Finally, this method can be extended to other biological patient-specific simulations, like more extensive hemodynamics reduced models or air flow into the lungs.

4

Data-driven model parametrization

Multidomain modeling (section 3.1) is more and more common to assess in detailed flow in a 3D region of interest (section 2.1.1), while the rest of the blood circulation or respiratory system is taken into account with reduced models (for 0D see section 2.1.3, for 1D see section 2.1.2). The latter constitute boundary conditions for the 3D part, and drive most of its dynamics. They are thus crucial for the model. Yet, their parameters are *a priori* unknown: they need to be identified in order to reflect blood or air flow measurements. Depending on the considered application, available measurements besides imaging data to build the 3D geometry vary. Here, direct or surrogate measurements of flow and/or pressure are considered. Depending on the acquisition method, either full time-varying curves or only mean values are trusted. We thus present several challenges in this topic:

1. Measurements are not necessarily taken at boundaries of the 3D domain.
2. They are often too few to identify all parameters, and thus need to be complemented by modeling assumptions or literature data.
3. They are usually not taken simultaneously and are thus not synchronized in time.
4. Computational complexity is often an issue for parameter identification.

Each section is addressing these challenges in its own way. The question of identifiability is not addressed here in the formal mathematical sense (see e.g. [Boulakia et al., 2013] for Robin parameter estimation in the Stokes system), but rather a practical approach is proposed: either the model is chosen simple enough to ensure identifiability (section 4.1) or sensitivity analysis tools give a numerical feedback (section 4.3).

Strategies should be devised according to the available measurements: their implementation and computational complexity need to be coherent with the amount of information. Thus parameter identification can be done on purely 0D models (sections 4.1 & 4.3), on loosely coupled 3D-0D models (section 4.3), or on strongly-coupled 3D-0D models (in the sense that each parameter identification simulation includes the 3D part) (section 4.2). In terms of methods, variational approaches (simple parameter space search in section 4.1, fixed-point algorithm in section 4.2) and sequential (unscented Kalman filter) approaches in section 4.3 have been implemented. Applications are presented through several real clinical and experimental cases. They include construction of typical patient setting for device design, preoperative patient state modeling for virtual surgery (section 4.2), cardiovascular disease assessment (section 4.3) and respiratory disease assessment (section 4.1).

Remark 1 *Note that in multiscale models of tissues such as in multicellular spheroids (section 2.3), the model is more complex compared to blood and airflow cases. Due to the interactions of agent-based (cellular automaton) cell models with continuum molecular scale models, and their stochastic nature, the above parametrization strategies do not work. Besides, the data available are of 2 kinds: 1) partial solution snapshots – spatial labeling by immunochemistry of proliferating cells, dying cells, etc. on spheroids cuts at several days–, 2) overall growth dynamics surrogate (projected spheroid area over time). In such a case, time-consuming manual tuning of the parameters, within the acceptable physiological ranges, has permitted to infer some mechanisms that explain the diversity of data for different nutrient concentrations (fig. 2.11). This will not be presented here, but all details can be found in [31].*

4.1 Simplest model when data is scarce: application to better understanding of emphysema

4.1.1 Parameter estimation for homogeneous emphysema

Simulations of airflow in the lung (fig. 1.3) can augment experimental knowledge and physiologic understanding only if they can accurately model *in vivo* respiratory conditions and

anatomy. Due to the vast range of length scales in the lung, complex geometry, computational cost and complex pulmonary tissue mechanics, it is currently impossible to model the lung in full. Therefore, multidomain methods must be employed that couple here 3D geometry of the largest airways (section 2.1.1) to lower-dimensional models of the rest of the respiratory system (section 2.1.3) as in section 3.1.

Deposition in emphysematous lungs (see section 1.2.2) has been previously studied in vivo [Brand et al., 2009, Sweeney et al., 1987], in vitro [Oakes et al., 2010], and with empirical models [Sturm and Hofmann, 2004, Segal et al., 2002], however with conflicting results regarding particle deposition in emphysema. This work thus provides a mathematical modeling framework to study how ventilation and particle transport differ in emphysema.

While prior numerical studies have investigated airflow [Gemci et al., 2008, Monjezi et al., 2012, Baffico et al., 2010], particle deposition [Comer et al., 2000, Longest and Vinchurkar, 2007, Nowak et al., 2003, Walters and Luke, 2011] and distribution [Darquenne et al., 2011] in the lung, few have incorporated patient or animal specific geometry and breathing parameters. Airflow [De Backer et al., 2008, Minard et al., 2012, de Rochefort et al., 2007] and particle deposition [Fetita et al., 2005, Comerford et al., 2010, Nowak et al., 2003] in the lung were shown to be highly dependent on geometry and flow asymmetry [Butler and Tsuda, 2005]. Boundary conditions that describe the upstream and downstream mechanics outside of the 3D domain must be defined on the inlets and outlets for all CFD simulations. Constant pressure or flow rate are typically implemented at the mouth/trachea and distal airway outlets. However, as the flow patterns change in time, CFD simulations should model the breathing unsteadiness, to determine airflow [Malve et al., 2013] and particle [Comerford et al., 2010] deposition patterns in the lung. Thus, appropriate boundary conditions must be devised.

Multidomain modeling techniques have been applied to numerous studies in the cardiovascular system (see sections 3.1, 3.2, 4.2, 4.3). However, not until recently have these methods been applied to the respiratory system [Kuprat et al., 2013, Gravemeier et al., 2012, Malve et al., 2013, Baffico et al., 2010]. These models enable more realistic 3D unsteady flow simulations because they do not require direct description of time-dependent flow and pressure waveforms at the distal branches, which are typically unknown [Gravemeier et al., 2012]. However none of these works directly parameterized their lower dimensional models from animal or patient in-vivo specific data. In addition, the recent work of [Wongviriyawong et al., 2013] showed that their lumped parameter model of the human lung could only reproduce the ventilation measurements if it included the downstream resistances and compliances tuned from healthy and asthmatic measurements. These findings help motivate the usage of such 0D parameter models components when solving for airflow in a 3D CFD model.

Despite their extensive use in toxicology [Wichers et al., 2006] and therapeutic studies [Agu and Ugwoke, 2011], relatively few studies have simulated airflow [Minard et al., 2012] and particle deposition in the rat lung. In a recent study, CFD and MRI steady flow measurements agreed well in the conducting airways [Minard et al., 2012]. Empirical models can be predictive of particle deposition in the rat [Anjilvel and Asgharian, 1995], however there have been no prior 3D simulations of particle transport and deposition in rat airways.

The goal of this work [15] is to develop a multidomain respiratory model to simulate airflow and particle deposition with the aim of replicating animal aerosol exposure experiments [Oakes et al., 2013] in both healthy and emphysematous rats [Oakes et al., 2014]. Note that the experiments were performed before the mathematical modeling.

Five healthy and five elastase induced emphysematous [Oakes et al., 2014] anesthetized rats were mechanically ventilated (fig. 4.1). During inhalation, the piston pump pushed 2.2 mL of particle-laden air into the lung at a breathing frequency (BF) of 80 $breaths \backslash min$. The

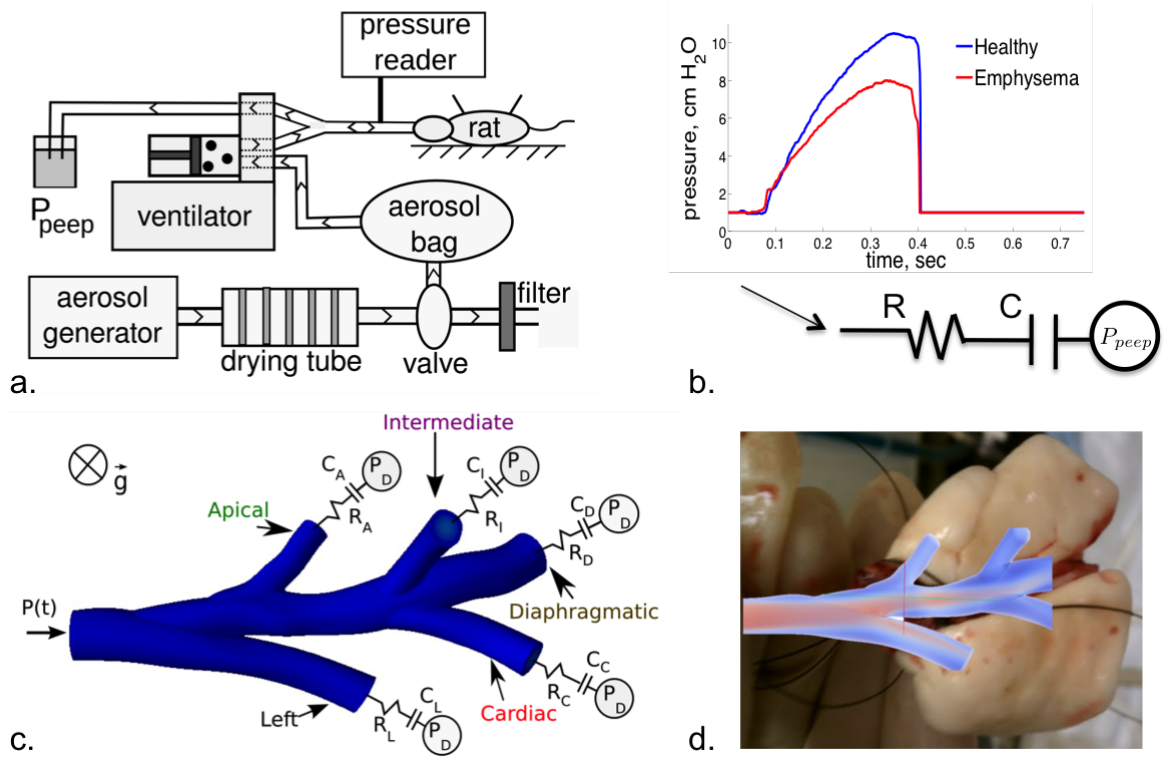

Figure 4.1: a) Rat aerosol exposure experiment. b) Reduced global model and driving measured pressure. c) 3D-0D model. d) 3D velocity field rendering (dark blue for low velocity to red for high velocity) superposed on the excised lung.

particles had a 0.95 μm geometric diameter and a density of 1.35 $g\backslash cm^3$ [Oakes et al., 2013]. At the end of inhalation, the rat passively exhaled through a tube subjecting the rat to a constant 1 cmH_2O end expiratory pressure (P_{Peep}). Pressure $P(t)$ was measured over time at the trachea and the maximum pressure was significantly lower (p = 0.01) in the emphysematous rats compared to the healthy rats [Oakes et al., 2014] (fig. 4.1b). The only other available respiratory measurement is the tidal volume pushed by the pump at the end of inspiration. Thus, in a first step we characterize the respiratory system by a well-known two-component R-C model (0D global model) (see section 2.1.3 and [Bates and Suki, 2008], [15] for its derivation):

$$R\frac{dV}{dt} + \frac{V(t)}{C} = P(t) - P_{peep}. \tag{4.1}$$

where $V : \mathbb{R}^+ \to \mathbb{R}$ is the instantaneous inhaled volume (deviation of the lung air volume from the minimum air volume at quiet breathing). As the rats were ventilated at a breathing frequency and tidal volume representative of normal breathing, it is appropriate to assume constant resistance and compliance [Diamond and O'Donnell, 1977]. As the R and C parameters are unknown, eqn. 4.1 is solved using a large range of values. A unique pair is found for each rat satisfying the following constraints from the experimental data: a) the maximum volume is the one imposed by the pump (i.e. 2.2 mL) and b) inspiration ends as set by the pump (i.e. time of maximum volume was $1\backslash(2BF)$). Resistance during exhalation is set to 1.5 times the resistance during inhalation following previous work [Rubini et al., 2011]. A Mann Whitney two-tailed t-test shows that capacitance, contrarily to resistance, is significantly higher (p = 0.04)) in the emphysematous rats (C=0.37±0.14$cm^3\backslash cmH_2O$) compared to the healthy rats (C=0.25±0.04$cm^3\backslash cmH_2O$). The increase is found consistent with the literature. The resulting breathing dynamics (fig. 4.2) shows how expiration is delayed in the emphysematous rat.

The multidomain airflow simulations are then performed by coupling MRI-derived 3D rat conducting airways [Oakes et al., 2012] to the 0D global model (fig. 4.1c). In this first study [15], only the first branch of each lobe is included. We refer to the paper for model parameters and numerical methods choices, including multi domain coupling (section 3.2.2), inertial stabilization (section 3.3) and anisotropic mesh adaptation ([Muller et al., 2005], section 2.1.1). To summarize, the 3D Navier-Stokes equations are solved with the following boundary conditions. The experimental pressure used to estimate the global parameters (fig. 4.2A) is applied at the trachea as a Neumann boundary condition. At the airway walls, the no-slip zero velocity boundary condition is set. At each distal face, the 3D Navier-Stokes equations are coupled to a 0D model as in eqn. 4.1. While a few recent studies have measured ventilation in rat lungs [Emami et al., 2011], none of these have measured the ventilation distribution to each lobe. However, Raabe et al. [Raabe et al., 1975] measured the lobar distribution of 0.52 μm particles in spontaneously breathing rat lungs and found the distribution of deposited particles to be proportional to lung volume. Particles of this size have minimal intrinsic properties and consequently they closely trace the convective flow in the lung. Therefore, for each lobe, the parameters $R_{distal,i}$ and $C_{distal,i}$ are computed assuming that the regional tidal volume to each lobe is proportional to its volume at total lung capacity, where α_i is the volume of each lobe divided by the total lung volume [Oakes et al., 2012]:

$$C_{distal,i} = \alpha_i C \ ; \ R_{distal,i} = \frac{R}{\alpha_i} \tag{4.2}$$

The global resistance is thus distributed among the resistances distal to the 3D domain, which is justified because the resistance in the 3D domain is negligible. One healthy and

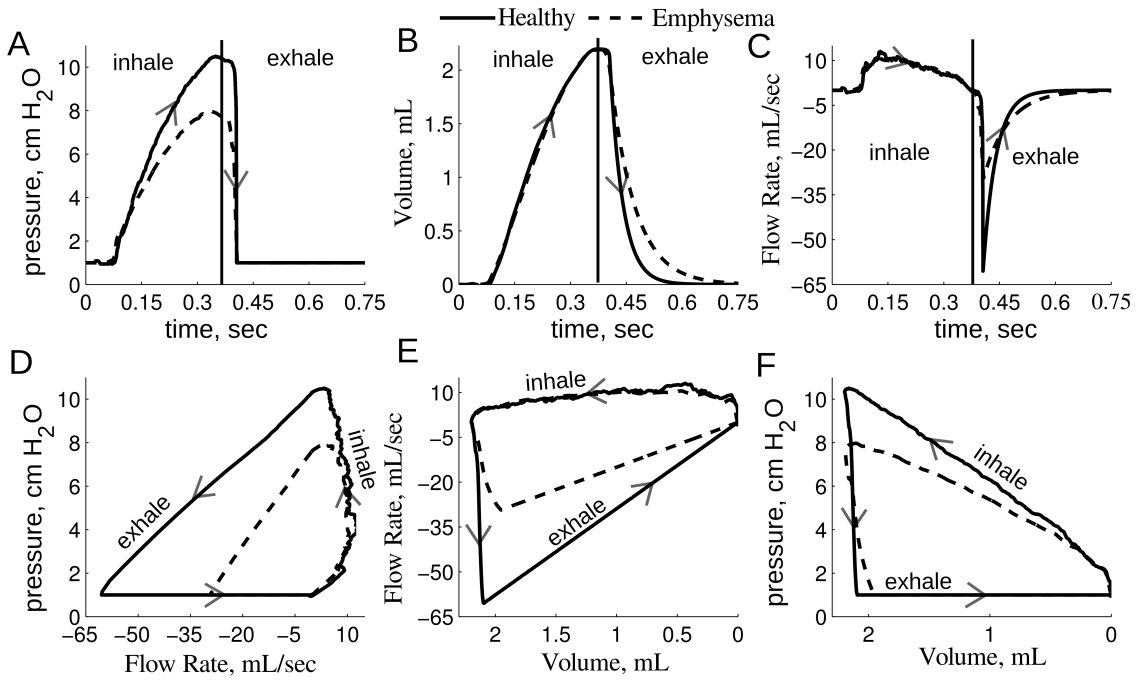

Figure 4.2: Global 0D model solution for healthy and emphysematous rats. A: experimental pressure used to solve eqn. 4.1 and applied to the trachea face for the 3D-0D simulations. B and C: the 0D volume and flow rate solution. D, E and F: pressure and flow rate loops, flow rate and volume loops and pressure volume loops. Arrows: direction of the breathing cycle.

one emphysematous representative rats are simulated. To compare this data-driven homogeneous emphysema case to heterogeneous emphysema, disease localized to one lobe only is also simulated for the five different lobes (see an illustrative example in fig. 4.3).

Finally, particles are tracked in the 3D domain during inspiration to determine deposition sites within the 3D model and delivery distribution of particles into the five rat lobes. Rigid spherical particles are tracked in the 3D model by solving the Maxey-Riley equation [Maxey and Riley, 1983]. For small particles the Faxen correction and Basset/Boussinesq memory terms may be neglected [Maxey and Riley, 1983]. Therefore, the Maxey-Riley equation reduces to

$$\left(\rho_p + \frac{\rho_f}{2}\right)\frac{d\mathbf{v}}{dt} = (\rho_p - \rho_f)\mathbf{g} + \frac{3}{2}\rho_f\frac{D\mathbf{u}}{Dt} - \frac{9}{2}\frac{\mu}{a^2}(\mathbf{v}-\mathbf{u})\ , \tag{4.3}$$

where $\mathbf{v} : \Omega \times \mathbb{R}^+ \to \mathbb{R}^3$ is the particle velocity, a is the particle radius, μ is the viscosity of air, ρ_p is the particle density, ρ_f is the fluid density, $\mathbf{u} : \Omega \times \mathbb{R}^+ \to \mathbb{R}^3$ is the air velocity. We refer to [15] for the model parameters and the numerical methods. Gravity, $\mathbf{g}$, is either positioned to represent a rat in the supine position as in the experiments [Oakes et al., 2013], or such that the rat was in the standing position.

Simulations are performed for a healthy rat lung, one with homogeneously distributed emphysema, and five different cases of heterogeneous emphysema (see [15] for illustration and discussion of the results). Furthermore, the influence of particle size and rat position are investigated. The regional tidal volume at each of the distal airways is found to match the expected flow distribution in these multidomain simulations, unlike when a constant pressure boundary condition is applied at the distal airway faces. The unsteady simulations exhibit complex flow patterns, especially at the triple bifurcation area. These complex flow patterns

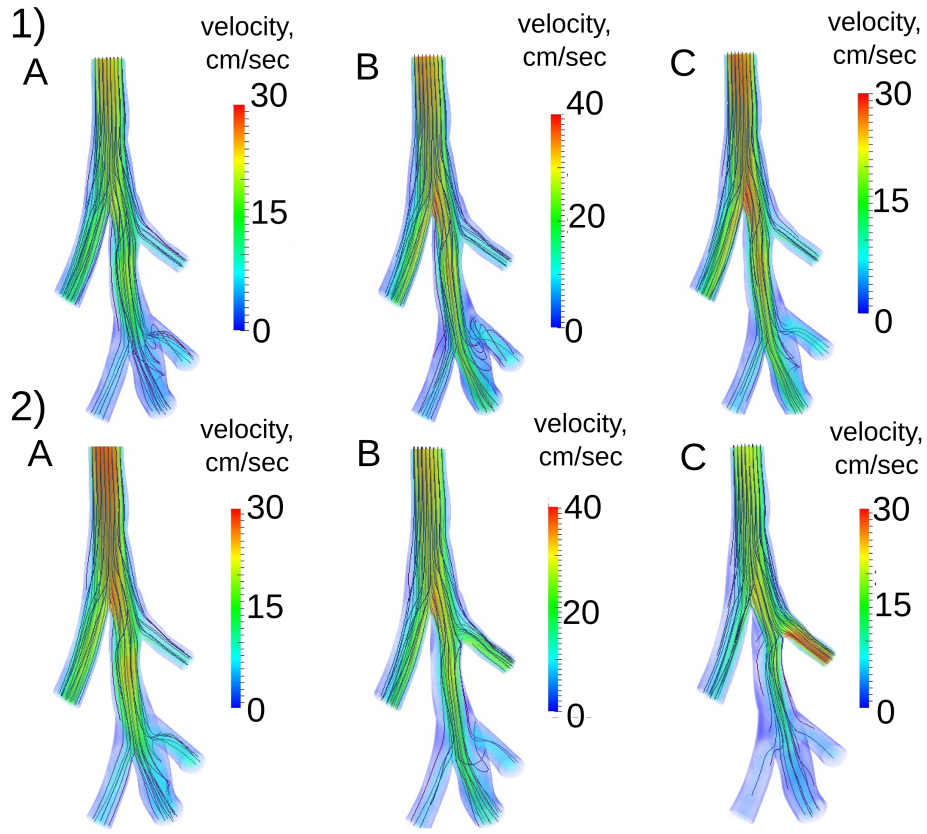

Figure 4.3: 3D rendering of the velocity magnitude and massless fluid particle pathlines for homogeneous emphysema (panels 1A-C) and for heterogeneous emphysema (apical lobe diseased) (panels 2A-C). Time points are mean inflow during acceleration, peak inflow, mean inflow during deceleration.

influence the particle deposition in the airways; fewer particles travel to the cardiac and intermediate lobes compared to their corresponding fraction of regional tidal volume. There is an increase in airflow, particle deposition in the 3D model, and particle delivery to the diseased regions for the heterogeneous cases compared to the homogeneous cases. Moreover, a standing rat position and a larger particle size both increase deposition in the 3D model. Finally, in some cases the particle deposition analytical models studied here predict a higher deposition compared to the 3D numerical simulations. This is likely because the analytical models do not account for the influence of unsteady flow and complex flow patterns.

In summary, this study presents a novel combination of a subject-specific multidomain airflow model and its parametrization directly from in-vivo experimental data. The airflow and particle deposition in the rat airways were solved under unsteady breathing conditions, and the CFD model was used to predict the influence of emphysema on deposition and distribution of particles in the conducting airways of the lung. The results highlight the importance of multidomain numerical simulations to study airflow and particle distribution in healthy and diseased lungs. The effect of particle size and gravity were studied. In a next step, these *in silico* predictions may be compared to experimental deposition data.

4.1.2 Parameter estimation for heterogeneous emphysema

When the experimental deposition data became available, we realized that emphysema was heterogeneously distributed within several lobes. Furthermore, we wanted to take into account all the airways visible given the MRI resolution. These two points led to a second work [18], summarized in this section.

Computational fluid and particle dynamics simulations provide detailed spatial and temporal distributions of airflow and particles in healthy and diseased lungs. However, to increase confidence in these models, results must be validated against *in vivo* experimental data. While several groups have shown good agreement between three-dimensional (3D) flow [de Rochefort et al., 2007, Mylavarapu et al., 2009] and particle-based [Longest et al., 2012, Ma and Lutchen, 2009, Ma et al., 2009, Zhang and Kleinstreuer, 2001, van Ertbruggen et al., 2009] models with *in vitro* experiments, these comparisons are not sufficient for validation of *in vivo* conditions. While 1D particle transport models have relatively well predicted *in vivo* data of total and regional deposition in the human [Darquenne and Paiva, 1994, Asgharian et al., 2006, Katz et al., 2013] and rat [Schmid et al., 2008, Anjilvel and Asgharian, 1995] lung, they do not provide detailed spatial information. Recently, Minard et al. [Minard et al., 2012] showed promising agreement between *in silico* predictions and *in vivo* magnetic resonance (MR) derived flow fields in rat lungs. While these previous studies have advanced the validity of computational models, none of them compared multidomain simulations to regional particle deposition data in both healthy and diseased lungs.

Emphysema has been shown to impact particle deposition in the lungs [Oakes et al., 2014, Sweeney et al., 1987, Brand et al., 2009]. To study the influence of emphysema-like morphometric changes on particle deposition, [Oakes et al., 2014] previously employed MR methods [Oakes et al., 2013] to determine lobar deposition in elastase-treated and healthy rat lungs. Results showed, for rats ventilated with the same breathing parameters, that particle concentration was higher in the elastase-treated lungs, compared to the healthy lungs. However, the distribution of particles to the lobes was the same in the healthy and emphysematous rats [Oakes et al., 2014] despite the MR and histological measurements suggesting heterogeneous distribution of emphysema-like structures in several lobes of the emphysematous group.

The goal of the current study is to extend the previous 3D geometric model (see previous section) and to compare regional deposition predictions to experimental data [Oakes et al., 2014]. These simulations require matching the numerical model as closely as possible to the experimental conditions and comparing the predicted distribution of inhaled

particles to the experimental lobar deposition. Using this *in silico* model, we explore the influence of flow conditions (unsteady versus steady) and initial particle spatial distribution on deposition and lobar delivery.

In terms of methods, the multidomain numerical framework is the same as in the above section (see also [18]), leading here to 3 million elements mesh even after adaptation. What changes is how the parameters of the 0D equation 4.4 in the 3D-0D simulations are inferred from data, especially for the emphysema case, which here is heterogeneous.

$$R_{i,j}\frac{dV(t)_{i,j}}{dt} + \frac{V(t)_{i,j}}{C_{i,j}} = P(t)_{i,j} - P_{peep}, \tag{4.4}$$

where $V_{i,j}$ is the inspired volume, $P(t)_{i,j}$ is the pressure at each distal face and the j and i indices identify the distal faces, with lobe j and assigned airway number i. In the next two paragraphs, the parameters $R_{i,j}$ and $C_{i,j}$ are estimated using a combination of the experimental measures and a purely 0D model (e.g. fig. 4.4 C). With this formulation, it is assumed and verified that the 3D resistance does not influence the average flow repartition in the distal branches of the 3D tree. Therefore, the driving pressures, $P_H(t)$ or $P_E(t)$ (fig. 4.4 A) remain the relevant $P(t)_{i,j}$ for these solely 0D models.

The 0D model parameters for the healthy simulations are defined as functions of both the fractional cross-sectional area within each lobe j and experimentally-measured lobar volume fraction α_j, and the global RC parameters identified in the previous section, in the spirit of eqn. 4.2. Neglecting the 3D region, all the distal RC 0D models in parallel are mathematically equivalent to a single global RC 0D model. This is due to the fact that the products $R_{i,j}C_{i,j}$ are all equal, i.e. the relaxation times are the same. As before, the 0D resistance during expiration is set to 1.5 times the 0D resistance during inhalation ($R_{i,j_{ex}} = 1.5R_{i,j}$) [Rubini et al., 2011]. Emphysematous regions are heterogeneously located in the lung to match the histological and MRI experimental findings [Oakes et al., 2014]. The lung is divided into normal (Zone 1) and diseased (Zone 2) regions (fig. 4.4B). Due to this heterogeneity, a new procedure to estimate the distal parameters is designed, based on a purely 0D model. In fact, several RC models in parallel are not mathematically equivalent to a single RC model when the characteristic times, that is, the products $\tau = RC$ are not the same. Within each homogeneous region (normal or diseased) these products are the same by construction. However between regions, this is no longer true, that is, a diseased RC and a normal RC in parallel are no longer formally equivalent to a global RC model. [Note that only the global compliance, and not the global resistance, changed for the emphysematous rats compared to the healthy rats (see previous section), resulting in different relaxation times between these two states.] As a result, the relationship between experimentally determined global R and C, and lobar or sublobar values is no longer simple. However, the latter can be determined with a 0D model, in which each homogeneous region (normal or diseased) is represented by a single RC model (fig. 4.4C). For details, see [18].

Following the airflow simulations, particle transport and deposition are simulated throughout inspiration as in the previous section, after having checked independence to the time step and number of particles released. The percentage of deposited particles is calculated by normalizing the number of particles deposited by the number of particles inspired. The particle delivery to each lobe P_{Del_j} is calculated as a % of the total delivery (wall deposited or exited particles). It is then normalized by the lobar volume fraction, giving VP_{Del_j}.

This study is the first to compare 3D numerical particle deposition simulations to experimental data in both healthy and diseased conditions. The main flow results are that contrarily to normal rats, there is an asynchrony between the healthy and diseased regions in emphysema, and as a consequence air is still entering certain zones while leaving others (fig.

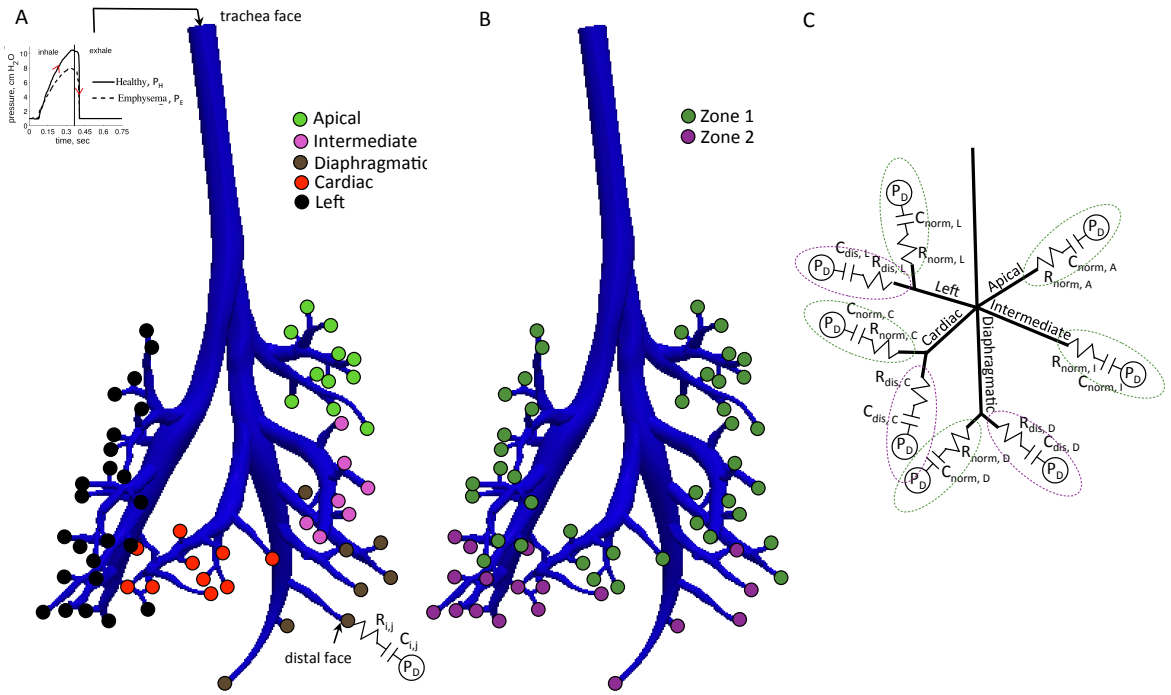

Figure 4.4: 3D airway geometry [Oakes et al., 2012] used for all the simulations. Panel A: identification of the airways leading to the five lobes. Panels B and C: definition of the zones for the emphysematous simulations. Zone 2 (diseased region) is set to be at the bottom $\frac{1}{3}$ of the left, cardiac and diaphragmatic lobes. Zone 1 (normal region) is defined as the top $\frac{2}{3}$ of the left, cardiac and diaphragmatic lobes and the entire apical and intermediate lobes. Panel C shows the distribution of the normal (R_{norm} and C_{norm}) and diseased (R_{dis} and C_{dis}) parameters for each zone.

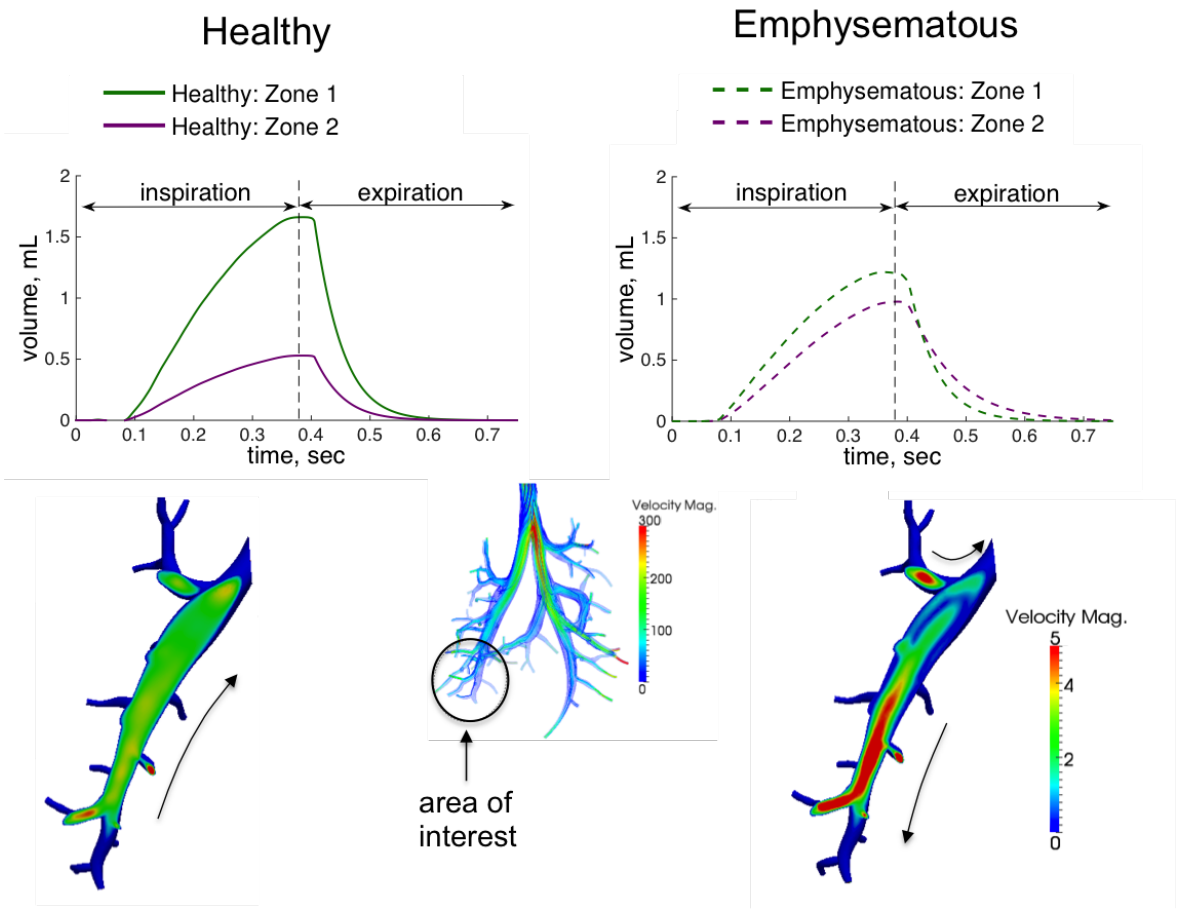

Figure 4.5: Inhaled volume over time for zones defined in fig. 4.4, comparing healthy and emphysema cases. Zoom on a zone of interest (mix of zones 1 & 2) showing for each case velocity magnitude and flow direction.

4.5). Besides, these healthy regions are less ventilated (lower tidal volume, lower velocities) than in normal rats, and conversely diseased regions are more ventilated than in normal rats and slower to empty than the healthy regions. All these facts influence particle deposition and delivery. It is possible that this asynchrony becomes more significant as the disease progresses, causing air to be trapped. Particles suspended in this trapped air will likely have more time to sediment and deposit. This failure to flush out potentially harmful particles could contribute to accelerated disease progression.

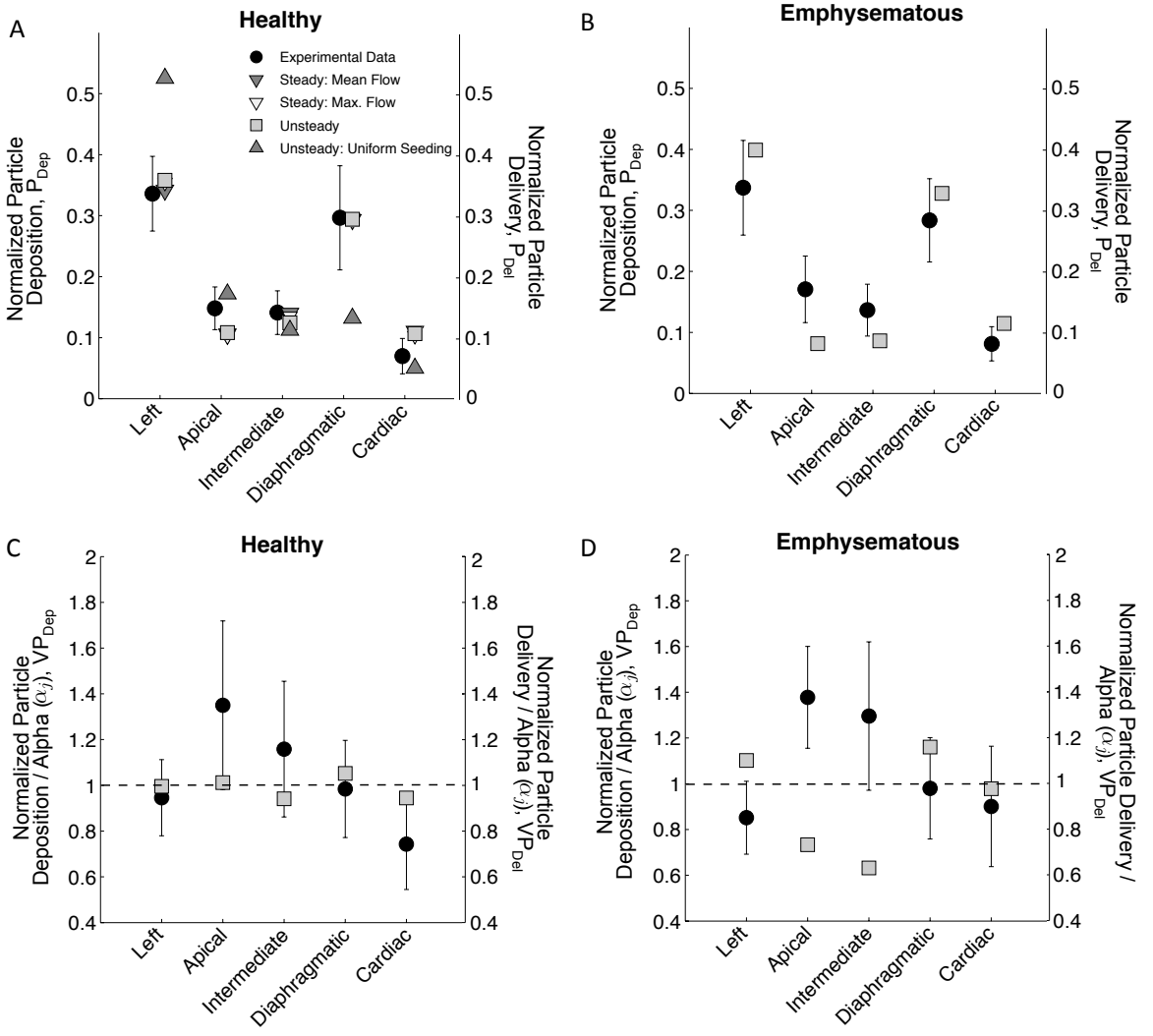

Figure 4.6: Panels A and B: comparison of P_{Del} and P_{Dep} [Oakes et al., 2014] for the healthy (uniform and parabolic seeding, panel A) and the emphysematous (panel B) rats. The particle delivery results for the steady simulations at mean and maximum inhalation flow rate are shown in panel A. Panels C and D: VP_{Dep} [Oakes et al., 2014] and VP_{Del} for the 5 lobes of the healthy (panel C) and emphysematous (panel D) rat lungs. A value of 1 would indicate that deposition/particle delivery is proportional to lobe volume.

While both the steady and unsteady simulations reasonably predicted the lobar distribution of particles in the healthy case (fig. 4.6), the deposition patterns in the 3D geometry is quite different between the two (fig. 4.7). This finding indicates that if only lobar distribution is needed, steady simulations may be appropriate for the flow and particle properties considered in this study. However, unless the flow delivery to each lung region is known beforehand, emphysema ventilation can only be modeled using unsteady multidomain techniques, as the

one employed in the current study. Besides, unlike for the healthy simulations, we are unable to match the emphysema particle deposition experimental data (fig. 4.6). This is likely because the airways and pulmonary region downstream of the 3D geometry are lumped in the RC models. In the healthy simulations, it is possible that deposition efficiency downstream of the 3D geometry is relatively similar between lobes. However, in emphysematous lungs, where normal regions are neighboring diseased regions, the deposition efficiency is likely not the same between these different areas of the lung. Therefore other factors should be taken into account to understand emphysema (see section 5.3). For more detailed results on the flow dynamics, particle deposition results and discussion, we refer to [18].

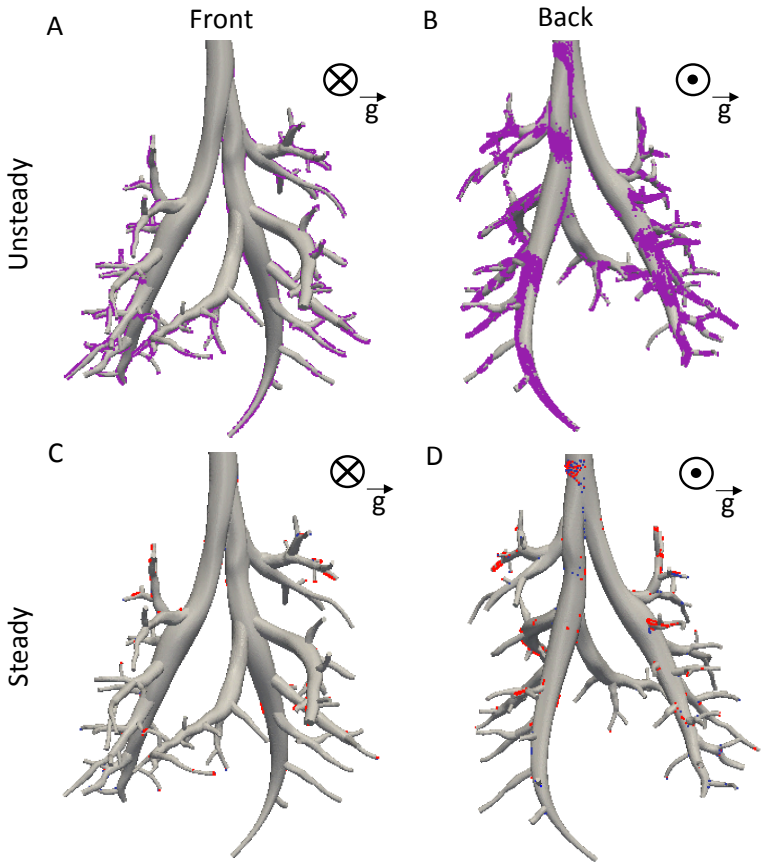

Figure 4.7: Particle deposition locations for the unsteady healthy (panels A and B) and steady simulations (panels C and D). For the steady simulations, blue and red particles were used for the mean and maximum flow rate, respectively.

4.2 Inverse problem for constant non-local targets - application to surgical planning in single ventricle physiology

In the above section, although the 3D region finally included a large number of branches, the pressure drop in the 3D part was negligible compared to the coupling pressure with downstream domains. Therefore, it was possible to derive parameters from a global 0D model and transfer this information directly into the 81 terminal 0D models. But this strategy does not work when the 3D part has a non-negligible resistance compared to the downstream ones, and actually influences the average flow repartition between the branches. Thus this section presents a strategy for such cases.

4.2.1 Parameter estimation for constant but distributed targets

Several stages of palliative surgery are required to connect the systemic and pulmonary circulations to the single ventricular (SV) power source (see 1.2.3). Accurate modeling of patient-specific physiology for clinical decision-making requires the integration of the patient's clinical data into numerical simulations [3]. CFD studies of SV conditions [13] [Bove et al., 2003, de Zélicourt et al., 2010] have presented the crucial aspect of specifying the relevant boundary conditions. Multidomain methods (sections 3.1, 3.2) have been favored to take into account the effect of the distal pulmonary vascular trees (e.g. for SV [13, 3] [Pennati et al., 2011, Ceballos et al., 2012] and citing references). This allows one to obtain information about local fluid dynamics due to changes in anatomical features resulting from surgical operations [4, Kung et al., 2013]. Besides, when the 3D-0D model is closed loop, changes on and from the heart or other key systemic factors, can be evaluated from the known preoperative patient state for these different virtual surgeries [4, Kung et al., 2013]. Nevertheless, such multidomain models need patient-specific parameters to be an effective tool for clinical support in surgical planning. The current work provides the parametrization of the 0D components that are in direct contact with the multibranched 3D model, where neither flow nor pressure are known.

In cases of pure zero-dimensional models, a number of methods for parameter identification were applied to minimal models of the adult systemic arterial circulation [Stergiopulos et al., 1999, Segers et al., 2008], and submodelling or sensitivity analysis were suggested to reduce the identification complexity in closed-loop models of the whole cardiovascular system [Pope et al., 2009, Hann et al., 2010, Sughimoto et al., 2013, Liang et al., 2014]. However, these methods cannot be applied easily to 3D-0D modeling because of very high computational costs. Considering multidomain models, a possible approach consists of manually tuning lumped parameters [Pennati et al., 2011]; however, this simple method requires intuition regarding hemodynamics, and has been found to be infeasible if the 3D geometry has multiple branches. Automatic parameter estimation methods have thus been developed (see 1D and 3D references in section 4.3). These different methods, although effective, are demanding in terms of numerical implementation or numerical costs. They have the advantage, however, of matching time-varying measurements. We note here the work of [D'Elia et al., 2012], in which a variational control approach is successfully tested for the linearized steady Navier-Stokes equations to control the input traction to match velocity information given in different slices of a vessel. This approach is also computationally heavy. Our first aim here, is to provide an automatic parameter estimation for multi-branched geometries, whose complexity is coherent with the type of available data. As described in the next section, clinical measurements are limited in single ventricle patients (only a few months or years old) immediately prior to surgery. Namely, classical identification of the outflow impedances (compliances and resistances) for each vascular branch cannot be achieved since complete arterial pressure and flow tracings are usually lacking, and sometimes only the average values are available.

We have first developed an alternative approach [23, 43] consisting of two steps: i) total downstream resistances are identified for each pulmonary outlet; ii) each resistance is split and compliance is derived, using a morphometric approach and according to literature scaling rules (e.g. relative role of arterial and venous vascular beds). In [23] a simple method has been introduced to iteratively tune total outlet resistances of the 3D model and match clinical inlet average pressure, inlet average flow and outlets' flow repartition. In this following work, we extend the method for more general pressure clinical data localization, as clinical data are rarely available at the specific 3D boundaries. We can recast these different situations as an inverse problem for which given a set of measurements to match (target values vector $\mathbf{V^T}$) find the vector $\mathbf{R}$ of resistances $(R_i)_{,i=1...N}$ for the 3D-0D coupled Navier-Stokes equations. N is the number of outlets. In other words, we are looking for the fixed-point $\mathbf{R}$ of the following problem:

$$\mathbf{R} = \mathbf{g} \circ \mathbf{f}(\mathbf{R}) \text{ such that } L(\mathbf{f}(\mathbf{R})) = \mathbf{V^T} \tag{4.5}$$

Let us now define these different components in their biomedical context and the associated fixed-point algorithm. We concentrate on the pre-stage 2 case [19] to avoid complex terminology, but pre-stage 3 work of [23] can be describe in the same framework.

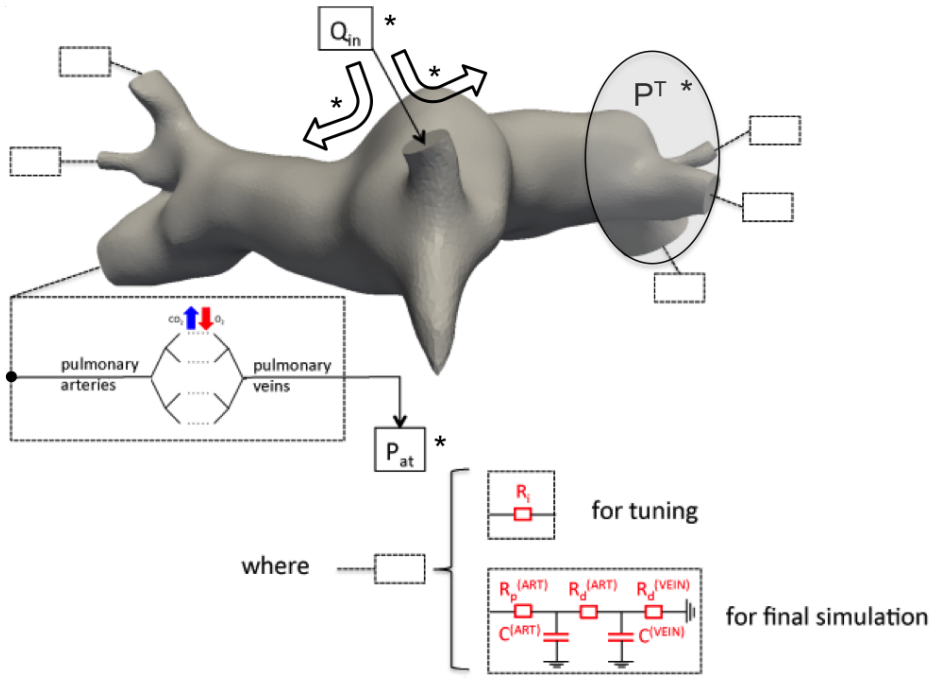

Figure 4.8: multidomain set-up, with the 3D domain, its inlet face on which the inflow Q_{in} is prescribed, and the distal pulmonary circulation for each outlet that all merge in the single atrium defined by its pressure P_{at}. Clinically measured quantities are marked with a star. At each outlet (dashed rectangle), the pulmonary arteries, capillaries and veins are represented either by a single total resistance for tuning, or by a more complete 5-parameter reduced model for virtual surgery [43, 44].

We refer to [19] for the description of the six patients pathology (labeled A–F), medical imaged-based geometry reconstruction and measurements protocols of the hemodynamics data from cardiac magnetic resonance imaging (usually abbreviated as CMR) and cardiac catheterization. The inflow to the model Q_{in} is measured and directly applied as a boundary condition to the Navier-Stokes equations (see section 2.1.1). P_{at}, the measured single atrium pressure is the end pressure of the multidomain model. The main challenge of this study is to determine outflow boundary conditions for each patient-specific model that are consistent with the clinically measured data, which themselves are nonlocal measurements of the 3D model (see fig. 4.8): 1) time-average flow distribution (flow split) between left and right sides defined as $\text{fs} = \frac{Q_\text{R}}{Q_\text{L}+Q_\text{R}}$ with evident notations, and 2) time-average pulmonary artery (PA) pressure denoted by P^T, which is the target pressure to match, and whose location and definition vary for each patient. Besides for validation purposes, pressure differences between left and right sides when measured were considered negligible (0-1mmHg) for patient A, B, D, F whereas for patient E it was 3mmHg. For patient C, the measurement was done on the left, and the pressure difference was assumed negligible (this case will be discussed later). All theses values are reported in Table 4.1. For each case, one can thus define $\mathbf{V^T}$ as the target values (P^T,fs).

But the inverse problem is certainly ill-posed to find a unique vector of outlet resistances $\mathbf{R}$ given that there are typically 6-20 outlets. Thus the inverse problem is completed by assumptions on the flow repartition between the branches: the mean flow rate (Q_i^T), that is the target to reach through an outlet i, is assumed to be proportional to the surface area of this outlet (S_i): $Q_i^T \propto S_i$. A power law could also be used if relevant [23]. A target average value for the flow rate at outlet i is thus a function of the inlet flow rate ($\mathrm{Q_{in}}$) coming from clinical measurements:

$$Q_i^T = Q_{\mathrm{in}}\Big(\delta_{i\mathrm{r}}\mathrm{fs} + (1-\delta_{i\mathrm{r}})(1-\mathrm{fs})\Big)\frac{S_i}{\sum_j S_j\delta_{ij}} \tag{4.6}$$

where $\delta_{i\mathrm{r}}$ is the kronecker symbol equal to 1 if outlet i is on the right side and 0 if not, and δ_{ij} is the kronecker symbol equal to 1 if outlet j is on the same side as outlet i and 0 if not. $\mathbf{V^T}$ is thus (P^T,$(Q_i^T)_{i=1...N}$).

The algorithm is then run as follows (see [19] for information on adaptive meshing, numerical discretization and solvers of the multidomain simulations, numerical parameters, etc.):

1. A first value of R_i at each outlet is estimated to initialize the algorithm, usually by neglecting 3D pressure losses.

2. This sets the 0D values for a 3D-0D coupled Navier-Stokes simulation that is run with sufficient time steps in order to reach stable state results [typically a few 100 time steps for steady simulations and four cardiac cycles for pulsatile simulations. Note here, that even in case of steady inlet flow (so called "steady simulations"), the resulting 3D flow is unsteady due to its complex interaction with the patient-specific geometry. Therefore, we use a transient formulation even for steady boundary conditions.] By post-processing the results over the last stable period, time-averaged (and mean in space) pressure ($P_i^{3\mathrm{D}}$) and flow rate ($Q_i^{3\mathrm{D}}$) are computed at each outlet, leading to the N-value vectors $\mathbf{P}^{3\mathrm{D}}$ and $\mathbf{Q}^{3\mathrm{D}}$. The function $\mathbf{f}$ in eqn. 4.5 has thus been defined: $\mathbf{f} : \mathbb{R}^N \mapsto \mathbb{R}^N \times \mathbb{R}^N$ such that $(\mathbf{P}^{3\mathrm{D}}, \mathbf{Q}^{3\mathrm{D}}) = \mathbf{f}(\mathbf{R})$.

3. $L\left(\mathbf{P}^{3\mathrm{D}}, \mathbf{Q}^{3\mathrm{D}}\right) = \mathbf{V^T}$ in eqn. 4.5 is now defined as the linear operator identity for the flows and the following operator for the pressures: the controlled pressure ($P_c^{3\mathrm{D}}$) that varies according to the measurement location and clinician input is then calculated. Note that the exact pressure measurement location is unknown, hence this controlled pressure cannot be related to the output pressure at a specific location in the 3D domain. Rather, if catheterization was performed on the left pulmonary side, $P_c^{3\mathrm{D}}$ is the average pressure over all the outlets of the left side ($P_i^{3\mathrm{D}}$, $i \in [0, N_l]$ for N_l the number of left pulmonary outlets). Sometimes, there were several measurements done on one or both sides; $P_c^{3\mathrm{D}}$ is then defined together with clinical experts as being the maximum or minimum value over all the corresponding branches of number N, e.g.

$$P_c^{3\mathrm{D}} = \min_i P_i^{3\mathrm{D}}, i \in [0, N] \tag{4.7}$$

   These different options define *the measurement for tuning* and *control method* reported in Table 4.1.

4. The results are then compared to the target pressure and flow values, i.e. the residual $L\left(\mathbf{P}^{3\mathrm{D}}, \mathbf{Q}^{3\mathrm{D}}\right) - \mathbf{V^T}$ is computed with the following norm:

$$\begin{aligned} \varepsilon_P &= \frac{|P^T - P_c^{3\mathrm{D}}|}{P^T} \\ \varepsilon_Q &= \left(\frac{1}{N}\sum_{i=1}^{N}\left(\frac{Q_i^{3\mathrm{D}} - Q_i^T}{Q_i^T} - \frac{1}{N}\sum_{i=1}^{N}\frac{Q_i^{3\mathrm{D}} - Q_i^T}{Q_i^T}\right)^2\right)^{\frac{1}{2}} \end{aligned} \tag{4.8}$$

5. If convergence is reached within a certain tolerance the process stops. Otherwise before continuing with step 2., outlet resistances $\mathbf{R}$ are updated with the following function $\mathbf{g} : \mathbb{R}^N \times \mathbb{R}^N \mapsto \mathbb{R}^N$ which components $R_i = g_i(\mathbf{P}^{3D}, \mathbf{Q}^{3D})$ are defined as:

$$R_i = \frac{P^T - (P_c^{3D} - P_i^{3D})}{Q_i^T} \tag{4.9}$$

In the case of a flow time-tracing being used as inflow, pulsatile tuning simulations are performed, which better capture nonlinear effects across the 3D domain; total resistances (R_i) are also applied as boundary conditions, while pulsatile flow is imposed at the inlet. The controlled variables (P_c^{3D}, Q_i^{3D}) are then the time-averaged values over the last cardiac cycle. The framework presented above is the same for steady and pulsatile simulations. The steady tuning simulations are performed for all six patients, whereas the pulsatile ones only for patients A and E.

Patient	A	B	C	D	E	F
Age (months)	6	4	5	5	3	4
BSA (m^2)	0.34	0.28	0.34	0.30	0.26	0.27
Inflow (cm^3/s)	7.5	12	20	9.7	12	16.6
Re_{max}	2300	1750	2900	2500	3000	4150
fs	0.64	0.46	0.55	0.46	0.67	0.52
PA pressure (mmHg)	12.8	12.7	13.5	12	17	11
$\Delta P_{L/R}$ (mmHg)	negl.	negl.	negl.?	negl.	3	negl.
Meas. loc. for tuning	both	LPA	LPA	both	RPA	both
Control method	average	average	average	average	min	max
fs^{3D}	0.64 (0.64)	0.46	0.55	0.46	0.66 (0.67)	0.52
P_c^{3D} (mmHg)	12.3 (12.4)	12.7	13.4	12.0	17.0 (17.0)	11.0
$\Delta P_{L/R}^{3D}$ (mmHg)	0.4 (0.4)	0.7	0.5	6.0	3.0 (3.0)	0.2

Table 4.1: Clinical measurements, numerical method and results. For each patient, clinical data (age, BSA, average pulmonary inflow, deduced Reynolds number Re_{max}, flow split fs, target pulmonary artery pressure value, negligible or not left/right pulmonary pressure difference), tuning set-up (left or right pulmonary side, and control method to define P_c^{3D}), and numerical results in red (obtained flow split fs^{3D}, controlled pressure P_c^{3D} and pressure difference between left and right sides $\Delta P_{L/R}^{3D}$). Numbers are for the steady tuning and in parenthesis for the pulsatile tuning.

4.2.2 Results

Table 4.1 reports the tuning results. Steady tuning was run for every patient: the results (fs^{3D} and P_c^{3D}) are very close to the targeted clinical data. However, if we focus on the not targeted quantity ($\Delta P_{L/R}$), the model predictions are satisfactory only in five cases. Indeed, according to clinical observations, the pressure difference between right and left lungs is significant only for patient E, whereas the calculated $\Delta P_{L/R}^{3D}$ is significant for both patients E and D. This issue is considered in detail in the next section. Fig. 4.9 illustrates the convergence of the tuning algorithm for pressure and flow: both errors are under 2% for all patients, except for patient F where ϵ_Q is 5%. Pulsatile tuning was also performed for patients A and E and led to results (reported in parenthesis in table 4.1) all very close to both steady tuning and targeted clinical values. As a consequence, the next paragraphs only report the 3D results of the steady tuning.

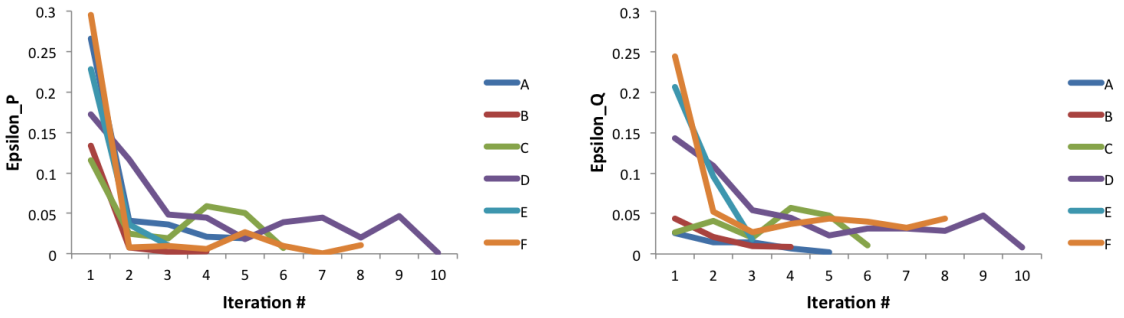

Figure 4.9: Convergence of the tuning algorithm shown for pressure (ϵ_P) and flow (ϵ_Q) for patients A-F.

Historically, very little CFD work has been performed at pre-stage 2 and pre-stage 3 surgeries (for more precise information, see [23] for pre-stage 3 surgeries, and [19] for pre-stage 2 surgeries). To the best of our knowledge, no prior computational study exists on patient-specific pulmonary hemodynamics in the presence of a systemic-to-pulmonary shunt and appropriate boundary conditions. The second aim of such study is hence to provide a first characterization of blood flow behavior in the distal anastomosis of the systemic-to-pulmonary shunt, and the connected pulmonary arteries over several bifurcations, in a number of different single ventricle patients scheduled for stage 2 surgery [19] - and similarly in [23] for stage 3 surgery.

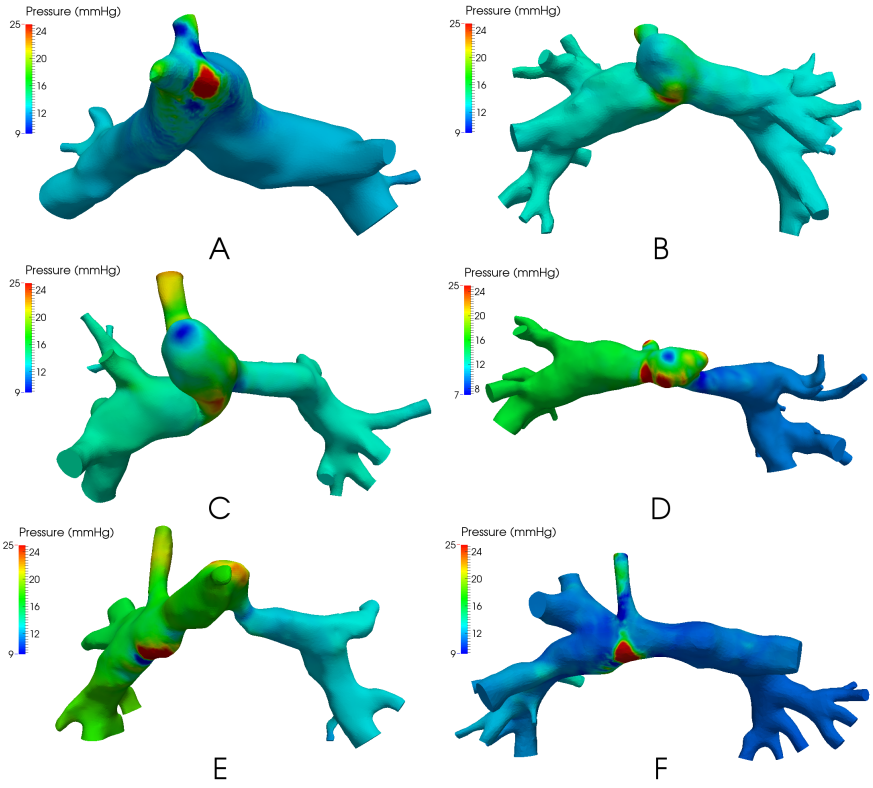

Figure 4.10: Pressure maps for patients A-F. Maximum pressure is equal to 25 mmHg on the color scale, even if the real maximal pressure is larger. 1 mmHg = 133.3 Pa.

In fig. 4.10 the pressure map for each patient is presented at the end of the tuning. We

observe a high peak of pressure on the wall. The maximum pressure for patients A, B, C, D, E and F are respectively 52, 26, 25, 45, 62 and 74 mmHg. The patients A, B and F have homogeneous pressure in both pulmonary arteries respectively, approximately 12, 13 and 11 mmHg. Moreover, patients D and E have a left pulmonary artery (LPA) stenosis which involves a significant pressure loss of approximately 6 and 3 mmHg respectively, while homogeneous pressure is found in the right pulmonary artery (RPA). A last remark concerns patient C who has a kink in the RPA close to the shunt. The kink does not generate a significant pressure loss and pressure is homogeneous in both PAs, around 13.5 mmHg.

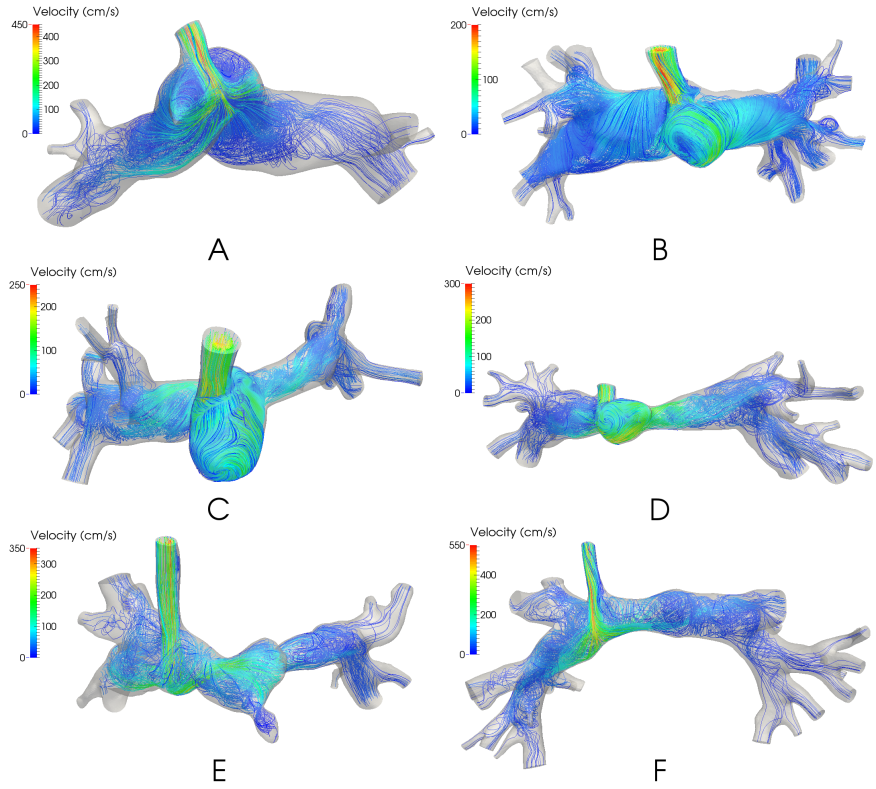

Figure 4.11: Streamlines of patients A-F colored by velocity magnitude.

In fig. 4.11 blood flow patterns for each patient are presented at the end of the tuning. A very complex flow can be observed in the 3D geometrical domain, especially close to the shunt where blood flow is the highest. Highest velocity is obtained in the center of the shunt and is respectively equal to 470, 250, 265, 319, 377 and 570 cm/s. For patients A, B, and F the blood is swirling in the pulmonary arteries close to the shunt and goes towards the outlets smoothly with less complexity. This mixing flow behavior extends into the main pulmonary artery stump for patients B, C, and D where the stump from the ligated vessel is prominent. For patient E, swirling reflects the tortuous geometry on the left side, where there is a constriction anastomosis near the main pulmonary artery stump, followed by an LPA stenosis. The results of this study highlight the high complexity of the blood flow patterns in pulmonary arteries in single ventricle patients approaching stage 2 surgery with a systemic-to-pulmonary artery shunt in situ. The variability of the pulmonary flow rate – between 7.5 and 20 cm^3/s – leads to very high Reynolds numbers, between 1750 and 4150 when computed at the shunt inlet with the maximum velocity.

Wall shear stress surface maps are discussed in detail in [19]. To summarize, for all patients the maximal wall shear stress is reached either in the shunt, or where there is a peak of pressure, stenosis or ligation, except for one patient where the opposite happens.

4.2.3 Discussion

This proposed methodology to tune reduced model parameters, adopted as outlet boundary conditions of patient-specific 3D pulmonary arterial models, accurately replicates clinical measurements (table 4.1), within acceptable clinical measurement tolerance limits. As the pressure difference between the left and right side was not used for parameter tuning, the fact that this measurement is well-matched by the simulations constitutes a preliminary validation of the results.

At the 3D outlets, it would not be relevant to apply pressure boundary conditions for the following reasons: 1) the measured flow distribution between the two different lungs cannot be easily matched, and 2) the pressure measurements were not performed at these locations in the pulmonary arteries. Sometimes, applying the same pressure at all outlets can even lead to unphysiological reverse average flow in some of the branches. Applying time-varying flow boundary conditions would also be difficult because the flow distribution between the different outlets is not necessarily constant, and would not guarantee coherence with the pressure measurements. Moreover, prescribing pressure or flow reduces the predictive potential such as in virtual surgery planning [3]. This is why we coupled 3D Navier-Stokes equations to reduced models.

The tuning methodology introduced in this work consists of coupling Navier-Stokes equations to reduced models (here resistances) at the outlets and running steady or pulsatile simulations. The *a priori* interest in running a pulsatile simulation is the integration of all non linearities due to the 3D geometrical model, and to obtain a more accurate set of reduced model parameters. However, to achieve periodic stability, pulsatile simulations need to be run over 4 cardiac cycles (around 2000 time steps) and the iterative process converges within 5 iterations, thus around 10000 time steps. In comparison, 100 time steps for a steady stimulation were enough and the iterative process converges in 5 iterations (tolerance of 0.05), thus around 500 time steps were necessary in total. Furthermore, pulsatile tuning for patients A and E was performed, and both matched targeted clinical values were very close to the steady tuning results. Moreover, the reduced model parameters were very close to those obtained by steady tuning. Indeed, for patients A and E the difference between steady and pulsatile tuning are respectively 6.37% and 7.82% in resistances, computed by the formula (4.8).

See [19] for more discussion on the choices of inflow velocity profile and rigid wall assumption, number of included branches and sources of uncertainties (see also section 5.4).

4.2.4 Application to surgical planning in single ventricle physiology

The third aim of this work is to provide some concrete examples of how patient-specific integration of clinical data and computational modeling can provide interesting insights to clinicians.

The importance of the severe PA stenosis causing a pressure drop, and the swirling behavior of the blood flow was also shown. This complexity is induced by the high Reynolds number in the shunt. For these stenosis cases and patient C with its PA kinks, computational fluid dynamics complements information from clinical measurements. One potential clinical application for this technique is to aid clinicians' understanding of the significance of anatomical abnormalities in these complex patients. For example, patient C appears to have a significant geometric 'kink' or restriction in their RPA, just distal to the shunt. Only a distal LPA pressure measurement was obtained clinically, so the hemodynamic effect of this lesion was unknown. However, simulation results clearly indicate that the pressure difference between the shunt anastomosis and the PAs are equal on the left and right sides. This was of interest to the clinicians, as the consensus was that judging by the anatomy alone, they would expect a pressure loss across the RPA. Indeed, at stage 2 surgery, patients A, C, D, and E all underwent patch augmentation of their central PAs or proximal LPAs judged on the appear-

ance of the geometry alone. This work suggests that in some cases the clinician's perception of what constitutes a geometric abnormality may actually not result in a hemodynamically significant pressure difference, as in case C. Although, the tortuous course of the PA appears to constitute a stenosis, it is partly an illusion due to the distal PA having a relatively large cross-sectional area.

For patient D, the first attempt was to match the measured flow split of 0.46 and a pressure on both LPA and RPA sides equal to 12 mmHg. Unfortunately, setting target flow split as 0.46 induced a pressure difference between the left and right sides of approximately 6 mmHg, which was not acceptable from a clinical point of view. Discussions with clinicians led us to disregard the clinically measured flow split. By imposing the same average pressure on both sides, a flow split of 0.54 (more flow to the right side) was then found, which was clinically acceptable. The differences in flow split would correspond to an error of 0.78 ml/s (i.e. 8 %) in estimating flow with CMR. This example highlights the impact of uncertainty of measurements on the numerical simulations. It could be interesting to investigate more precisely the effect of uncertainties of pressure and flow split measurements on the pressure loss through the stenosis (see section 5.4). This patient-specific example was thus challenging and required a close collaboration with clinicians. On the other hand, performing simulations underlined the potential for incoherence of the original clinical measurements ; and joint assessment with clinical experts elucidated which data was more reliable to utilize.

A last comment regarding uncertainties of clinical measurements: in fig. 4.12 simulated velocity vectors for patient D are shown at the same locations as flow measurements were performed in CMR. We highlight the complexity of the blood flow patterns at these locations, which might explain the difficulty obtaining accurate clinical time-varying velocity measurements by CMR at these locations. The PAs are relatively small, and are receiving flow from the aorta, or one of its branches, at high pressure. CMR flow measurements are typically less reliable in areas of complex flow because unpredictable phase shifts occur. This often leads to signal loss (voiding) and inaccurate flow measurements [Oshinski et al., 1995]. Typically, the PA flow measurements in this location would be underestimated in pre-stage 2 patients. The pulmonary veins may represent a more stable location to measure the pulmonary flow split, however, the physiology of these patients sometimes leads to the pulmonary veins receiving additional blood flow external to the pulmonary arteries. It is only through the iterative process of comparing simulation results to clinical measurements that suitable strategies for managing measurement uncertainty are reached.

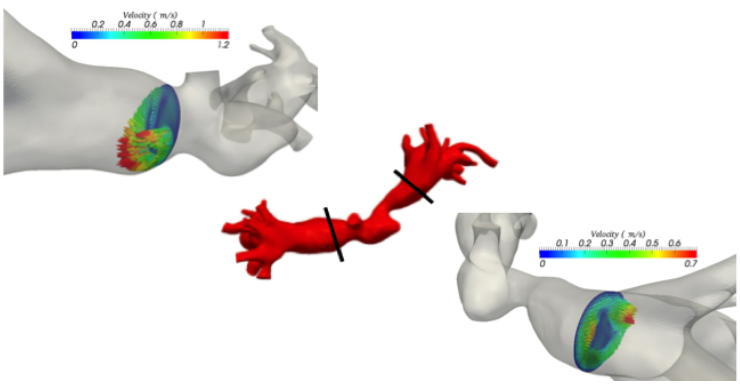

Figure 4.12: Velocity vectors (colored by their magnitudes) from the 3D simulation shown at the locations where the CMR flow measurements were performed.

Finally, the work above enabled surgery planning based on preoperative patient-specific data. A workflow of virtual surgery planning for two Hemi-Fontan patients is presented in [Kung et al., 2013]. Two standard ways of performing stage 2 surgery (Glenn vs Hemi-Fontan)

are studied in [4]. [40] proposes a way to integrate data from different time-points and [40, 43] study the inclusion of collateral flows. Stage 3 surgical planning has been investigated in [3] to successfully predict venous central pressure (linked to the head) on one patient, in [5] to study different surgical variations, and in particular a novel 'Y' shape, and in [6] to optimize the artificial surgical graft. Respiration, exercise and close-loop modeling impacts have been studied in [24, 36].

4.3 Data assimilation for time-varying observations - applications to congenital heart diseases

In the previous section, a strategy was proposed to tune reduced parameters of coupled 3D-0D systems where the resistance in the 3D part is non-negligible compared to the global one. It was designed to satisfy non-local target measurements (e.g. max over a region) but, as other variational approaches, it cannot easily match time-varying measurements. In this section, we thus develop an approach to take into account the richness of such measurements.

4.3.1 Data assimilation for time-varying observations

For a patient-specific multidomain or purely 0D flow analysis, reduced models need customization for each patient individually. While it is natural that their parameters be estimated via some patient-specific clinical measurements such that the discrepancy between model output and the measurements is minimized, the inverse problem is challenging, particularly when the number of parameters to be estimated is high. The problem is further exacerbated by uncertainty in the clinical measurements. As mentioned before, a manual tuning of the parameters could be performed, but it is a long process requiring much biomechanical and physiological expertise (see for example, [24]). Automatic approaches, on the other hand, are mostly confined to either models with a low number of estimated parameters [Hann et al., 2010] or open-loop circulatory models with simplified boundary conditions [19] [Spilker and Taylor, 2010]. Furthermore, such methods typically make inherent hypotheses about the ratios of different parameters [Spilker and Taylor, 2010] or consider only the major model parameters [Sughimoto et al., 2013] to reduce the total number of free parameters. Besides, in certain applications, pressure and flow information are available at different locations, but contrarily to the section above, their time variations are acquired with sufficient precision to be trustable. Hence this section aims at presenting a strategy to take advantage of this richness of the data that we have developed over the last years [17, 20, 45, 26].

Data assimilation is a process by which real measurements (partial observations of the system state) and 'a first guess' (prior knowledge) of the initial state are integrated into a computational model to reduce its uncertainty in representing the real system. In the context of blood flow, it has mainly been used for parameter estimation by treating the parameters as state variables; thus requiring prior knowledge of the parameters as well. Basically it entails to minimize a cost function which is composed of a sum over time of the discrepancy between the observations and the corresponding functions of the state variables in a certain norm, and of the norm of the uncertainties in the initial state and parameters. Depending on the norms, one chooses to put more trust (weight) on the data or on the *a priori* knowledge. The problem is then solved either by *variational methods* or by *sequential approaches*.

Variational approaches have most commonly been used for estimating blood flow 0D parameters, including transformation to a linear least-square problem in 0D [Hann et al., 2004], Nelder-Mead simplex method in 0D [Segers et al., 2008, Sughimoto et al., 2013], quasi-Newton method in 3D [Spilker and Taylor, 2010], adjoint-based method in 3D [Ismail et al., 2013b]. Other iterative approaches include fixed-point/control-system based methods in 0D [Hann et al., 2010, Hann et al., 2011, Revie et al., 2013], in

1D [Xiao et al., 2014] and 3D [23, 19]. All these methods usually employ targets of the mean/extrema values or scalar shape descriptors of the clinical measurements and are successful only when a few parameters are to be estimated. An alternate approach for parameter estimation that has gained a lot of attention in recent years is the sequential Kalman filtering-type method that takes advantage of time-varying measurement curves. These methods have been applied in hemodynamics primarily to estimate tissue/wall material properties in 1D or in 3D [Bertoglio et al., 2012, Moireau et al., 2013, Bertoglio et al., 2014, Lombardi, 2014]. Hemodynamics parameters such as Windkessel parameters have only been estimated in 1D [DeVault et al., 2008, Lombardi, 2014]. Note that in [Bertoglio et al., 2012], a proximal resistance is estimated in a 3D FSI aneurysm based on synthetic wall displacements, which has led us to try this approach but based rather on pressure and flow information.

The general filtering method is now briefly described. Consider a dynamical system described by state variables $\mathbf{x} \in \mathbb{R}^d$, $\mathbf{x} = [x_1, x_2, \ldots, x_d]^T$ and parameterised by $\boldsymbol{\theta} \in \mathbb{R}^p$, $\boldsymbol{\theta} = [\theta_1, \theta_2, \ldots, \theta_p]^T$, with following dynamics

$$\mathbf{x}_{n+1} = F(\mathbf{x}_n, \boldsymbol{\theta}), \tag{4.10}$$

where $\mathbf{x}_n$ and $\mathbf{x}_{n+1}$ refer to the state at times t_n and t_{n+1}. Eqn. (4.10) can, for example, be considered as a discretised form of the ODE system $\dot{\mathbf{x}} = \mathcal{F}(\mathbf{x}, \boldsymbol{\theta})$. Consider that at time t_n, measurements of vector $\mathbf{y} \in \mathbb{R}^m$, $\mathbf{y} = [y_1, y_2, \ldots, y_m]^T$ are available and related to the state through the observation operator H and measurement noise $\boldsymbol{\epsilon}$ as follows

$$\mathbf{y}_n = H(\mathbf{x}_n) + \boldsymbol{\epsilon}_n. \tag{4.11}$$

In the above, the noise at all measurement times is assumed to be independent and distributed according to a multivariate Gaussian distribution with zero mean and covariance $\boldsymbol{\Sigma}_n$. The goal of all filtering methods is to provide estimates of $\mathbf{x}_n$ recursively at each measurement time t_n through the measurements $\mathbf{y}_n$. This is achieved through two steps of propagation and correction. The general steps of a filter are as follows.

1. An estimate of state is assumed available at time t_n with mean $\hat{\mathbf{x}}_n$ and covariance $\mathbf{P}_n$
2. The forward propagation step involves propagation of the mean and covariance from t_n to t_{n+1} through the forward model of eqn. (4.10)
3. In the correction step, these means and covariances are corrected through the measurement of $\mathbf{y_{n+1}}$
4. They yield an estimate of mean $\hat{\mathbf{x}}_{n+1}$ and covariance $\mathbf{P}_{n+1}$ at t_{n+1}

Thus, starting from an initial estimate of the state with mean $\mathbf{x}_0$ and covariance $\mathbf{P}_0$, an estimate of the state is available at all times through the filter. Parameter estimation is performed by considering an augmented state containing the parameters $\mathbf{z}_n = [\mathbf{x}_n, \boldsymbol{\theta}_n]^T$ and adding trivial dynamics $\dot{\boldsymbol{\theta}} = 0$, *i.e.* $\boldsymbol{\theta}_{n+1} = \boldsymbol{\theta}_n$, for the parameters in eqn. (4.10). The filter is run on the augmented state $\mathbf{z}$, and the $\boldsymbol{\theta}$ component of filtered $\mathbf{z}$ at the last measurement time is taken as the final parameter vector estimate [20]. The estimate of the parameters depends on three factors: a) the manner in which the parameters affect the measured quantities, *i.e.* the operators F and H in eqns. (4.10) and (4.11); b) the uncertainty associated with prior knowledge about the parameters and the state, *i.e.* $\mathbf{x}_0$ and $\mathbf{P}_0$; and c) the uncertainty associated with the clinical measurements, *i.e.* $\mathbf{y}_n$ and $\boldsymbol{\Sigma}_n$. As a general rule for parameter estimation, the prior variances in $\mathbf{P}_0$ are set to relatively higher values compared to the variances in $\boldsymbol{\Sigma}_n$ to imply that initial guess of $\mathbf{z}_0 = [\mathbf{x}_0, \boldsymbol{\theta}_0]^T$ has less confidence when compared to the measurements [20].

While the steps of forward propagation and correction are common to all sequential filters, the Unscented Kalman Filter (UKF) employs a set of deterministically chosen particles

(usually $2d + 1$) to be propagated through eqns. (4.10) and (4.11) for the implementation of the two steps. This means that computationally, only $2d + 1$ simulations of the dynamical system be performed (as opposed to a significantly larger number when considering variational approaches such as minimization of loss function through gradient-descent based approaches). For the choice of unscented Kalman filter (UKF) for data assimilation, its appropriateness for parameter estimation in non-linear systems, and application to hemodynamics, [20] is referred.

The details of the UKF method and discussion with respect to parameter estimation in hemodynamics systems can be found in [20]. This includes how to enforce equality constraints, when there is a strong knowledge about certain relationships between the parameters to be estimated. A pseudo-observation method is favored here since in such a case the model dynamics need not be rewritten and constraints are added as fictitious observations (see for example [Tahk and Speyer, 1990]). The constraint equations are appended to the observation model and the observation variance for the constraints are controlled to specify how strongly the constraints are enforced. For the example of the Windkessel model (see section 2.1.3), an added observation of '$R_p + R_d - R_t$' (linking proximal and distal resistances to a known total resistance R_t) can be represented by a zero-mean random variable, r_{cons}, with variance σ^2_{cons} [De Geeter et al., 1997].

Such a method has been successfully applied to two idealized cases [20] and a patient-specific case of aortic coarctation ([20], section 4.3.3). The effect of various features of the UKF parameter-estimation method, such as the relative error between the initial state and the observations and the observation frequency, on parameter estimates has been discussed in [20]. The UKF has been implemented with the Verdandi library for data assimilation [Chapelle et al., 2013].

4.3.2 Sensitivity analysis and model complement

Sensitivity based analysis is needed to assess potential identifiability problems: the question whether the parameter estimation procedure with the available clinical/experimental data is likely to succeed; are the parameter estimates highly correlated; which sets of parameters should be combined together or fixed to improve identifiability, etc. A demonstration of the traditional sensitivity function [Bai et al., 2007] and the generalized sensitivity function (GSF, e.g. [Thomaseth and Cobelli, 1999, Bai et al., 2007]) is shown on various examples in [20]. The relative magnitudes of the traditional sensitivity functions between parameters represent the effect of changes in model parameters on model outputs in different intervals of time. GSFs characterize the sensitivity of parameter estimates with respect to data measurements. In particular:

- Sharp increase in GSFs implies high concentration of parameter information in the corresponding time-interval.
- Monotonically non-decreasing GSFs imply that the parameters are uncorrelated.
- GSFs exhibiting large oscillations imply large correlations between the parameters and hence potential identifiability problems.

Such an analysis on various cases, and in particular on an aortic model lead us to select set of measurements when identifiability problems can be avoided (see fig. 4.13). We observed that in general pressure at one location (usually inlet) in the system and flow-rates at all outlets are sufficient to identify the Windkessel parameters. This observation justifies that when only mean flow splits among different branches are known, an assumption to estimate flow-rate curves is required to complement the model and avoid identifiability problems. In practice, this means that one constructs a flow time-curve observation to which relatively low confidence is given, but one can add with a high confidence the mean value constraint.

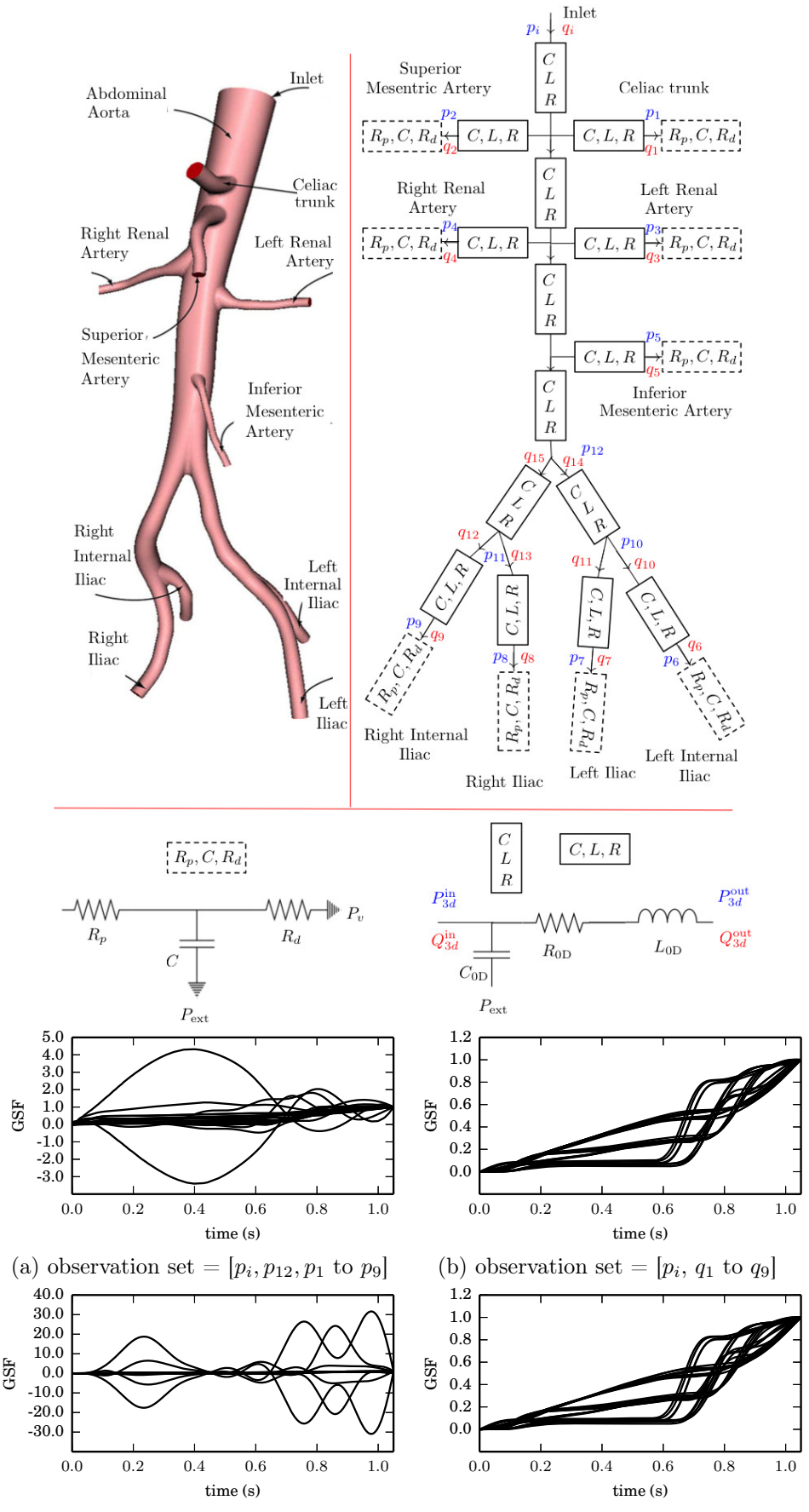

(a) observation set = $[p_i, p_{12}, p_1$ to $p_9]$

(b) observation set = $[p_i,\ q_1$ to $q_9]$

(c) observation set = $[p_0, q_1, q_2, q_3, q_4, q_5, q_8, q_9]$

(d) observation set = $[p_0, q_1, q_2, q_3, q_4, q_5, q_7, q_9, q_{15}]$

Figure 4.13: Top: 3D and 0D representations of the abdominal aorta, boxes in solid line represent known parameters and boxes in dashed lines represent parameters to be estimated. Bottom: GSF for several sets of observations.

4.3.3 Loosely coupled 3D-0D strategy for coarctation pressure gradient estimation

In this work a novel methodology for tuning the Windkessel (or other lumped model) parameters is proposed. This strategy employs the UKF approach (section 4.3.1) on a reduced order model (0D) whose accuracy is improved iteratively. It has all the advantages of a sequential estimation approach, and in addition involves a fast-to-compute model that can be run over enough cycles to match the given targets while being enriched by a few 3D simulations. The 0D model also provides a surrogate to quickly test and justify several modeling assumptions and their potential effect on the behavior of the 3D model. Fig. 4.14 provides the main steps of this algorithm.

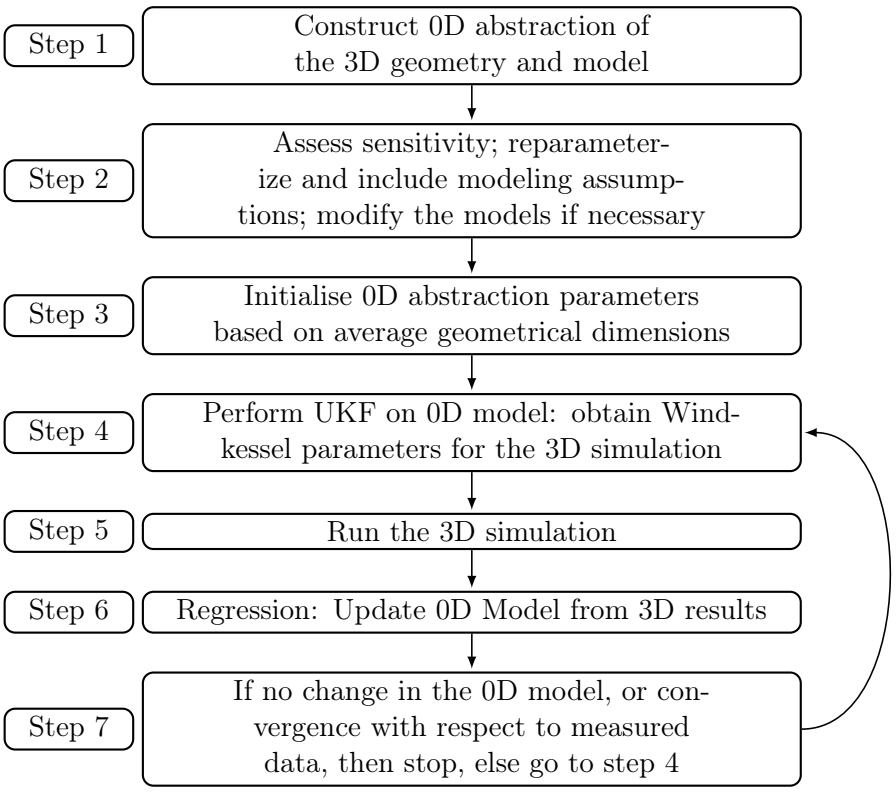

Figure 4.14: Algorithm for multidomain 3D simulations using sequential parameter estimation in a 0D model.

In this section a case of patient specific aortic coarctation is considered. This case was presented as part of the CFD challenge organized in STACOM 2013 [Camara et al., 2014]. For patients with aortic coarctation the pressure drop across the coarctation is the critical parameter to be assessed, especially under exercise conditions when the flow-rate is high. While invasive assessment of pressure drop across the coarctation is relatively easy during rest conditions, the same task becomes difficult in exercise conditions as the physiological conditions are hard to replicate in a clinical environment. Consequently, sometimes a 'pharmacological stress-test' is preferred [Camara et al., 2014]. The goal in this case is to assess whether CFD and appropriate application of boundary conditions can both reproduce the available clinical measurements and subsequently predict the pressure drop across the coarctation in two physiological states of rest and stress.

Besides the geometrical surface information, pressure curves in the ascending aorta and flow curves in both the ascending and the descending aorta were provided. These are shown in fig. 4.15 for the physiological state of rest. The mean flow rates in the supra-aortic branches

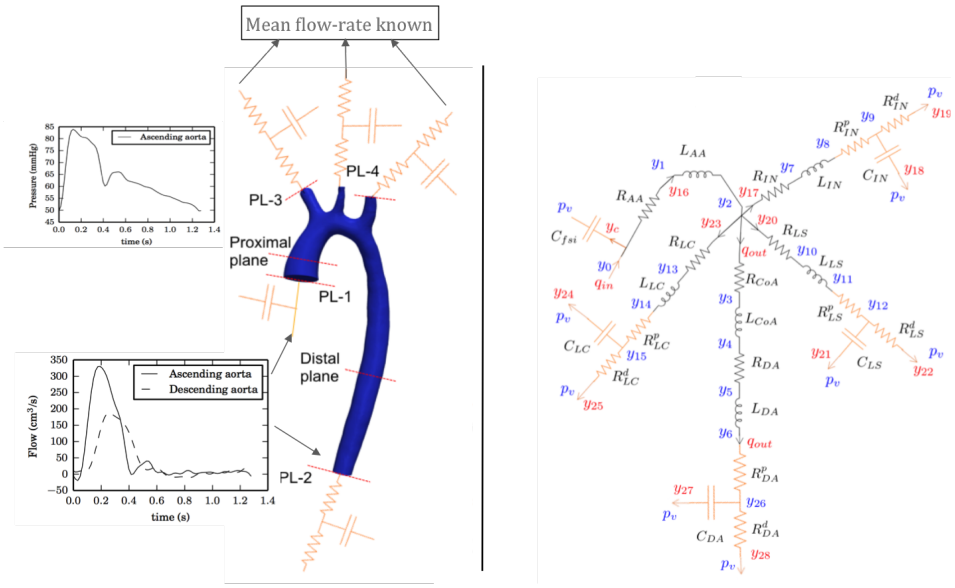

Figure 4.15: 3D model and corresponding 0D representation (in black), and observations. Windkessel boundary elements are represented in orange. Variables in red indicate flows and variables in blue indicate pressures. In the 0D model: IN represents the innominate artery; LC the left carotid artery; LS the left subclavian artery; AA the ascending aorta; DA the descending aorta; CoA the aortic coarctation.

were also provided. Given these measurements the aim of this study is to demonstrate that the algorithm above can be used to tune the Windkessel boundary parameters so that the CFD results closely match the clinically measured data, and hence predict the pressure drop across the coarctation. The pressure in the descending aorta was measured but not disclosed before the end of the CFD challenge. The overall 3D blood flow parameters and numerical methods are presented in [17], our article in the CFD challenge. For the set up of the parameter estimation aspects, including different Dirichlet and Windkessel boundary conditions in the descending aorta, and detailed discussion on the results we refer to [20]. It is demonstrated there that the data measurement asynchrony can be accounted for to achieve physiologically realistic results. For the rest case three iterations and for the stress case seven iterations between the 0D and 3D simulations (fig. 4.14) are required for convergence. Since the UKF run times are negligible compared to a 3D simulation, in effect the cost of tuning the parameters and obtaining the final results are equivalent to three and seven 3D simulation runs for the rest and stress case, respectively. The proposed framework applied to this case results in a close match, less than 3% and 9% for the physiological states of rest and stress, respectively, between the measured data and the CFD results. The developed multi scale iterative algorithm is tested for prediction of the pressure-drop across the coarctation. It is observed that the numerical model closely predicts the mean pressure-drop and the peak-to-peak pressure-drop across the coarctation (table 4.2). Furthermore, it is shown that a Windkessel boundary condition is significantly less constraining than a Dirichlet boundary condition for the outlets and leads to physiologically realistic results. A discussion on the interpretation of the CFD results in relation to the clinically relevant quantities and the choice of modelling assumptions is also presented. Lastly, although resulting from flow modeling assumption, the Windkessel parameters obtained for rest and stress are consistent with the literature. Knowledge on how these parameters change with stress could thus be learned by such an approach.

Table 4.2: Prediction results for the patient-specific case of aortic coarctation

Quantity	REST		STRESS	
	CFD	Experimental	CFD	Experimental
ΔP_{mean} (mmHg)	2.0	1.2	12.6	14.5
$P_{\text{max}}^{\text{prox}} - P_{\text{max}}^{\text{dist}}$ (mmHg)	6.4	6.4	35.5	44.7
$(P^{\text{prox}} - P^{\text{dist}})_{\text{max}}$ (mmHg)	11.8	9.1	41.34	72.8

4.3.4 Perspectives

Note that apart from the mean-value estimates of the parameters, the UKF procedure also provides variances of estimated parameters, and as such uncertainty quantification based on the confidence in the measurements.

Of particular interest in this work is the estimation of a time-shift between the flow and pressure measurements. Since the flow and pressure measurements were not taken simultaneously in the patient, as typically is the case, the estimate of time-shift aligns the measurement curves as if they were synchronized. The problem of asynchronous measurements can lead to difficulties in both estimation of parameters and validation of numerical models. In this regard the results of the proposed method to estimate such uncertainty in the measurements are encouraging.

In conclusion, our approach has been to perform the parameter estimation on a 0D model, weakly coupled to the 3D domain of interest: the parameters of the 0D model that represent the domain of interest are iteratively inferred from 3D-0D simulations. We show here that this can be a successful strategy. In single-ventricle disease applications (see sections 1.2.3, 4.2 for background), the need to automatically parameterize closed-loop model of the circulation has triggered to test UKF on these large 0D models. Patient-specific parameter estimation is achieved in a heart model for this physiology [45]. Heart chambers are described in this work by a single-fibre mechanics model and valve function is modelled with smooth opening and closure. Patient-specific clinical measurements are used as boundary conditions in the model, as target curves for parameter estimation or for validation. UKF is employed for parameter estimation to closely reproduce the measurements and obtain physiologically realistic results. Then this work has been extended to closed-loop 0D model of the entire circulation (fig. 2.5), successfully estimating around 35 parameters for single ventricle stage 1 patients with and without atrio-ventricular valve regurgitation [26] (see fig. 4.16 for an example of parameter convergence and measurements matching). Methodological aspects such as nonlinear observation manager, strategy to enforce state variables amplitude, management of measurements taken at different heart rates are discussed in [46].

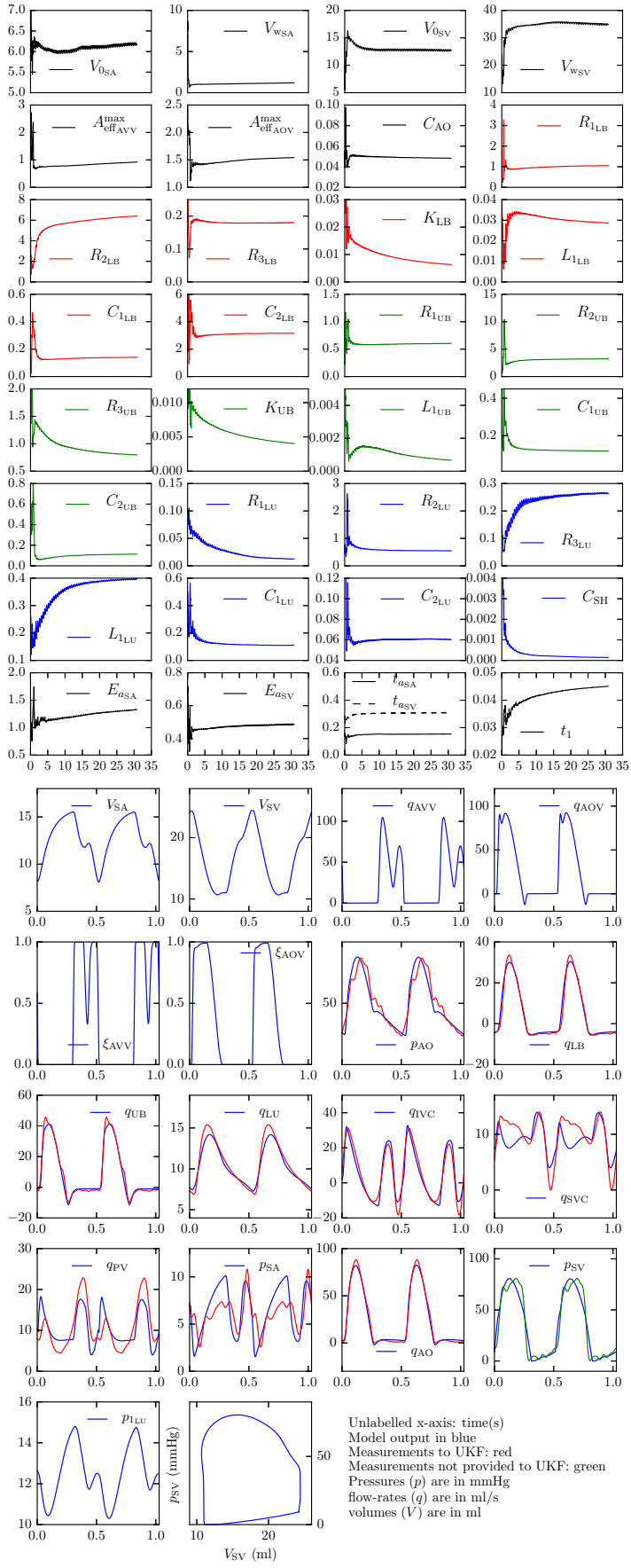

Figure 4.16: Parameter evolution with UKF (top) over 50 cardiac cycles; volumes are in ml, areas (A) in cm^2, linear resistances (R) in mmHg.s/ml, quadratic resistances (K) in mmHg.s^2/ml^2, compliances (C) in ml/mmHg, inductances (L) in mmHg.s^2/ml, and time in s. Forward model with the estimated parameters and measurements over two cardiac cycles (bottom).

"People who say it cannot be done should not interrupt those who are doing it."

Anonymous

5 Outlook

In the previous chapters, we have shown how bioclinical questions generate interesting modeling and numerical challenges and how we have addressed these questions coherently with the available data. Simulation results with these models contribute to solve the bioclinical questions, provide a new view on them, and guide new therapeutic strategies. This biomedical-mathematics interaction is however still in its infancy, in the sense that several obstacles remain to gain maturity. The acquisition of clinical data, its integration into a mathematical model and the model itself, however, all have inherent limitations and uncertainties which may affect simulation results and clinical decision making. In this chapter, we give a few directions to push the state of the art beyond these barriers. But there are, of course, many other challenges to face - such as reduction of computational cost for the direct or the inverse problem [Lassila et al., 2013, Bertagna and Veneziani, 2014, Sankaran et al., 2015] [47, 48]. There is an infinity of bioclinical applications for which no mathematical or numerical model exist and which would benefit from it. We have thus selected some that are promising based on our experience and new collaborations.

5.1 Towards a better understanding of non-invasive imaging data: parameter estimation of which model?

Medical non-invasive functional imaging is a very active medical image research field [Essig et al., 2013]. Unconventional MRI or CT image acquisition techniques have been the matter of intense research. However they have not yet reached clinical routine in a large part because the interpretation of the images is subject of debate. The image intensity at each pixel, varying in time, e.g. in dynamic contrast enhanced (DCE) perfusion imaging: DCE-MRI, DCE-CT or DCE-ultrasound, or with excitation mode, e.g. in diffusion weighted imaging (DWI)-MRI, is interpreted based on so called *compartment* or *pharmacokinetics* models that were constructed to represent as simply as possible the underlying structure and function of the imaged tissue. Inherent model hypotheses are often forgotten by users or their validity is not easy to assess in practice. Hence, we propose to assess such data interpretation procedure by comparison either with invasive imaging tissue analysis (e.g. postdoc of Yi Yin coadvised with Dirk Drasdo (INRIA) in collaboration mainly with medical doctors Oliver Sedlaczek and Arne Warth, and biologist Kai Breuhahn (U. Heidelberg Clinics) in BMBF project *Lungsys*) and/or with modeling. Let us now give an example of the latter.

DCE perfusion imaging has shown great potential to non-invasively assess cancer development and its treatment, even short term [Palmowski et al., 2008, O'Connor et al., 2011, Lassau et al., 2011]. In these imaging modalities, a contrast agent is injected in the blood stream, which when it spreads in the vasculature, and for non extravascular agents also permeates outside of it in-between tissue cells, gives rise to a signal representative of its overall concentration in the tissue. Different pharmacokinetics models (ODEs) are used, without consensus, to estimate parameters that are directly or indirectly linked to tumor cell density, vascular density, and perfusion parameters from DCE perfusion imaging. The interpretation of the indirectly related parameters changes with the regime of the true tissue parameters [Essig et al., 2013]. There is thus a need to provide a benchmark to evaluate and compare these different pharmacokinetics models. To this aim in-silico vasculatures can be constructed to solve the direct problem of contrast agent perfusion (intra-vascular transport, intra-extravascular exchange and diffusion within the interstitial space), with spatio-temporal coupled multiphase PDEs. Different pharmacokinetic models can then be evaluated from in-silico contrast-agent perfusion data. All these steps present interesting modeling or numerical challenges. The first results show that various tumor vascularizations (architecture and function) can explain diverse spatio-temporal contrast imaging dynamics characteristic of in-vivo tumor morphotypes (fig. 5.1 from Nick Jagiella's thesis [49], collaboration mainly with Dirk Drasdo (INRIA) and Oliver Sedlaczek (U. Heidelberg Clinics) in BMBF project *Lungsys*).

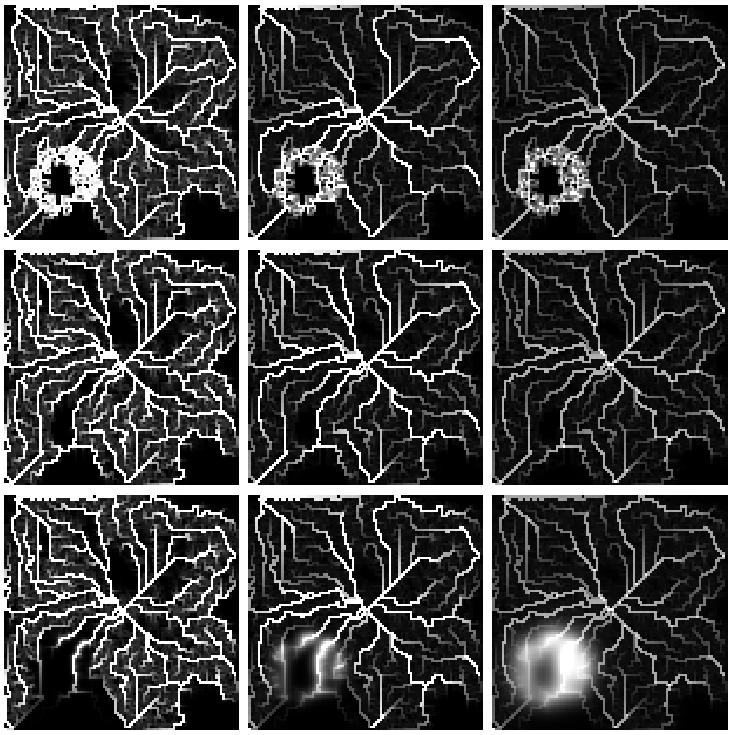

Figure 5.1: Reference case (middle row). Tumor rim either represented by an increase in microvascular density (top row) or in vessel 'leakiness' (bottom row). Columns represent numerical intensity results for different times after contrast agent injection.

Besides, inverse problems on common pharmacokinetics models indicate that taking into account space to estimate perfusion parameters may be key. Much more work on constructing robust parameter estimation procedures is thus warranted.

5.2 Modeling a new area: surgical planning in liver

Another research direction is introducing hemodynamics modeling in surgical planning of liver. With liver surgeons (Eric Vibert, surgeon at Paul Brousse Hospital and students Petru Bucur and Mohamed Bekheit) and other colleagues in ANR-tecsan *iFLOW* (companies FLUOPTICS and MID, and at INRIA, Chloé Audebert coadvised with Jean-Frédéric Gerbeau, Noémie Boissier coadvised with Dirk Drasdo), we are studying through a combination of pig experiments and blood circulation reduced models (see section 2.1.3) the unknown interplay between liver size, liver function and hemodynamics, to better avoid liver failure after large hepatectomies. This raises interesting modeling questions on liver circulation, the interaction with the rest of the circulation, vessel adaptation, blood loss and infusion; use of the model to understand the diversity of the data, to predict hemodynamics post-surgery with and without flow-controling devices, etc. Numerical challenges include the sharp change of hemodynamics, the possible collapse of some vessels (fluid-solid interaction) depending on the surgical suture, model parametrization and interactions between these macroscale models and microscale lobule models.

5.3 Hybrid modeling for lung disease understanding

Besides the two new research directions above, it is natural to keep improving current models. For example, as shown in section 4.1, the respiratory and particle deposition model is not able to accurately reproduce experimental deposition results for emphysema. Therefore other factors should be taken into account to understand this disease such as enhanced deposition in the normal acinus regions compared to the diseased regions, smaller airway diameters in diseased regions compared to normal regions, airway collapse in diseased regions, and particle transport through expiration. They all may impact deposition efficiency downstream of the 3D geometry considered in that study.

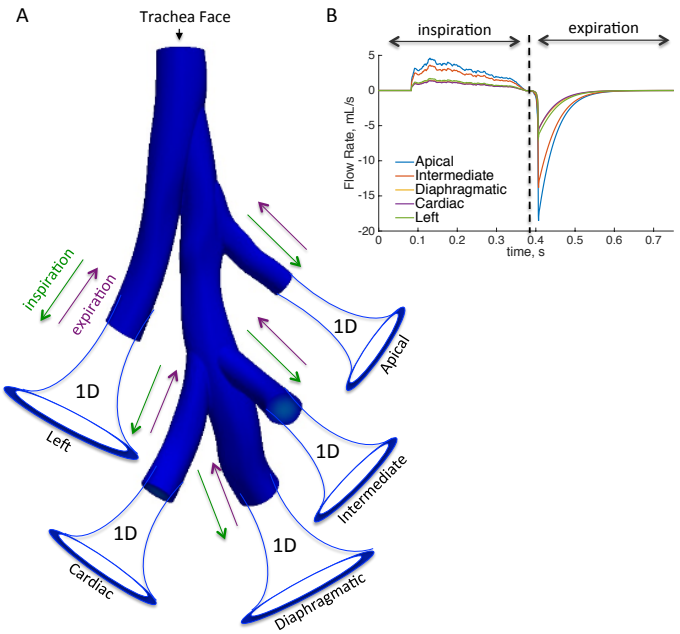

Figure 5.2: 3D-1D respiratory and particle coupling illustration between the 3D image-based airways and 1D trumpet models (panel A). Panel B shows the flow rate of each lobe at the coupling interface [15].

In a new collaboration, we are studying the effects of emphysema particular air dynamics on particle transport in acini models [50]. In addition, with Céline Grandmont (INRIA), Jessica Oakes and Shawn Shadden (U. of California, Berkeley), we are expanding the model by coupling the existing 3D main airways to the 1D airflow and particle transport *trumpet* model for the distal airways and alveoli [Taulbee and Yu, 1975, Martin and Maury, 2013]. Its name comes from the representation of the distal geometry as a single pipe of increasing area. This enables simulation of expiration for the particle model and a better differentiation of lobar morphometry [Oakes et al., 2012]. These developments present interesting modeling (for particle loss modeling and overall parametrization) and numerical coupling issues (fig. 5.2). Improving ventilation reduced model in health and chronic obstructive disease is also important for therapeutics treatments (anrt thesis of Nicolas Pozin with AIR LIQUIDE SANTE INTERNATIONAL, coadvised with Céline Grandmont).

5.4 Validation and uncertainty quantification

Other remaining challenges are validation and uncertainty quantification. Validation of codes with in-vitro data [Ku et al., 2005, Passerini et al., 2013] is a first important step. But validation of in-vivo conditions is another challenge [Ku et al., 2002]. In every applied project, we have tried to validate the simulation results [3, 18, 19], but often rather qualitatively [13, 26]. This is because either the animal experiments had been carried out before we were contacted for the modeling work, or the clinically indicated patient measurements are taken only preoperatively or not immediately postoperatively.

Since model parametrization is based on data (section 4), sensitivity of the results to these hemodynamics or respiratory input data is an important validation step. However little work has been done in this area, apart from inflow studies (on pulsatility or velocity profiles - e.g. [14]). In [Pennati et al., 2011] the location of the pressure measurement and the downstream capacitances is varied when constructing the two pulmonary boundary conditions

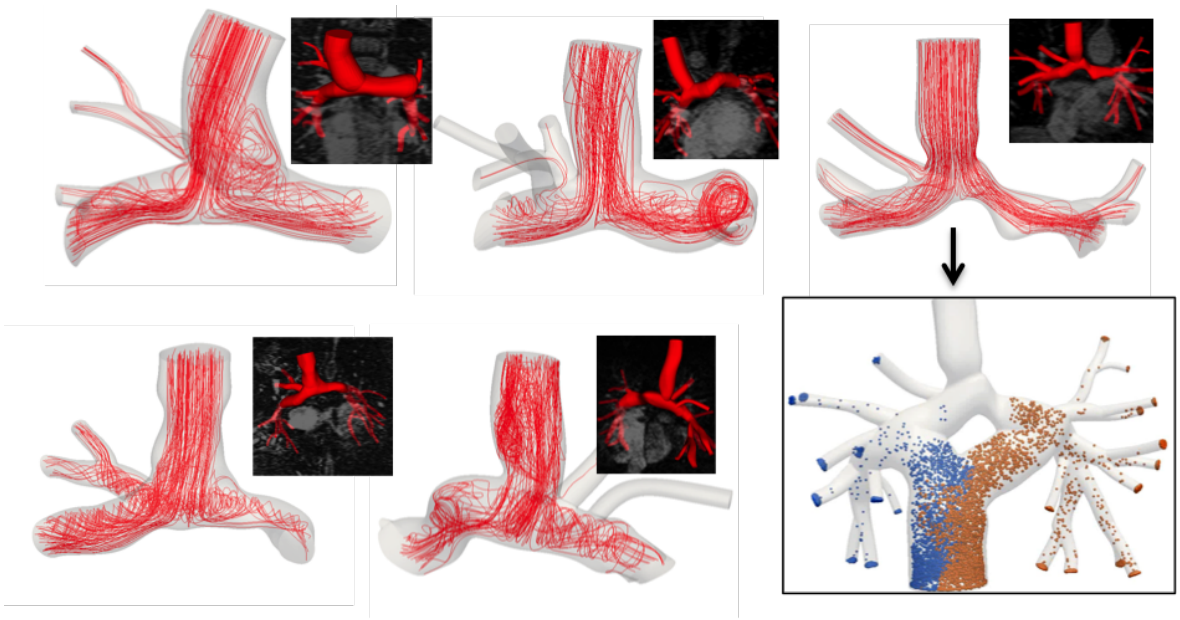

Figure 5.3: For the five patients, streamline representation of the flow at peak deceleration zoomed at the anastomosis and the full Glenn models used for simulations. Flow splits to the right lung are from left to right [0.6 0.5 0.6 0.8 0.7]. Lower right: example of Fontan virtual Y-design with particles assessing hepatic factors distribution to the left and right lungs.

of a patient-specific Glenn case, without much influence on the resulting resistance of the pulmonary arteries and pulmonary flow waveforms, respectively. In [23], the sensitivity of patient-specific simulations to hemodynamics input data is systematically investigated: with only small variations of input parameters, some output indicators (such as power loss or wall shear stress) vary non-negligibly. Power efficiency is found to be an indicator more sensitive than power loss to pressure uncertainties. However, power loss is less sensitive to the power law relating cross-sectional area of a branch and its mean flow rate than to flow split variation between right and left lungs. To lower output uncertainties, more precision in the flow split acquisition would thus be expected to be more important than to further refine the repartition of flow in the smaller branches. The study suggests that $\pm 10\%$ flow split imprecision seems reasonable in terms of patient comparison but that the patient-specific flow split should be used (fig. 5.3). This sensitivity to the flow split is thus investigated when comparing the different virtual surgical designs of these patients, with the 'Y' shape often less sensitive to this parameter [5]. Sensitivities of the results to rest versus exercise conditions, or with respiration effects are other examples of robustness tests [14, 24, 5, 36, 48].

To go further in sensitivity analysis to input data, in [51] we propose a methodology for full propagation of uncertainty from clinical data to model results that, unlike deterministic simulation, enables estimation of the confidence associated with model predictions. We illustrate this problem in patient D of section 4.2, for which coherence of simulations and clinical data indicated that the flow split to the right lung was highly uncertain. We want assess here how such uncertainty translates into surgical planning of removing the stenosis or not. First, probability density functions (PDFs) of right pulmonary artery flow split ratio and average pulmonary pressure are determined from clinical measurements, complemented by literature data. Starting from a 0D model semi-empirical approximation, Bayesian parameter estimation is used to find the distributions of boundary conditions that produce the expected PA flow split and average pressure PDFs as pre-operative model results. Second, uncertainties in the boundary conditions are propagated to simulation predictions. Sparse grid stochas-

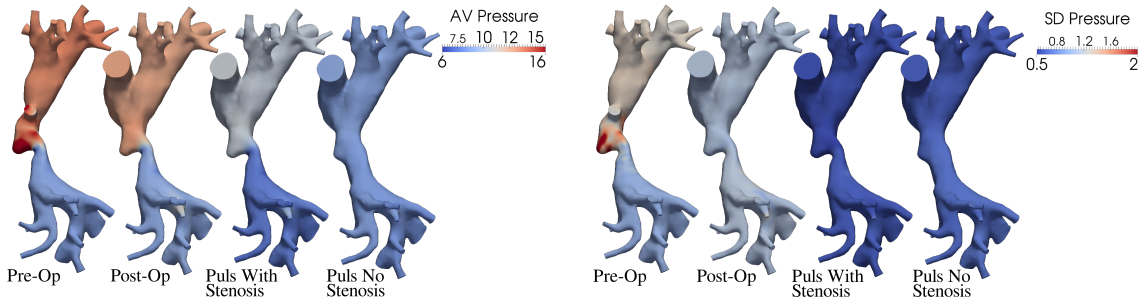

Figure 5.4: Average (left) and standard deviation (right) local pressure resulting from propagation of preoperative hemodynamics measured data uncertainty. 4 cases: preoperative model, simplified postoperative model, postoperative models with and without stenosis. Contours are limited to 16.0 and 2.0mmHg for maximum average (AV) pressure and standard deviation (SD), respectively.

tic collocation is employed to statistically characterize model predictions of post-operative hemodynamics in models with and without PA stenosis. The results quantify the statistical variability in virtual surgery predictions, allowing for placement of confidence intervals on simulation outputs (fig. 5.4).

This improved perspective on cardiovascular simulation results is achieved however at the expense of an increase in the overall computational cost. Yet, to the best of our knowledge, this study is the first to quantify the uncertainty in virtual surgery predictions directly from estimates of uncertainty in patient-specific clinical data and proposes a new paradigm of presenting cardiovascular simulation results that we hope will challenge the common practice of providing only deterministic results.

5.5 Conclusion

The outlook points above follow a research direction in line with my core research as well as novel research areas, with practical medical interest, and where there is much to explore from modeling and numerical standpoints. My PhD set the path for an important part of my research since then. Coupling of 3D Navier-Stokes equations with more extended reduced models of the circulation improved patient-specific surgical planning and device design capabilities for several congenital heart diseases. Understanding and treating numerical instabilities have also been key in this process. Highly motivated by application to medicine, I have developed strategies to parametrize models, depending on the pressure and flow data that were acquired for a given patient diagnosis. All these aspects were instrumental to extend my research to respiration. But in both blood and respiratory diseases, although the fluid mechanics understanding of these different conditions has improved, real contributions for patient care are still scarce. Therefore, in the next years, I hope I will bring my stone towards this goal.

References of the author

[1] Janice J. Yeung, Hyun Jin Kim, Thomas A. Abbruzzese, Irene E. Vignon-Clementel, Mary T. Draney-Blomme, Kay K. Yeung, Inder Perkash, Robert J. Herfkens, Charles A. Taylor, and Ronald L. Dalman. Aortoiliac hemodynamic and morphologic adaptation to chronic spinal cord injury. Journal of Vascular Surgery, 44(6):1254–1265, 2006.

[2] Jr. LaDisa, John F., Ronak J. Dholakia, C. Alberto Figueroa, Irene E. Vignon-Clementel, Frandics P. Chan, Margaret M. Samyn, Joseph R. Cava, Charles A. Taylor, and Jeffrey A. Feinstein. Computational simulations demonstrate altered wall shear stress in aortic coarctation patients treated by resection with end-to-end anastomosis. Congenital Heart Disease, 6(5):432–443, 2011.

[3] Irene E Vignon-Clementel, Alison L Marsden, and Jeffrey A Feinstein. A primer on computational simulation in congenital heart disease for the clinician. Progress in Pediatric Cardiology, 30(1):3–13, 2010.

[4] C Corsini, C Baker, E Kung, S Schievano, G Arbia, A Baretta, G Biglino, F Migliavacca, G Dubini, G Pennati, A Marsden, I Vignon-Clementel, A Taylor, TY Hsia, A Dorfman, and Modeling Congenital Hearts. An integrated approach to patient-specific predictive modeling for single ventricle heart palliation. 17:1572–1589, 2014.

[5] Weiguang Yang, Irene E. Vignon-Clementel, Guillaume Troianowski, V. Mohan Reddy, Jeffrey A. Feinstein, and Alison L. Marsden. Hepatic blood flow distribution and performance in conventional and novel Y-graft Fontan geometries: a case series computational fluid dynamics study. Journal of Thoracic and Cardiovascular Surgery, 143(5):1086–1097, 2012.

[6] Weiguang Yang, Jeffrey A. Feinstein, Shawn C. Shadden, Irene E. Vignon-Clementel, and Alison L. Marsden. Optimization of a Y-Graft design for improved hepatic flow distribution in the Fontan circulation. Journal of Biomechanical Engineering-Transactions of the Asme, 135(1), 2013.

[7] Alfonso Caiazzo, Romain Guibert, Younes Boudjemline, and Irene E Vignon-Clementel. Blood flow simulations for the design of stented valve reducer in enlarged ventricular outflow tracts. Cardiovascular Engineering and Technology, pages 1–16, 2015.

[8] Dirk Drasdo, Nick Jagiella, Ignacio Ramis-Conde, Irene E Vignon-Clementel, and William Weens. Modeling Steps from a Begnin Tumor to an Invasive Cancer: Examples of Instrinsically Multiscale Problems, pages 379–416. Taylor & Francis, 2010.

[9] G Arbia, C Corsini, ME Moghadam, AL Marsden, F Migliavacca, G Pennati, TY Hsia, IE Vignon-Clementel, and Modeling Congenital Hearts Allianc. Numerical blood flow simulation in surgical corrections: what do we need for an accurate analysis? Journal of Surgical Research, 186:44–55, 2014.

[10] IE Vignon-Clementel. A Coupled Multidomain Method for Computational Modeling of Blood Flow. PhD thesis, Stanford, 2006.

[11] I. E. Vignon-Clementel, C. Alberto Figueroa, Kenneth E. Jansen, and C. A Taylor. Outflow boundary conditions for three-dimensional finite element modeling of blood flow and pressure in arteries. 195:3776–3796, 2006.

[12] C. A. Figueroa, I. E. Vignon-Clementel, K. E. Jansen, T. J. R. Hughes, and C. A. Taylor. A coupled momentum method for modeling blood flow in three-dimensional deformable arteries. Computer Methods in Applied Mechanics and Engineering, 195(41-43):5685–5706, 2006.

[13] I. E. Vignon-Clementel, C. A. Figueroa, K. E. Jansen, and C. A. Taylor. Outflow boundary conditions for 3d simulations of non-periodic blood flow and pressure fields in deformable arteries. 13:625–640, 2010.

[14] AL Marsden, IE Vignon-Clementel, FP Chan, JA Feinstein, and CA Taylor. Effects of exercise and respiration on hemodynamic efficiency in CFD simulations of the total cavopulmonary connection. Annals of Biomedical Engineering, 35:250–263, 2007.

[15] Jessica Oakes, Alison Marsden, L., Celine Grandmont, Shawn Shadden, C., Chantal Darquenne, and Irene Vignon-Clementel. Airflow and Particle Deposition Simulations in Health and Emphysema: From In Vivo to In Silico Animal Experiments. Annals of Biomedical Engineering, 42(4):899–914, April 2014.

[16] G Arbia, I.E. Vignon-Clementel, T.Y. Hsia, and J.F. Gerbeau. Modified Navier-Stokes equations for the outflow boundary conditions in hemodynamics. under revision, 2015.

[17] Sanjay Pant, Benoit Fabrèges, Jean-Frédéric Gerbeau, and IreneE. Vignon-Clementel. A multiscale filtering-based parameter estimation method for patient-specific coarctation simulations in rest and exercise. In Oscar Camara, Tommaso Mansi, Mihaela Pop, Kawal Rhode, Maxime Sermesant, and Alistair Young, editors, Statistical Atlases and Computational Models of the Heart. Imaging and Modelling Challenges, volume 8330 of Lecture Notes in Computer Science, pages 102–109. Springer Berlin Heidelberg, 2014.

[18] JM Oakes, AL Marsden, C Grandmont, C Darquenne, and IE Vignon-Clementel. Distribution of aerosolized particles in healthy and emphysematous rat lungs: Comparison between experimental and numerical studies. Journal of Biomechanics, 48:1147–1157, 2015.

[19] Gregory Arbia, Chiara Corsini, Catriona Baker, Giancarlo Pennati, Tain-Yen Hsia, Irene E Vignon-Clementel, and for MOCHA. Pulmonary hemodynamics simulations before stage 2 single ventricle surgery: patient-specific parameter identification and clinical data assessment. Cardiovascular Engineering and Technology, 2015.

[20] S Pant, B Fabreges, JF Gerbeau, and IE Vignon-Clementel. A methodological paradigm for patient-specific multi-scale CFD simulations: from clinical measurements to parameter estimates for individual analysis. 30:1614–1648, 2014.

[21] I. Vignon and C. A. Taylor. Outflow boundary conditions for one-dimensional finite element modeling of blood flow and pressure waves in arteries. 39:361–374, 2004.

[22] R. Raghu, I. E. Vignon-Clementel, C. A. Figueroa, and C. A. Taylor. Comparative study of viscoelastic arterial wall models in nonlinear one-dimensional finite element simulations of blood flow. J Biomech Eng, 133:081003, 2011.

[23] Guillaume Troianowski, Charles A Taylor, Jeffrey A Feinstein, and Irene E Vignon-Clementel. Three-dimensional simulations in glenn patients: clinically based boundary conditions, hemodynamic results and sensitivity to input data. Journal of Biomechanical Engineering, 133:111006, 2011.

[24] A Baretta, C Corsini, W Yang, IE Vignon-Clementel, AL Marsden, JA Feinstein, TY Hsia, G Dubini, F Migliavacca, G Pennati, and Modeling Congenital Hearts Allianc. Virtual surgeries in patients with congenital heart disease: a multi-scale modelling test case. Philosophical Transactions of the Royal Society a-Mathematical Physical and Engineering Sciences, 369:4316–4330, 2011.

[25] Mahdi Esmaily Moghadam, Francesco Migliavacca, Irene E. Vignon-Clementel, Tain-Yen Hsia, Alison L. Marsden, and Allianc Modeling Congenital Hearts. Optimization of shunt placement for the norwood surgery using multi-domain modeling. Journal of Biomechanical Engineering-Transactions of the Asme, 134(5), 2012.

[26] Sanjay Pant, Chiara Corsini, Catriona Baker, Tain-Yen Hsia, Giancarlo Pennati, Irene E Vignon-Clementel, and for MOCHA. Data assimilation and modelling of patient-specific single-ventricle physiology with and without valve regurgitation. Journal of Biomechanics, in press.

[27] John F. LaDisa, C. Alberto Figueroa, Irene E. Vignon-Clementel, Hyun Jin Kim, Nan Xiao, Laura M. Ellwein, Frandics P. Chan, Jeffrey A. Feinstein, and Charles A. Taylor. Computational Simulations for Aortic Coarctation: Representative Results From a Sampling of Patients. Journal of Biomechanical Engineering, 133:091008, 2011.

[28] D. Chapelle, J. F. Gerbeau, J. Sainte-Marie, and I. Vignon-Clementel. A poroelastic model valid in large strains with applications to perfusion in cardiac modeling. Computational Mechanics, 46:91–101, 2010.

[29] J. P. Latere, I. Vignon-Clementel, K. Nissen, J. F. Gerbeau, and C. Homsy. Injection of cells into the heart: a comprehensive model to increase retention. 104:78D–78D, 2009.

[30] Jean-Pierre Latere, Christian Homsy, Jean-Frederic Gerbeau, and Irene Vignon-Clementel. Myocardial delivery of cells to the heart: A comprehensive model to increase retention. 57:E208–E208, 2011.

[31] N Jagiella, B Mueller, M Mueller, I Vignon-Clementel, and D Drasdo. Inferring growth control mechanisms in growing multi-cellular spheroids of nsclc cells from spatial-temporal image data. PLoS Comput Biol, in press.

[32] Min Tang, Nicolas Vauchelet, Ibrahim Cheddadi, Irene Vignon-Clementel, Dirk Drasdo, and Benoît Perthame. Composite waves for a cell population system modeling tumor growth and invasion. Chinese Annals of Mathematics, Series B, 34(2):295–318, 2013.

[33] M. Esmaily Moghadam, I. E. Vignon-Clementel, R. Figliola, and A. L. Marsden. A modular numerical method for implicit 0D/3D coupling in cardiovascular finite element simulations. Journal of Computational Physics, 244:63–79, 2013.

[34] Mahdi Esmaily Moghadam, ME, Y Bazilevs, T-Y Hsia, IE Vignon-Clementel, AL Marsden, and Allianc Modeling Congenital Hearts. A comparison of outlet boundary treatments for prevention of backflow divergence with relevance to blood flow simulations. Computational Mechanics, 48:277–291, 2011.

[35] H. J. Kim, I. E. Vignon-Clementel, C. A. Figueroa, K. E. Jansen, and C. A. Taylor. Developing computational methods for three-dimensional finite element simulations of coronary blood flow. Finite Elements in Analysis and Design, 46(6):514–525, 2010.

[36] A Baretta, C Corsini, AL Marsden, IE Vignon-Clementel, TY Hsia, G Dubini, F Migliavacca, G Pennati, and MOCHA. Respiratory effects on hemodynamics in patient-specific CFD models of the Fontan circulation under exercise conditions. European Journal of Mechanics B-Fluids, 35:61–69, 2012.

[37] H.J. Kim, I.E. Vignon-Clementel, C.A. Figueroa, J.F. LaDisa, K.E. Jansen, J.A. Feinstein, and C.A. Taylor. On coupling a lumped parameter heart model and a three-dimensional finite element aorta model. Annals of Biomedical Engineering, 37(11):2153–2169, 2009.

[38] H. J. Kim, I. E. Vignon-Clementel, J. S. Coogan, C. A. Figueroa, K. E. Jansen, and C. A. Taylor. Patient-specific modeling of blood flow and pressure in human coronary arteries. Annals of Biomedical Engineering, 38(10):3195–3209, 2010.

[39] E. Kung, A. Baretta, C. Baker, G. Arbia, G. Biglino, C. Corsini, S. Schievano, I. E. Vignon-Clementel, G. Dubini, G. Pennati, A. Taylor, A. Dorfman, A. M. Hlavacek, A. L. Marsden, T.-Y. Hsia, and F. Migliavacca. Predictive modeling of the virtual Hemi-Fontan operation for second stage single ventricle palliation: two patient-specific cases. Journal of Biomechanics, 46(2):423–9, January 2013.

[40] C Corsini, C Baker, A Baretta, G Biglino, AM Hlavacek, TY Hsia, E Kung, A Marsden, F Migliavacca, I Vignon-Clementel, G Pennati, and Modeling Congenital Hearts. Integration of clinical data collected at different times for virtual surgery in single ventricle patients: A case study. 43:1310–1320, 2015.

[41] H. J. Kim, C. A. Figueroa, T. J. R. Hughes, K. E. Jansen, and C. A. Taylor. Augmented lagrangian method for constraining the shape of velocity profiles at outlet boundaries for three-dimensional finite element simulations of blood flow. Computer Methods in Applied Mechanics and Engineering, 198(45-46):3551–3566, 2009.

[42] ME Moghadam, F Migliavacca, IE Vignon-Clementel, TY Hsia, AL Marsden, and Modeling Congenital Hearts Allianc. Optimization of shunt placement for the norwood surgery using multi-domain modeling. 134, 2012.

[43] Alessia Baretta. Patient-specific modeling of the cardiovascular system for surgical planning of single-ventricle defects. PhD thesis, Politecnico di Milano, Milan, Italy, 2014.

[44] Gregory Arbia. Multiscale modeling of blood flow in the context Multiscale modeling of blood flow in the context of congenital heart disease. PhD thesis, UPMC Université Paris 6, Ecole doctorale de mathématiques de Paris Centre, 2014.

[45] Sanjay Gregory Pant, Chiara Corsini, Tain-Yen Hsia, Giancarlo Pennati, and Irene E Vignon-Clementel. Data assimilation for parameter estimation in a single-ventricle heart model. 2015.

[46] Sanjay Pant, Chiara Corsini, Catriona Baker, Tain-Yen Hsia, Giancarlo Pennati, Irene E Vignon-Clementel, and for MOCHA. Inverse problems in hemodynamics: consideration of heart-rate variability. in preparation, 2015.

[47] Kristin McLeod, Alfonso Caiazzo, Miguel A. Fernandez, Tommaso Mansi, Irene E. Vignon-Clementel, Maxime Sermesant, Xavier Pennec, Younes Boudjemline, and Jean-Frederic Gerbeau. Lecture Notes in Computer Science, volume 6364, pages 95–104. 2010.

[48] Romain Guibert, Kristin Mcleod, Alfonso Caiazzo, Tommaso Mansi, Miguel Ángel Fernández, Maxime Sermesant, Xavier Pennec, Irene Vignon-Clementel, Younes Boudjemline, and Jean-Frédéric Gerbeau. Group-wise Construction of Reduced Models for Understanding and Characterization of Pulmonary Blood Flows from Medical Images. Medical Image Analysis, 18(1):63–82, October 2013.

[49] Nick Jagiella. Parameterization of lattice-based tumor models from data. PhD thesis, Mathématiques Appliquées, Université Pierre et Marie Curie - Paris VI, 2012.

[50] JM Oakes, Ph Hofemeier, IE Vignon-Clementel, and J Sznitman. Aerosols in healthy and emphysematous in silico pulmonary acinar rat models. Journal of Biomechanics, accepted.

[51] DE Schiavazzi, G Arbia, C Baker, AM Hlavacek, TY Hsia, AL Marsden, IE Vignon-Clementel, et al. Uncertainty quantification in virtual surgery hemodynamics predictions for single ventricle palliation. International journal for numerical methods in biomedical engineering, 2015.

Other references

[cha,] 2nd CFD Challenge Predicting Patient-Specific Hemodynamics at Rest and Stress through an Aortic Coarctation, 2013.

[fel,] FELiScE: Finite Elements for LIfe SCiences and Engineering.

[euR, 2015] (2015). Medical devices text now includes modelling and simulation.

[sim, 2015] (2015). Simvascular.

[Abaci et al., 2014] Abaci, H. E., Shen, Y.-I., Tan, S., and Gerecht, S. (2014). Recapitulating physiological and pathological shear stress and oxygen to model vasculature in health and disease. Scientific reports, 4.

[Agu and Ugwoke, 2011] Agu, R. U. and Ugwoke, M. I. (2011). In vitro and in vivo testing methods for respiratory drug delivery. Expert Opinion on Drug Delivery, 8:57–69.

[Alarcón et al., 2005] Alarcón, T., Byrne, H. M., and Maini, P. K. (2005). A multiple scale model for tumor growth. Multiscale Model. Simul., 3(2):440–475 (electronic).

[Almeida and Spilker, 1998] Almeida, E. and Spilker, R. (1998). Finite element formulations for hyperelastic transversely isotropic biphasic soft tissues. Computer Methods in Applied Mechanics and Engineering, 151(3-4):513–538.

[Ambrosi and Mollica, 2002] Ambrosi, D. and Mollica, F. (2002). On the mechanics of a growing tumor. Ing. J. Eng. Sci., 40(12):1297–1316.

[Anderson et al., 2007] Anderson, A., Chaplain, M., and (editors), K. R. (2007). Single-Cell-Based Models in Biology and Medicine. Birkhäuse, Basel.

[Anjilvel and Asgharian, 1995] Anjilvel, S. and Asgharian, B. (1995). A multiple path model of particle deposition in the rat lung. Fundamental and Applied Toxiocology, 28:41–50.

[Anliker et al., 1971] Anliker, M., Rockwell, L., and Ogden, E. (1971). Nonlinear analysis of flow pulses and shock waves in arteries. ZAMP, 22:217–246.

[Arts et al., 1991] Arts, T., Bovendeerd, P., Prinzen, F. W., and Reneman, R. S. (1991). Relation between left ventricular cavity pressure and volume and systolic fiber stress and strain in the wall. Biophysical journal, 59(1):93–102.

[Asgharian et al., 2006] Asgharian, B., Price, O. T., and Hofmann, W. (2006). Prediction of particle deposition in the human lung using realistic models of lung ventilation. Journal of Aerosol Science, 37(10):1209–1221.

[Ashikaga et al., 2008] Ashikaga, H., Coppola, B. A., Yamazaki, K. G., Villarreal, F. J., Omens, J. H., and Covell, J. W. (2008). Changes in regional myocardial volume during the cardiac cycle: implications for transmural blood flow and cardiac structure. Am J Physiol Heart Circ Physiol, 295(2):H610–618.

[Auricchio et al., 2014] Auricchio, F., Conti, M., Lefieux, A., Morganti, S., Reali, A., Sardanelli, F., Secchi, F., Trimarchi, S., and Veneziani, A. (2014). Patient-specific analysis of post-operative aortic hemodynamics: a focus on thoracic endovascular repair (tevar). Computational Mechanics, 54(4):943–953.

[Badia et al., 2009] Badia, S., Quaini, A., and Quarteroni, A. (2009). Coupling Biot and Navier–Stokes equations for modelling fluid–poroelastic media interaction. Journal of Computational Physics, 228(21):7986–8014.

[Baffico et al., 2010] Baffico, L., Grandmont, C., and Maury, B. (2010). Multiscale Modeling of the Respiratory Tract. Mathematical Models and Methods in Applied Sciences, 20(01):59.

[Bai et al., 2007] Bai, P., Banks, H. T., Dediu, S., Govan, A. Y., Last, M., Lloyd, A. L., Nguyen, H. K., Olufsen, M. S., Rempala, G., and Slenning, B. D. (2007). Stochastic and deterministic models for agricultural production networks. Mathematical biosciences and engineering, 4(3):373–402.

[Barnard et al., 1966] Barnard, A. C. L., Hunt, W. A., Timlake, W. P., and Varley, E. (1966). A theory of fluid flow in compliant tubes. Biophysical Journal, 6(6):717–724.

[Bartha and Rieger, 2006] Bartha, K. and Rieger, H. (2006). Vascular network remodeling via vessel cooption, regression and growth in tumors. J. Theor. Biol., page 16.

[Bates, 2009] Bates, J. H. (2009). Lung mechanics: an inverse modeling approach. Cambridge University Press.

[Bates and Suki, 2008] Bates, J. H. T. and Suki, B. (2008). Assessment of peripheral lung mechanics. Respiratory Physiology & Neurobiology, 163(1-3):54–63.

[Bazilevs et al., 2009a] Bazilevs, Y., Gohean, J. R., Hughes, T. J. R., Moser, R. D., and Zhang, Y. (2009a). Patient-specific isogeometric fluid–structure interaction analysis of thoracic aortic blood flow due to implantation of the Jarvik 2000 left ventricular assist device. Computer Methods in Applied Mechanics and Engineering, 198(45):3534–3550.

[Bazilevs et al., 2009b] Bazilevs, Y., Gohean, J. R., Hughes, T. J. R., Moser, R. D., and Zhang, Y. (2009b). Patient-specific isogeometric fluid-structure interaction analysis of thoracic aortic blood flow due to implantation of the jarvik 2000 left ventricular assist device. Computer Methods in Applied Mechanics and Engineering, 198(45-46):3534–3550.

[Begue et al., 1988] Begue, C., Conca, C., Murat, F., and Pironneau, O. (1988). Les équations de Stokes et de Navier-Stokes avec des conditions aux limites sur la pression. Seminaire College de France.

[Berger et al., 2015] Berger, L., Bordas, R., Burrowes, K., Grau, V., Tavener, S., and Kay, D. (2015). A poroelastic model coupled to a fluid network with applications in lung modelling. International journal for numerical methods in biomedical engineering.

[Bergers and Benjamin, 2003] Bergers, G. and Benjamin, L. E. (2003). Tumorigenesis and the angiogenic switch. Nat. Rev. Cancer, 3(6):401–10.

[Berne and Levy, 2001] Berne, R. and Levy, M. (2001). Cardiovascular Physiology. St Louis, Mosby.

[Bertagna and Veneziani, 2014] Bertagna, L. and Veneziani, A. (2014). A model reduction approach for the variational estimation of vascular compliance by solving an inverse fluid–structure interaction problem. Inverse Problems, 30(5):055006.

[Bertoglio et al., 2014] Bertoglio, C., Barber, D., Gaddum, N., Valverde, I., Rutten, M., Beerbaum, P., Moireau, P., Hose, R., and Gerbeau, J.-F. (2014). Identification of artery wall stiffness: In vitro validation and in vivo results of a data assimilation procedure applied to a 3D fluid-structure interaction model. Journal of Biomechanics, 47(5):1027–1034.

[Bertoglio and Caiazzo, 2014] Bertoglio, C. and Caiazzo, A. (2014). A tangential regularization method for backflow stabilization in hemodynamics. Journal of Computational Physics, 261:162–171.

[Bertoglio et al., 2013] Bertoglio, C., Caiazzo, A., and Fernández, M. A. (2013). Fractional-step schemes for the coupling of distributed and lumped models in hemodynamics. SIAM Journal on Scientific Computing, 35(3):B551–B575.

[Bertoglio et al., 2012] Bertoglio, C., Moireau, P., and Gerbeau, J.-F. (2012). Sequential parameter estimation for fluid–structure problems: Application to hemodynamics. International Journal for Numerical Methods in Biomedical Engineering, 28(4):434–455.

[Biot, 1956] Biot, M. A. (1956). Theory of propagation of elastic waves in a fluid-saturated porous solid. II higher frequency range. J. Acoust. Soc. Am., 28:179–191.

[Biot, 1972] Biot, M. A. (1972). Theory of finite deformations of porous solids. Indiana Univ. Math. J., 21:597–620.

[Blanco et al., 2007] Blanco, P., Feijóo, R., and Urquiza, S. (2007). A unified variational approach for coupling 3d-1d models and its blood flow applications. Computer Methods in Applied Mechanics and Engineering, 196(41-44):4391 – 4410.

[Blanco et al., 2013] Blanco, P. J., Deparis, S., and Malossi, A. C. I. (2013). On the continuity of mean total normal stress in geometrical multiscale cardiovascular problems. Journal of Computational Physics, 251(0):136–155.

[Blanco and Feijoo, 2013] Blanco, P. J. and Feijoo, R. A. (2013). A dimensionally-heterogeneous closed-loop model for the cardiovascular system and its applications. Medical Engineering and Physics, 35(5):652–667.

[Bode et al., 2012] Bode, A. S., Huberts, W., Bosboom, E. M. H., Kroon, W., van der Linden, W. P. M., Planken, R. N., van de Vosse, F. N., and Tordoir, J. H. M. (2012). Patient-specific computational modeling of upper extremity arteriovenous fistula creation: Its feasibility to support clinical decision-making. PLoS ONE, 7(4):e34491 EP –.

[Boileau et al., 2015] Boileau, E., Nithiarasu, P., Blanco, P. J., Müller, L. O., Fossan, F. E., Hellevik, L. R., Donders, W. P., Huberts, W., Willemet, M., and Alastruey, J. (2015). A benchmark study of numerical schemes for one-dimensional arterial blood flow modelling. International journal for numerical methods in biomedical engineering.

[Borazjani et al., 2010] Borazjani, I., Ge, L., and Sotiropoulos, F. (2010). High-resolution fluid–structure interaction simulations of flow through a bi-leaflet mechanical heart valve in an anatomic aorta. Annals of Biomedical Engineering, 38:326–344.

[Borja, 2006] Borja, R. (2006). On the mechanical energy and effective stress in saturated and unsaturated porous continua. International Journal of Solids and Structures, 43(6):1764–1786.

[Boselli et al., 2015] Boselli, F., Freund, J. B., and Vermot, J. (2015). Blood flow mechanics in cardiovascular development. Cellular and Molecular Life Sciences, pages 1–15.

[Boulakia et al., 2013] Boulakia, M., Egloffe, A.-C., and Grandmont, C. (2013). Stability estimates for the unique continuation property of the stokes system. application to an inverse problem. Inverse Problems.

[Bove et al., 2003] Bove, E. L., de Leval, M. R., Migliavacca, F., Guadagni, G., and Dubini, G. (2003). Computational fluid dynamics in the evaluation of hemodynamic performance of cavopulmonary connections after the norwood procedure for hypoplastic left heart syndrome. The Journal of Thoracic and Cardiovascular Surgery, 126(4):1040 – 1047.

[Bradley et al., 2011] Bradley, C., Bowery, A., Britten, R., Budelmann, V., Camara, O., Christie, R., Cookson, A., Frangi, A. F., Gamage, T. B., Heidlauf, T., et al. (2011). Opencmiss: a multi-physics & multi-scale computational infrastructure for the vph/physiome project. Progress in biophysics and molecular biology, 107(1):32–47.

[Brand et al., 2009] Brand, P., Schulte, M., Wencker, M., Herpich, C. H., Klein, G., Hanna, K., and Meyer, T. (2009). Lung deposition of inhaled alpha1-proteinase inhibitor in cystic fibrosis and alpha1-antitrypsin deficiency. The European Respiratory Journal, 34:354–60.

[Bruneau and Fabrie, 1994] Bruneau, C.-H. and Fabrie, P. (1994). Effective downstream boundary conditions for incompressible Navier–Stokes equations. International Journal for Numerical Methods in Fluids, 19(8):693–705.

[Bruneau and Fabrie, 1996] Bruneau, C.-H. and Fabrie, P. (1996). New efficient boundary conditions for incompressible Navier–Stokes equations: a well-posedness result. RAIRO-Modélisation mathématique et analyse numérique, 30(7):815–840.

[Butler and Tsuda, 2005] Butler, J. P. and Tsuda, A. (2005). Logistic trajectory maps and aerosol mixing due to asynchronous flow at airway bifurcations. Respiratory physiology & neurobiology, 148(1):195–206.

[Byrne and Drasdo, 2009] Byrne, H. and Drasdo, D. (2009). Individual-based and continuum models of growing cell populations: A comparison. J Math Biol, 58(4-5):657–87.

[Byrne and Preziosi, 2003] Byrne, H. and Preziosi, L. (2003). Modelling solid tumour growth using the theory of mixtures. Mathem. Medicine and Biology, 20:341 – 366.

[Calo et al., 2008] Calo, V., Brasher, N., Bazilevs, Y., and Hughes, T. (2008). Multiphysics model for blood flow and drug transport with application to patient-specific coronary artery flow. Comput. Mech., 43(1):161–177.

[Camara et al., 2014] Camara, O., Mansi, T., Pop, M., Rhode, K., Sermesant, M., and Young, A., editors (2014). Statistical Atlases and Computational Models of the Heart. Imaging and Modelling Challenges, volume 8330 of Lecture Notes in Computer Science. Springer Berlin Heidelberg.

[Canić, 2002] Canić, S. (2002). Blood flow through compliant vessels after endovascular repair: wall deformations induced by the discontinuous wall properties. Computing and visualization in science, 4(3):147–155.

[Capasso and Morale, 2009] Capasso, V. and Morale, D. (2009). Stochastic modelling of tumour-induced angiogenesis. J Math Biol, 58(1-2):219–33.

[Caputo et al., 2013] Caputo, M., Chiastra, C., Cianciolo, C., Cutrì, E., Dubini, G., Gunn, J., Keller, B., Migliavacca, F., and Zunino, P. (2013). Simulation of oxygen transfer in stented arteries and correlation with in-stent restenosis. International journal for numerical methods in biomedical engineering, 29(12):1373–1387.

[Carmeliet, 2003] Carmeliet, P. (2003). Angiogenesis in health and disease. Nat Med, 9(6):653–60.

[Caruel et al., 2014] Caruel, M., Chabiniok, R., Moireau, P., Lecarpentier, Y., and Chapelle, D. (2014). Dimensional reductions of a cardiac model for effective validation and calibration. Biomechanics and modeling in mechanobiology, 13(4):897–914.

[Cattaneo and Zunino, 2014] Cattaneo, L. and Zunino, P. (2014). A computational model of drug delivery through microcirculation to compare different tumor treatments. International journal for numerical methods in biomedical engineering, 30(11):1347–1371.

[Cazeaux and Grandmont, 2015] Cazeaux, P. and Grandmont, C. (2015). Homogenization of a multiscale viscoelastic model with nonlocal damping, application to the human lungs. Mathematical Models and Methods in Applied Sciences, 25(06):1125–1177.

[Ceballos et al., 2012] Ceballos, A., Argueta-Morales, I. R., Divo, E., Osorio, R., Caldarone, C. A., Kassab, A. J., and Decampli, W. M. (2012). Computational analysis of hybrid norwood circulation with distal aortic arch obstruction and reverse blalock-taussig shunt. Ann Thorac Surg, 94(5):1540–50.

[Cebral et al., 2003] Cebral, J. R., Castro, M., Soto, O., Löhner, R., Yim, P. J., and Alperin, N. (2003). Finite element modeling of the circle of willis from magnetic resonance data. In Medical Imaging 2003, pages 11–21. International Society for Optics and Photonics.

[Chapelle et al., 2013] Chapelle, D., Fragu, M., Mallet, V., and Moireau, P. (2013). Fundamental principles of data assimilation underlying the Verdandi library: applications to biophysical model personalization within euHeart. Medical & Biological Engineering & Computing, pages 1–13.

[Chapelle and Moireau, 2014] Chapelle, D. and Moireau, P. (2014). General coupling of porous flows and hyperelastic formulations—from thermodynamics principles to energy balance and compatible time schemes. European Journal of Mechanics-B/Fluids, 46:82–96.

[Ciarlet and Geymonat, 1982] Ciarlet, P. G. and Geymonat, G. (1982). Sur les lois de comportement en élasticité non linéaire. C.R.A.S, Série II, 295:423–426.

[Cimrman and Rohan, 2003] Cimrman, R. and Rohan, E. (2003). Modelling heart tissue using a composite muscle model with blood perfusion. In Bathe, KJ, editor, Computational Fluid and Solid Mechanics, 2nd MIT Conference, pages 1642–1646.

[Comer et al., 2000] Comer, J. K., Kleinstreuer, C., Hyun, S., and Kim, C. S. (2000). Aerosol transport and deposition in sequentially bifurcating airways. Journal of Biomechanical Engineering, 122(2):152–8.

[Comerford et al., 2010] Comerford, A., Bauer, G., and Wall, W. A. (2010). Nanoparticle transport in a realistic model of the tracheobronchial region. International Journal for Numerical Methods in Biomedical Engineering, 26:904–914.

[Cookson et al., 2012] Cookson, A., Lee, J., Michler, C., Chabiniok, R., Hyde, E., Nordsletten, D., Sinclair, M., Siebes, M., and Smith, N. (2012). A novel porous mechanical framework for modelling the interaction between coronary perfusion and myocardial mechanics. Journal of biomechanics, 45(5):850–855.

[Coussy, 1995] Coussy, O. (1995). Mechanics of porous continua. Wiley, New-York.

[Curcio et al., 2004] Curcio, A., Clark, M., Zhao, M., and Ruan, W. (2004). A hyperbolic system of equations of blood flow in an arterial network. SIAM Journal on Applied Mathematics, 64(2):637–667.

[D'Angelo et al., 2011] D'Angelo, C., Zunino, P., Porpora, A., Morlacchi, S., and Migliavacca, F. (2011). Model reduction strategies enable computational analysis of controlled drug release from cardiovascular stents. SIAM Journal on Applied Mathematics, 71(6):2312–2333.

[Darquenne and Paiva, 1994] Darquenne, C. and Paiva, M. (1994). One-dimensional simulation of aerosol transport and deposition in the human lung. Journal of applied physiology, 77(6):2889–98.

[Darquenne et al., 2011] Darquenne, C., van Ertbruggen, C., and Prisk, G. K. (2011). Convective flow dominates aerosol delivery to the lung segments. Journal of Applied Physiology, 111:48–54.

[De Backer et al., 2008] De Backer, J. W., Vos, W. G., Gorl, C. D., Germonpre, P., Partoens, B., Wuyts, F. L., Parizel, P. M., and De Backer, W. (2008). Flow analyses in the lower airways : Patient-specific model and boundary conditions. Medical Engineering & Physics, 30:872–879.

[de Buhan et al., 1998] de Buhan, P., Chateau, X., and Dormieux, L. (1998). The constitutive equations of finite-strain poroelasticity in the light of a micro-macro approach. Eur. J. Mech. A/Solids, 17(6):909–922.

[De Geeter et al., 1997] De Geeter, J., Van Brussel, H., De Schutter, J., and Decréton, M. (1997). A smoothly constrained Kalman filter. Pattern Analysis and Machine Intelligence, IEEE Transactions on, 19(10):1171–1177.

[de Leval and Deanfield, 2010] de Leval, M. R. and Deanfield, J. E. (2010). Four decades of Fontan palliation. Nature Reviews Cardiology, 7(9):520–527.

[de Rochefort et al., 2007] de Rochefort, L., Vial, L., Fodil, R., Maître, X., Louis, B., Isabey, D., Caillibotte, G., Thiriet, M., Bittoun, J., Durand, E., and Sbirlea-Apiou, G. (2007). In vitro validation of computational fluid dynamic simulation in human proximal airways with hyperpolarized 3He magnetic resonance phase-contrast velocimetry. Journal of Applied Physiology, 102(5):2012–23.

[de Zelicourt et al., 2009] de Zelicourt, D., Ge, L., Wang, C., Sotiropoulos, F., Gilmanov, A., and Yoganathan, A. (2009). Flow simulations in arbitrarily complex cardiovascular anatomies - an unstructured cartesian grid approach. Computers and Fluids, 38(9):1749 – 1762.

[de Zélicourt et al., 2010] de Zélicourt, D. A., Marsden, A., Fogel, M. A., and Yoganathan, A. P. (2010). Imaging and patient-specific simulations for the Fontan surgery: Current methodologies and clinical applications. Progress in Pediatric Cardiology, 30(1):31–44.

[DeGroff, 2008] DeGroff, C. (2008). Modeling the Fontan circulation: Where we are and where we need to go. Pediatric Cardiology, 29(1):3–12.

[D'Elia et al., 2012] D'Elia, M., Perego, M., and Veneziani, A. (2012). A variational data assimilation procedure for the incompressible Navier-Stokes equations in hemodynamics. Journal of Scientific Computing, 52(2):340–359.

[DeVault et al., 2008] DeVault, K., Gremaud, P. A., Novak, V., Olufsen, M. S., Vernieres, G., and Zhao, P. (2008). Blood flow in the circle of Willis: modeling and calibration. Multiscale Modeling & Simulation, 7(2):888–909.

[Diamond and O'Donnell, 1977] Diamond, L. and O'Donnell, M. (1977). Pulmonary mechanics in normal rats. Journal of Applied, 43(6):942–8.

[Dobroserdova and Olshanskii, 2013] Dobroserdova, T. and Olshanskii, M. (2013). A finite element solver and energy stable coupling for 3d and 1d fluid models. Computer Methods in Applied Mechanics and Engineering, 259:166–176.

[Drasdo, 2003] Drasdo, D. (2003). On selected individual-based approaches to the dynamics of multicellular systems. In W. Alt, M. Griebel, J. L., editor, Multiscale modeling. Birkhäuser.

[Drasdo, 2005] Drasdo, D. (2005). Coarse graining in simulated cell populations. Adv. Complex Syst., 8(2 & 3):319–363.

[Drasdo and Hoehme, 2005] Drasdo, D. and Hoehme, S. (2005). A single-cell based model to tumor growth in-vitro: monolayers and spheroids. J. Phys. Biol., 2:133 – 147.

[Drasdo and Höhme, 2003] Drasdo, D. and Höhme, S. (2003). Individual-based approaches to birth and death in avascular tumors. Math. and Comp. Modelling, 37:1163 – 1175.

[Emami et al., 2011] Emami, K., Chia, E., Kadlecek, S., Macduffie-Woodburn, J. P., Zhu, J., Pickup, S., Blum, A., Ishii, M., and Rizi, R. R. (2011). Regional correlation of emphysematous changes in lung function and structure: a comparison between pulmonary function testing and hyperpolarized MRI metrics. Journal of Applied Physiology, 110(1):225–35.

[Essig et al., 2013] Essig, M., Shiroishi, M. S., Nguyen, T. B., Saake, M., Provenzale, J. M., Enterline, D., Anzalone, N., Dörfler, A., Rovira, À., Wintermark, M., et al. (2013). Perfusion mri: the five most frequently asked technical questions. AJR. American journal of roentgenology, 200(1):24.

[Feenstra and Taylor, 2009] Feenstra, P. and Taylor, C. (2009). Drug transport in artery walls: A sequential porohyperelastic-transport approach. Computer Methods in Biomechanics and Biomedical Engineering, 12(3):263–276.

[Fetita et al., 2005] Fetita, C., Mancini, S., Perchet, D., Prêteux, F., Thiriet, M., and Vial, L. (2005). An image-based computational model of oscillatory flow in the proximal part of tracheobronchial trees. Computer Methods in Biomechanics and Biomedical Engineering, 8(4):279–293.

[Fleury, 2012] Fleury, V. (2012). Clarifying tetrapod embryogenesis by a dorso-ventral analysis of the tissue flows during early stages of chicken development. Biosystems, 109(3):460–474.

[Formaggia et al., 2001] Formaggia, L., Gerbeau, J., Nobile, F., and Quarteroni, A. (2001). On the coupling of 3D and 1D Navier-Stokes equations for flow problems in compliant vessels. Computer Methods in Applied Mechanics and Engineering, 191(6-7):561–582.

[Formaggia et al., 2002a] Formaggia, L., Gerbeau, J. F., Nobile, F., and Quarteroni, A. (2002a). Numerical treatment of defective boundary conditions for the Navier-Stokes equations. Siam Journal on Numerical Analysis, 40(1):376–401.

[Formaggia et al., 2003] Formaggia, L., Lamponi, D., and Quarteroni, A. (2003). One-dimensional models for blood flow in arteries. Journal of engineering mathematics, 47(3-4):251–276.

[Formaggia et al., 2007] Formaggia, L., Moura, A., and Nobile, F. (2007). On the stability of the coupling of 3d and 1d fluid-structure interaction models for blood flow simulations. ESAIM: Mathematical Modelling and Numerical Analysis, 41:743–769.

[Formaggia et al., 2002b] Formaggia, L., Nobile, F., and Quarteroni, A. (2002b). A one dimensional model for blood flow: application to vascular prosthesis. Lecture Notes in Computational Science and Engineering, 19:137–154.

[Formaggia et al., 2010] Formaggia, L., Quarteroni, A., and Veneziani, A. (2010). Cardiovascular Mathematics: Modeling and simulation of the circulatory system, volume 1. Springer Science & Business Media.

[Formaggia et al., 2013] Formaggia, L., Quarteroni, A., and Vergara, C. (2013). On the physical consistency between three-dimensional and one-dimensional models in haemodynamics. Journal of Computational Physics, 244:97–112.

[Formaggia et al., 2008] Formaggia, L., Veneziani, A., and Vergara, C. (2008). A new approach to numerical solution of defective boundary valve problems in incompressible fluid dynamics. Society for Industrial and Applied Mathematics Journal on Numerical Analysis, 46(6):2769–2794.

[Fouchet-Incaux, 2014] Fouchet-Incaux, J. (2014). Artificial boundaries and formulations for the incompressible Navier–Stokes equations: applications to air and blood flows. SeMA Journal, 64(1):1–40.

[Freyer and Sutherland, 1986] Freyer, J. and Sutherland, R. (1986). Regulation of growth saturation and development of necrosis in emt6 ro multicellular spheroids by the glucose and oxygen supply. Cancer Res., 46:3504–3512.

[Fronek and Zweifach, 1975] Fronek, K. and Zweifach, B. (1975). Microvascular pressure distribution in skeletal muscle and the effect of vasodilation. Am J Physiol, 228(3):791–796.

[Gemci et al., 2008] Gemci, T., Ponyavin, V., Chen, Y., Chen, H., and Collins, R. (2008). Computational model of airflow in upper 17 generations of human respiratory tract. Journal of Biomechanics, 41(9):2047–54.

[Gerbeau et al., 2005] Gerbeau, J.-F., Vidrascu, M., and Frey, P. (2005). Fluid–structure interaction in blood flows on geometries based on medical imaging. Computers & Structures, 83(2):155–165.

[Ghista and Ng, 2007] Ghista, D. and Ng, E. (2007). Cardiac Perfusion and Pumping Engineering. World Scientific.

[Gillespie, 1977] Gillespie, D. T. (1977). Exact stochastical simulations of coupled chemical reactions. J. Phys. Chem., 81(25):2340–2361.

[Givoli, 1992] Givoli, D. (1992). Numerical methods for problems in infinite domains. Elsevier.

[Go et al., 2013] Go, A. S., Mozaffarian, D., Roger, V. L., Benjamin, E. J., Berry, J. D., Borden, W. B., Bravata, D. M., Dai, S., Ford, E. S., Fox, C. S., et al. (2013). Heart disease and stroke statistics–2013 update: a report from the american heart association. Circulation, 127(1):e6.

[Gonzalez and Bassingthwaighte, 1990] Gonzalez, F. and Bassingthwaighte, J. B. (1990). Heterogeneities in regional volumes of distribution and flows in rabbit heart. Am J Physiol Heart Circ Physiol, 258(4):H1012–1024.

[Goto et al., 1991] Goto, M., Flynn, A. E., Doucette, J. W., Jansen, C. M., Stork, M. M., Coggins, D. L., Muehrcke, D. D., Husseini, W. K., and Hoffman, J. I. (1991). Cardiac contraction affects deep myocardial vessels predominantly. Am J Physiol Heart Circ Physiol, 261(5):H1417–1429.

[Grandmont et al., 2006] Grandmont, C., Maury, B., and Meunier, N. (2006). A viscoelastic model with non-local damping application to the human lungs. ESAIM: Mathematical Modelling and Numerical Analysis-Modélisation Mathématique et Analyse Numérique, 40(1):201–224.

[Gravemeier et al., 2012] Gravemeier, V., Comerford, A., Yoshihara, L., and Ismail, M. (2012). A novel formulation for neumann inflow boundary conditions in biomechanics. International Journal for Numerical Methods in Biomedical Engineering, 28:560–573.

[Hanahan and Folkman, 1996] Hanahan, D. and Folkman, J. (1996). Patterns and emerging mechanisms of the angiogenic switch during tumorigenesis. Cell, 86(3):353–64.

[Hann et al., 2004] Hann, C., Chase, J., Shaw, G., and Smith, B. W. (2004). Identification of patient specific parameters for a minimal cardiac model. In Engineering in Medicine and Biology Society, 2004. IEMBS'04. 26th Annual International Conference of the IEEE, volume 1, pages 813–816. IEEE.

[Hann et al., 2010] Hann, C. E., Chase, J. G., Desaive, T., Froissart, C., Revie, J., Stevenson, D., Lambermont, B., Ghuysen, A., Kolh, P., and Shaw, G. M. (2010). Unique parameter identification for cardiac diagnosis in critical care using minimal data sets. Computer methods and programs in biomedicine, 99(1):75–87.

[Hann et al., 2011] Hann, C. E., Revie, J., Stevenson, D., Heldmann, S., Desaive, T., Froissart, C., Lambermont, B., Ghuysen, A., Kolh, P., Shaw, G. M., et al. (2011). Patient specific identification of the cardiac driver function in a cardiovascular system model. Computer methods and programs in biomedicine, 101(2):201–207.

[Heywood et al., 1996] Heywood, J. G., Rannacher, R., and Turek, S. (1996). Artificial boundaries and flux and pressure conditions for the incompressible Navier-Stokes equations. International Journal for Numerical Methods in Fluids, 22(5):325–352.

[Hindmarsh, 2000] Hindmarsh, A. C. (2000). The PVODE and IDA algorithms. Technical report, Technical Report UCRL-ID-141558, LLNL.

[Hindmarsh et al., 2005] Hindmarsh, A. C., Brown, P. N., Grant, K. E., Lee, S. L., Serban, R., Shumaker, D. E., and Woodward, C. S. (2005). SUNDIALS: Suite of nonlinear and differential/algebraic equation solvers. ACM Transactions on Mathematical Software (TOMS), 31(3):363–396.

[Holenstein et al., 1980] Holenstein, R., Niederer, P., and Anliker, M. (1980). A viscoelastic model for use in predicting arterial pulse waves. Journal of biomechanical engineering, 102(4):318–325.

[Horssen et al., 2009] Horssen, P., Wijngaard, J. P. H. M., Siebes, M., and Spaan, J. A. E. (2009). Improved regional myocardial perfusion measurement by means of an imaging cryomicrotome. In 4th European Conference of the International Federation for Medical and Biological Engineering, pages 771–774. Springer.

[Hughes and Lubliner, 1973] Hughes, T. J. and Lubliner, J. (1973). On the one-dimensional theory of blood flow in the larger vessels. Mathematical Biosciences, 18(1):161–170.

[Huyghe et al., 1992] Huyghe, J. M., Arts, T., van Campen, D. H., and Reneman, R. S. (1992). Porous medium finite element model of the beating left ventricle. Am J Physiol Heart Circ Physiol, 262(4):H1256–1267.

[Huyghe and van Campen, 1991a] Huyghe, J. M. and van Campen, D. H. (1991a). Finite deformation theory of hierarchically arranged porous solids: I. Balance of mass and momentum. Int. J. Engng Sci., 33(13):1861–1871.

[Huyghe and van Campen, 1991b] Huyghe, J. M. and van Campen, D. H. (1991b). Finite deformation theory of hierarchically arranged porous solids: II. Constitutive behaviour. Int. J. Engng Sci., 33(13):1861–1871.

[Ismail et al., 2013a] Ismail, M., Comerford, A., and Wall, W. (2013a). Coupled and reduced dimensional modeling of respiratory mechanics during spontaneous breathing. International Journal for Numerical Methods in Biomedical Engineering.

[Ismail et al., 2014] Ismail, M., Gravemeier, V., Comerford, A., and Wall, W. (2014). A stable approach for coupling multidimensional cardiovascular and pulmonary networks based on a novel pressure-flow rate or pressure-only neumann boundary condition formulation. International Journal For Numerical Methods in Biomedical Engineering, 30(4):447–469.

[Ismail et al., 2013b] Ismail, M., Wall, W. A., and Gee, M. W. (2013b). Adjoint-based inverse analysis of windkessel parameters for patient-specific vascular models. Journal of Computational Physics, 244:113–130.

[Jansen et al., 2000] Jansen, K., Whiting, C., and Hulbert, G. (2000). A generalized-[alpha] method for integrating the filtered Navier-Stokes equations with a stabilized finite element method. Computer Methods in Applied Mechanics and Engineering, 190(3-4):305 – 319.

[Jiang et al., 2005] Jiang, Y., Pjesivac-Grbovic, J., Cantrell, C., and Freyer, J. (2005). A multiscale model for avascular tumor growth. Biophys. J., 89(6):3884–94.

[Johnson et al., 2011] Johnson, D. A., Naik, U. P., and Beris, A. N. (2011). Efficient implementation of the proper outlet flow conditions in blood flow simulations through asymmetric arterial bifurcations. International Journal for Numerical Methods in Fluids, 66(11):1383–1408.

[Kamiya and Togawa, 1980] Kamiya, A. and Togawa, T. (1980). Adaptive regulation of wall shear stress to flow change in the canine carotid artery. American Journal of Physiology-Heart and Circulatory Physiology, 239(1):H14–H21.

[Kassab et al., 1999] Kassab, G. S., Le, K. N., and Fung, Y.-C. B. (1999). A hemodynamic analysis of coronary capillary blood flow based on anatomic and distensibility data. Am J Physiol Heart Circ Physiol, 277(6):H2158–2166.

[Katz et al., 2013] Katz, I., Pichelin, M., Caillibotte, G., Montesantos, S., Majoral, C., Martonen, T., Fleming, J., Bennett, M., and Conway, J. (2013). Controlled parametric individualized 2D and 3D imaging measurements of aerosol deposition in the respiratory tract of healthy human subjects preliminary comparisons with simulations. Aerosol Science & Technology, 47:714–723.

[Kheyfets et al., 2013] Kheyfets, V., O'Dell, W., Smith, T., Reilly, J., and Finol, E. (2013). Considerations for numerical modeling of the pulmonary circulation—a review with a focus on pulmonary hypertension. Journal of biomechanical engineering, 135(6):061011.

[Kim et al., 2009] Kim, H. J., Figueroa, C. A., Hughes, T. J. R., Jansen, K. E., and Taylor, C. A. (2009). Augmented lagrangian method for constraining the shape of velocity profiles at outlet boundaries for three-dimensional finite element simulations of blood flow. Computer Methods in Applied Mechanics and Engineering, 198(45-46):3551–3566.

[Kim et al., 2007] Kim, Y., Stolarska, M., and Othmer, H. (2007). A hybrid model for tumor spheroid growth *in vitro*. I. Theoretical development and early results. Math. Models Methods Appl. Sci., 17(suppl.):1773–1798.

[Koshiba et al., 2007] Koshiba, N., Ando, J., Chen, X., and Hisada, T. (2007). Multiphysics simulation of blood flow and LDL transport in a porohyperelastic arterial wall model. Journal of biomechanical engineering, 129:374.

[Ku et al., 2002] Ku, J. P., Draney, M. T., Arko, F. R., Lee, W. A., Chan, F. P., Pelc, N. J., Zarins, C. K., and Taylor, C. A. (2002). In vivo validation of numerical prediction of blood flow in arterial bypass grafts. Annals of Biomedical Engineering, 30(6):743–752.

[Ku et al., 2005] Ku, J. P., Elkins, C. J., and Taylor, C. A. (2005). Comparison of CFD and MRI flow and velocities in an in vitro large artery bypass graft model. Annals of biomedical engineering, 33(3):257–269.

[Kung et al., 2013] Kung, E., Baretta, A., Baker, C., Arbia, G., Biglino, G., Corsini, C., Schievano, S., Vignon-Clementel, I. E., Dubini, G., Pennati, G., Taylor, A., Dorfman, A., Hlavacek, A. M., Marsden, A. L., Hsia, T.-Y., and Migliavacca, F. (2013). Predictive modeling of the virtual Hemi-Fontan operation for second stage single ventricle palliation: two patient-specific cases. Journal of Biomechanics, 46(2):423–9.

[Kuprat et al., 2013] Kuprat, A. P., Kabilan, S., Carson, J. P., Corley, R. A., and Einstein, D. R. (2013). A bidirectional coupling procedure applied to multiscale respiratory modeling. Multi-scale Modeling and Simulation of Biological Systems, 244(0):148–167.

[Lagana et al., 2005] Lagana, K., Balossino, R., Migliavacca, F., Pennati, G., Bove, E., de Leval, M., and Dubini, G. (2005). Multiscale modeling of the cardiovascular system: application to the study of pulmonary and coronary perfusions in the univentricular circulation. Journal of Biomechanics, 38(5):1129 – 1141.

[Lagana et al., 2002] Lagana, K., Dubini, G., Migliavacca, F., Pietrabissa, R., Pennati, G., Veneziani, A., and Quarteroni, A. (2002). Multiscale modelling as a tool to prescribe realistic boundary conditions for the study of surgical procedures. Biorheology, 39(3-4):359–364.

[Lambert, 1958] Lambert, J. W. (1958). On the nonlinearities of fluid flow in nonrigid tubes. Journal of the Franklin Institute, 266(2):83–102.

[Lassau et al., 2011] Lassau, N., Chami, L., Chebil, M., Benatsou, B., Bidault, S., Girard, E., Abboud, G., and Roche, A. (2011). Dynamic contrast-enhanced ultrasonography (dce-us) and anti-angiogenic treatments. Discovery medicine, 11(56):18–24.

[Lassila et al., 2013] Lassila, T., Manzoni, A., Quarteroni, A., and Rozza, G. (2013). A reduced computational and geometrical framework for inverse problems in hemodynamics. Int. j. numer. method. biomed. eng., 29(7):741–776.

[Learoyd and Taylor, 1966] Learoyd, B. M. and Taylor, M. G. (1966). Alterations with age in the viscoelastic properties of human arterial walls. Circulation research, 18(3):278–292.

[Lee and Rieger, 2006] Lee, D.-S. and Rieger, H. (2006). Flow correlated percolation during vascular remodeling in growing tumors. Phys. Rev. Lett., 96(5):4.

[Lee and Langille, 1991] Lee, R. D. B. and Langille, B. L. (1991). Arterial adaptations to altered blood flow. Canadian journal of physiology and pharmacology, 69(7):978–983.

[Leiva et al., 2010] Leiva, J. S., Blanco, P. J., and Buscaglia, G. C. (2010). Iterative strong coupling of dimensionally heterogeneous models. International Journal for Numerical Methods in Engineering, 81(12):1558–1580.

[Levesque and Nerem, 1985] Levesque, M. and Nerem, R. (1985). The elongation and orientation of cultured endothelial cells in response to shear stress. Journal of biomechanical engineering, 107(4):341–347.

[Liang et al., 2014] Liang, F., Sughimoto, K., Matsuo, K., Liu, H., and Takagi, S. (2014). Patient-specific assessment of cardiovascular function by combination of clinical data and computational model with applications to patients undergoing Fontan operation. Int J Numer Method Biomed Eng, 30(10):1000–18.

[Lighthill, 1975] Lighthill, J. (1975). Mathematica biofluiddynamics. Society for Industrial & Applied Mathematics, US.

[Lindsey et al., 2014a] Lindsey, S. E., Butcher, J. T., and Yalcin, H. C. (2014a). Mechanical regulation of cardiac development. Frontiers in physiology, 5.

[Lindsey et al., 2014b] Lindsey, S. E., Menon, P. G., Kowalski, W. J., Shekhar, A., Yalcin, H. C., Nishimura, N., Schaffer, C. B., Butcher, J. T., and Pekkan, K. (2014b). Growth and hemodynamics after early embryonic aortic arch occlusion. Biomechanics and modeling in mechanobiology, pages 1–17.

[Lloyd-Jones et al., 2010] Lloyd-Jones, D., Adams, R. J., Brown, T. M., Carnethon, M., Dai, S., De Simone, G., Ferguson, T. B., Ford, E., Furie, K., Gillespie, C., et al. (2010). Heart disease and stroke statistics—2010 update a report from the american heart association. Circulation, 121(7):e46–e215.

[Lombardi, 2014] Lombardi, D. (2014). Inverse problems in 1D hemodynamics on systemic networks: A sequential approach. International Journal for Numerical Methods in Biomedical Engineering, 30(2):160–179.

[Longest et al., 2012] Longest, P. W., Tian, G., Walenga, R. L., and Hindle, M. (2012). Comparing MDI and DPI aerosol deposition using in vitro experiments and a new stochastic individual path (SIP) model of the conducting airways. Pharmaceutical Research, 29(6):1670–88.

[Longest and Vinchurkar, 2007] Longest, P. W. and Vinchurkar, S. (2007). Effects of mesh style and grid convergence on particle deposition in bifurcating airway models with comparisons to experimental data. Medical Engineering and Physics, 29(3):350–66.

[Loseille and Löhner, 2010] Loseille, A. and Löhner, R. (2010). Adaptive anisotropic simulations in aerodynamics. In 48th AIAA Aerospace Sciences Meeting and Exhibit, AIAA-2010-169, Orlando, FL, USA, page 170.

[L.Preziosi, 2003] L.Preziosi (2003). Cancer Modelling and Simulation. Chapman and Hall/CRC.

[Ma and Lutchen, 2009] Ma, B. and Lutchen, K. R. (2009). CFD simulation of aerosol deposition in an anatomically based human large-medium airway model. Annals of Biomedical Engineering, 37(2):271–85.

[Ma et al., 2009] Ma, B., Ruwet, V., Corieri, P., Theunissen, R., Riethmuller, M., and Darquenne, C. (2009). CFD Simulation and Experimental Validation of Fluid Flow and Particle Transport in a Model of Alveolated Airways. Journal of Aerosol Science, 40(5):403–141.

[Macklin et al., 2009] Macklin, P., McDougall, S., Anderson, A. R., Chaplain, M. A., Cristini, V., and Lowengrub, J. (2009). Multiscale modelling and nonlinear simulation of vascular tumour growth. J Math Biol, 58(4-5):765–98.

[Malossi et al., 2011] Malossi, A. C. I., Blanco, P. J., Deparis, S., and Quarteroni, A. (2011). Algorithms for the partitioned solution of weakly coupled fluid models for cardiovascular flows. International Journal for Numerical Methods in Biomedical Engineering, 27(12):2035–2057.

[Malve et al., 2013] Malve, M., Chandra, S., Lopez-Villalobos, J., Finol, E., Ginel, A., and Doblare, M. (2013). CFD analysis of the human airways under impedance- based boundary conditions: application to healthy, diseased and stented trachea. Computer Methods in Biomechanics and Biomedical Engineering, (March):37–41.

[Mantzaris et al., 2004] Mantzaris, N. V., Webb, S., and Othmer, H. G. (2004). Mathematical modeling of tumor-induced angiogenesis. J Math Biol, 49(2):111–87.

[Marmé and Adam, 2008] Marmé, D. and Adam, N. F. (2008). Tumor Angiogenesis. Springer-Verlag, Berlin Heidelberg.

[Marsden et al., 2008] Marsden, A., Feinstein, J., and Taylor, C. (2008). A computational framework for derivative-free optimization of cardiovascular geometries. Computer Methods in Applied Mechanics and Engineering, 197(21-24):1890 – 1905.

[Marsden et al., 2009] Marsden, A. L., Bernstein, A. J., Reddy, V. M., Shadden, S. C., Spilker, R. L., Chan, F. P., Taylor, C. A., and Feinstein, J. A. (2009). Evaluation of a novel Y-shaped extracardiac Fontan baffle using computational fluid dynamics. The Journal of Thoracic and Cardiovascular Surgery, 137(2):394–403.

[Martin et al., 2015] Martin, M., Feinstein, J., Chan, F., Marsden, A., Yang, W., and Reddy, V. (2015). Technical feasibility and intermediate outcomes of a hand-crafted, area-preserving, bifurcated "Y-Graft" Fontan. Journal of Thoracic and Cardiovascular Surgery, 149(1):247–255.

[Martin and Maury, 2013] Martin, S. and Maury, B. (2013). Modeling of the oxygen transfer in the respiratory process. ESAIM: Mathematical Modelling and Numerical Analysis, 47(04):935–960.

[Maury, 2013] Maury, B. (2013). The respiratory system in equations, volume 7. Springer Science; Business Media.

[Maury, 2014] Maury, B. (2014). The resistance of the respiratory system, from top to bottom. ESAIM: Proceedings and Surveys, 47:75–96.

[Maury et al., 2005] Maury, B., Meunie, N., Soualah, A., and Vial, L. (2005). Outlet dissipative conditions for air flow in the bronchial tree. ESAIM: Proc., 14:201–212.

[Maxey and Riley, 1983] Maxey, M. R. and Riley, J. J. (1983). Equation of motion for a small rigid sphere in nonuniform flow.pdf. Physics of Fluids, 26:883–889.

[May-Newman et al., 2001] May-Newman, K., Chen, C., Oka, R., Haslim, R., and DeMaria, A. (2001). Evaluation of myocardial perfusion using three-dimensional myocardial contrast echocardiography. In Nuclear Science Symposium Conference Record, 2001 IEEE, volume 3, pages 1691–1694 vol.3.

[May-Newman and McCulloch, 1998] May-Newman, K. and McCulloch, A. D. (1998). Homogenization modeling for the mechanics of perfused myocardium. Progress in Biophysics & Molecular Biology, 69:463–481.

[McDougall et al., 2006] McDougall, S. R., Anderson, A. R., and Chaplain, M. A. (2006). Mathematical modelling of dynamic adaptive tumour-induced angiogenesis: Clinical implications and therapeutic targeting strategies. J Theor Biol, 241(3):564–89.

[Migliavacca et al., 2006] Migliavacca, F., Balossino, R., Pennati, G., Dubini, G., Hsia, T. Y., de Leval, M. R., and Bove, E. L. (2006). Multiscale modelling in biofluidynamics: Application to reconstructive paediatric cardiac surgery. Journal of Biomechanics, 39(6):1010–1020.

[Migliavacca et al., 2001] Migliavacca, F., Pennati, G., Dubini, G., Fumero, R., Pietrabissa, R., Urcelay, G., Bove, E. L., Hsia, T.-Y., and de Leval, M. R. (2001). Modeling of the norwood circulation: effects of shunt size, vascular resistances, and heart rate. American Journal of Physiology - Heart and Circulatory Physiology, 280(5):H2076–H2086.

[Milner et al., 1998] Milner, J. S., Moore, J. A., Rutt, B. K., and Steinman, D. A. (1998). Hemodynamics of human carotid artery bifurcations: computational studies with models reconstructed from magnetic resonance imaging of normal subjects. Journal of vascular surgery, 28(1):143–156.

[Minard et al., 2012] Minard, K. R., Kuprat, A. P., Kabilan, S., Jacob, R. E., Einstein, D. R., Carson, J. P., and Corley, R. A. (2012). Phase-contrast MRI and CFD modeling of apparent (3)He gas flow in rat pulmonary airways. Journal of Magnetic Resonance, 221:129–138.

[Moireau et al., 2013] Moireau, P., Bertoglio, C., Xiao, N., Figueroa, C. A., Taylor, C. A., Chapelle, D., and Gerbeau, J. F. (2013). Sequential identification of boundary support parameters in a fluid-structure vascular model using patient image data. Biomechanics and Modeling in Mechanobiology, 12(3):475–496.

[Moireau et al., 2012] Moireau, P., Xiao, N., Astorino, M., Figueroa, C. A., Chapelle, D., Taylor, C. A., and Gerbeau, J.-F. (2012). External tissue support and fluid–structure simulation in blood flows. Biomechanics and modeling in mechanobiology, 11(1-2):1–18.

[Monjezi et al., 2012] Monjezi, M., Dastanpour, R., Saidi, M., and a.R. Pishevar (2012). Prediction of particle deposition in the respiratory track using 3D–1D modeling. Scientia Iranica, 19(6):1479–1486.

[Moore et al., 1999] Moore, J. A., Rutt, B. K., Karlik, S. J., Yin, K., and Ethier, C. R. (1999). Computational blood flow modeling based on in vivo measurements. Annals of biomedical engineering, 27(5):627–640.

[Mueller-Klieser, 1987] Mueller-Klieser, W. (1987). A review on cellular aggregates in cancer research. Cancer Res. Clin. Oncol., 113(2):101–122.

[Muller et al., 2005] Muller, J., Sahni, O., Li, X., Jansen, K. E., Shephard, M. S., and Taylor, C. A. (2005). Anisotropic adaptive finite element method for modelling blood flow. Computer Methods in Biomechanics and Biomedical Engineering, 8(5):295–305.

[Mylavarapu et al., 2009] Mylavarapu, G., Murugappan, S., Mihaescu, M., Kalra, M., Khosla, S., and Gutmark, E. (2009). Validation of computational fluid dynamics methodology used for human upper airway flow simulations. Journal of Biomechanics, 42(10):1553–1559.

[Nichols et al., 2011] Nichols, W., O'Rourke, M., and Vlachopoulos, C. (2011). McDonald's blood flow in arteries: theoretical, experimental and clinical principles. CRC Press.

[Nomura-Kitabayashi et al., 2009] Nomura-Kitabayashi, A., Phoon, C. K., Kishigami, S., Rosenthal, J., Yamauchi, Y., Abe, K., Yamamura, K.-i., Samtani, R., Lo, C. W., and Mishina, Y. (2009). Outflow tract cushions perform a critical valve-like function in the early embryonic heart requiring bmpria-mediated signaling in cardiac neural crest. American Journal of Physiology-Heart and Circulatory Physiology, 297(5):H1617–H1628.

[Nowak et al., 2003] Nowak, N., Kakade, P. P., and Annapragada, A. V. (2003). Computational Fluid Dynamics Simulation of Airflow and Aerosol Deposition in Human Lungs. Annals of Biomedical Engineering, 31(4):374–390.

[Oakes et al., 2014] Oakes, J. M., Breen, E., Scadeng, M., Tchantchou, G. S., and Darquenne, C. (2014). MRI-based measurements of aerosol deposition in the lung of healthy and elastase-treated rats. Journal of Applied Physiology, 116:1561–1568.

[Oakes et al., 2010] Oakes, J. M., Day, S., Weinstein, S. J., and Robinson, R. J. (2010). Flow field analysis in expanding healthy and emphysematous alveolar models using particle image velocimetry. Journal of Biomechanical Engineering, 132(2):021008.

[Oakes et al., 2012] Oakes, J. M., Scadeng, M., Breen, E. C., Marsden, A. L., and Darquenne, C. (2012). Rat airway morphometry measured from in situ mri-based geometric models. Journal of Applied Physiology, 112(11):1921–1931.

[Oakes et al., 2013] Oakes, J. M., Scadeng, M., Breen, E. C., Prisk, G. K., and Darquenne, C. (2013). Regional Distribution of Aerosol Deposition in Rat Lungs Using Magnetic Resonance Imaging. Annals of Biomedical Engineering, 41:967–978.

[O'Connor et al., 2011] O'Connor, J., Tofts, P., Miles, K., Parkes, L., Thompson, G., and Jackson, A. (2011). Dynamic contrast-enhanced imaging techniques: Ct and mri. The British journal of radiology, 84(Spec Iss 2):S112–20.

[Olufsen, 1999] Olufsen, M. S. (1999). Structured tree outflow condition for blood flow in larger systemic arteries. American journal of physiology-Heart and circulatory physiology, 276(1):H257–H268.

[Olufsen et al., 2012] Olufsen, M. S., Hill, N., Vaughan, G. D., Sainsbury, C., and Johnson, M. (2012). Rarefaction and blood pressure in systemic and pulmonary arteries. Journal of fluid mechanics, 705:280–305.

[Olufsen et al., 2000] Olufsen, M. S., Peskin, C. S., Kim, W. Y., Pedersen, E. M., Nadim, A., and Larsen, J. (2000). Numerical simulation and experimental validation of blood flow in arteries with structured-tree outflow conditions. Annals of biomedical engineering, 28(11):1281–1299.

[Oshima et al., 2012] Oshima, M., Torii, R., Tokuda, S., Yamada, S., and Koizumi, A. (2012). Patient-specific modeling and multi-scale blood simulation for computational hemodynamic study on the human cerebrovascular system. Current Pharmaceutical Biotechnology, 13(11):2153–2165.

[Oshinski et al., 1995] Oshinski, J. N., Ku, D. N., and Pettigrew, R. I. (1995). Turbulent fluctuation velocity: The most significant determinant of signal loss in stenotic vessels. Magnetic Resonance in Medicine, 33(2):193–199.

[Ottesen et al., 2013] Ottesen, J. T., Novak, V., and Olufsen, M. S. (2013). Development of patient specific cardiovascular models predicting dynamics in response to orthostatic stress challenges. In Batzel, J., Bachar, M., and Kappel, F., editors, MATHEMATICAL MODELING AND VALIDATION IN PHYSIOLOGY: APPLICATIONS TO THE

CARDIOVASCULAR AND RESPIRATORY SYSTEMS, volume 2064 of Lecture Notes in Mathematics, pages 177–213.

[Owen et al., 2009] Owen, M. R., Alarcón, T., Maini, P. K., and Byrne, H. M. (2009). Angiogenesis and vascular remodelling in normal and cancerous tissues. J Math Biol, 58(4-5):689–721.

[Palmowski et al., 2008] Palmowski, M., Huppert, J., Ladewig, G., Hauff, P., Reinhardt, M., Mueller, M. M., Woenne, E. C., Jenne, J. W., Maurer, M., Kauffmann, G. W., et al. (2008). Molecular profiling of angiogenesis with targeted ultrasound imaging: early assessment of antiangiogenic therapy effects. Molecular Cancer Therapeutics, 7(1):101–109.

[Passerini et al., 2013] Passerini, T., Quaini, A., Villa, U., Veneziani, A., and Canic, S. (2013). Validation of an open source framework for the simulation of blood flow in rigid and deformable vessels. International journal for numerical methods in biomedical engineering, 29(11):1192–1213.

[Patan, 2004] Patan, S. (2004). Vasculogenesis and angiogenesis. In Angiogenesis in brain tumors, pages 3–32. Springer.

[Pedley, 1980] Pedley, T. (1980). The fluid dynamics of large blood vessels. Cambridge University Press, Cambridge, UK.

[Pedley et al., 1996] Pedley, T. J., Brook, B. S., and Seymour, R. S. (1996). Blood pressure and flow rate in the giraffe jugular vein. Philosophical Transactions of the Royal Society B: Biological Sciences, 351(1342):855–866.

[Peeters et al., 2015] Peeters, G., Debbaut, C., Cornillie, P., De Schryver, T., Monbaliu, D., Laleman, W., and Segers, P. (2015). A multilevel modeling framework to study hepatic perfusion characteristics in case of liver cirrhosis. Journal of biomechanical engineering, 137(5):051007.

[Peiró and Veneziani, 2009] Peiró, J. and Veneziani, A. (2009). Reduced models of the cardiovascular system. In Cardiovascular mathematics, pages 347–394. Springer.

[Pekkan et al., 2005] Pekkan, K., De Zelicourt, D., Ge, L., Sotiropoulos, F., Frakes, D., Fogel, M. A., and Yoganathan, A. P. (2005). Physics-driven CFD modeling of complex anatomical cardiovascular flows - A TCPC case study. Annals of Biomedical Engineering, 33(3):284–300.

[Pennati et al., 2011] Pennati, G., Corsini, C., Cosentino, D., Hsia, T.-Y., Luisi, V. S., Dubini, G., and Migliavacca, F. (2011). Boundary conditions of patient-specific fluid dynamics modelling of cavopulmonary connections: possible adaptation of pulmonary resistances results in a critical issue for a virtual surgical planning. Interface Focus, 1(3):297–307.

[Perktold and Rappitsch, 1995] Perktold, K. and Rappitsch, G. (1995). Computer simulation of local blood flow and vessel mechanics in a compliant carotid artery bifurcation model. Journal of biomechanics, 28(7):845–856.

[Pontrelli, 2002] Pontrelli, G. (2002). A mathematical model of flow in a liquid-filled viscoelastic tube. Medical and Biological Engineering and Computing, 40(5):550–556.

[Pope et al., 2009] Pope, S. R., Ellwein, L. M., Zapata, C. L., Novak, V., Kelley, C. T., and Olufsen, M. S. (2009). Estimation and identification of parameters in a lumped cerebrovascular model. Math Biosci Eng, 6(1):93–115.

[Porpora et al., 2012] Porpora, A., Zunino, P., Vergara, C., and Piccinelli, M. (2012). Numerical treatment of boundary conditions to replace lateral branches in hemodynamics. International Journal for Numerical Methods in Biomedical Engineering, 28(12):1165–1183.

[Pradat et al., 2003] Pradat, P., Francannet, C., Harris, J., and Robert, E. (2003). The epidemiology of cardiovascular defects, part i: a study based on data from three large registries of congenital malformations. Pediatric cardiology, 24(3):195–221.

[Prasad et al., 2011] Prasad, A., To, L. K., Gorrepati, M. L., Zarins, C. K., and Figueroa, C. A. (2011). Computational analysis of stresses acting on intermodular junctions in thoracic aortic endografts. Journal of Endovascular Therapy, 18(4):559–568.

[Prasad et al., 2013] Prasad, A., Xiao, N., Gong, X.-Y., Zarins, C. K., and Figueroa, C. A. (2013). A computational framework for investigating the positional stability of aortic endografts. Biomechanics and modeling in mechanobiology, 12(5):869–887.

[Preziosi and Tosin, 2009] Preziosi, L. and Tosin, A. (2009). Multiphase modelling of tumour growth and extracellular matrix interaction: Mathematical tools and applications. J Math Biol, 58(4-5):625–56.

[Quarteroni et al., 2001] Quarteroni, A., Ragni, S., and Veneziani, A. (2001). Coupling between lumped and distributed models for blood flow problems. Computing and Visualization in Science, 4:111–124.

[Quarteroni et al., 2000] Quarteroni, A., Tuveri, M., and Veneziani, A. (2000). Computational vascular fluid dynamics: problems, models and methods. Computing and Visualization in Science, 2(4):163–197.

[Quarteroni and Veneziani, 2003] Quarteroni, A. and Veneziani, A. (2003). Analysis of a geometrical multiscale model based on the coupling of ODEs and PDEs for blood flow simulations. Multiscale Model Simul., 1(2):173–195.

[Raabe et al., 1975] Raabe, O. G., Yeh, H. C., Newton, G. J., Phalen, R. F., and Velasquez, D. J. (1975). Deposition of inhaled monodisperse aerosols in small rodents. Inhaled Particles, 4(1):3 – 21.

[Radaellia et al., 2008] Radaellia, A. G., Augsburger, L., Cebral, J. R., Ohta, M., Ruefenacht, D. A., Balossino, R., Benndorf, G., Hose, D. R., Marzo, A., Metcalfe, R., Mortier, P., Mut, F., Reymond, P., Socci, L., Verhegghe, B., and Frangi, A. F. (2008). Reproducibility of haemodynamical simulations in a subject-specific stented aneurysm model - a report on the virtual intracranial stenting challenge 2007. Journal of Biomechanics, 41(10):2069–2081.

[Radszuweit et al., 2009] Radszuweit, M., Block, M., Hengstler, J., Schoell, E., and Drasdo, D. (2009). Comparing the growth kinetics of cell populations in two and three dimensions. submitted.

[Revie et al., 2013] Revie, J. A., Stevenson, D. J., Chase, J. G., Hann, C. E., Lambermont, B. C., Ghuysen, A., Kolh, P., Shaw, G. M., Heldmann, S., and Desaive, T. (2013). Validation of subject-specific cardiovascular system models from porcine measurements. Computer methods and programs in biomedicine, 109(2):197–210.

[Ribatti et al., 2003] Ribatti, D., Vacca, A., and Dammacco, F. (2003). New non-angiogenesis dependent pathways for tumour growth. Eur J Cancer, 39(13):1835–41.

[Roose et al., 2007] Roose, T., Chapman, S., and Maini, P. (2007). Mathematical models of avascular tumour growth: a review. SIAM Review, 49(2):179–208.

[Rubini et al., 2011] Rubini, A., Carniel, E. L., Parmagnani, A., and Natali, A. N. (2011). Flow and volume dependence of rat airway resistance during constant flow inflation and deflation. Lung, 189(6):511–8.

[Sahni et al., 2006] Sahni, O., Muller, J., Jansen, K., Shephard, M., and Taylor, C. (2006). Efficient anisotropic adaptive discretization of the cardiovascular system. Computer Methods in Applied Mechanics and Engineering, 195:5634–5655.

[Sainte-Marie et al., 2006] Sainte-Marie, J., Chapelle, D., Cimrman, R., and Sorine, M. (2006). Modeling and estimation of the cardiac electromechanical activity. Computers & Structures, 84:1743–1759.

[Sanchez et al., 2014] Sanchez, M., Ecker, O., Ambard, D., Jourdan, F., Nicoud, F., Mendez, S., Lejeune, J.-P., Thines, L., Dufour, H., Brunel, H., et al. (2014). Intracranial aneurysmal pulsatility as a new individual criterion for rupture risk evaluation: Biomechanical and numeric approach (irras project). American Journal of Neuroradiology, 35(9):1765–1771.

[Sani et al., 2006] Sani, R. L., Shen, J., Pironneau, O., and Gresho, P. M. (2006). Pressure boundary condition for the time-dependent incompressible Navier-Stokes equations. International Journal for Numerical Methods in Fluids, 50(6):673–682.

[Sankaran et al., 2015] Sankaran, S., Grady, L., and Taylor, C. (2015). Fast computation of hemodynamic sensitivity to lumen segmentation uncertainty.

[Schaller and Meyer-Hermann, 2005] Schaller, G. and Meyer-Hermann, M. (2005). Multicellular tumor spheroid in an off-lattice voronoi-delaunay cell model. Phys. Rev., 71:051910–1 – 051910–16.

[Schiffer et al., 2003] Schiffer, I., Gebhard, S., Heimerdinger, C., Heling, A., Hast, J., Wollscheid, U., Seliger, B., Tanner, B., Gilbert, S., Beckers, T., Baasner, S., Brenner, W., Spangenberg, C., Prawitt, D., Trost, T., Schreiber, W., Zabel, B., Thelen, M., Lehr, H., Oesch, F., and Hengstler, J. (2003). Switching off her-2/neu in a tetracycline-controlled mouse tumor model leads to apoptosis and tumor-size-dependent remission. Cancer Res., 63:7221–7231.

[Schmid et al., 2008] Schmid, O., Bolle, I., Harder, V., Karg, E., Takenaka, S., Schulz, H., and Ferron, G. A. (2008). Model for the deposition of aerosol particles in the respiratory tract of the rat. I. Nonhygroscopic particle deposition. Journal of Aerosol Medicine and Pulmonary Drug Delivery, 21(3):291–307.

[Schmidt et al., 2008] Schmidt, J. P., Delp, S. L., Sherman, M. A., Taylor, C. A., Pande, V. S., and Altman, R. B. (2008). The simbios national center: Systems biology in motion. Proc IEEE Inst Electr Electron Eng, 96(8):1266.

[Segal et al., 2002] Segal, R. A., Martonen, T. B., Kim, C. S., and Shearer, M. (2002). Computer simulations of particle deposition in the lungs of chronic obstructuve pulmonary disease patients. Inhalation Toxicology, 14:705–720.

[Segers et al., 2008] Segers, P., Rietzschel, E., De Buyzere, M., Stergiopulos, N., Westerhof, N., Van Bortel, L., Gillebert, T., and Verdonck, P. (2008). Three-and four-element windkessel models: assessment of their fitting performance in a large cohort of healthy middle-aged individuals. Proceedings of the Institution of Mechanical Engineers, Part H: Journal of Engineering in Medicine, 222(4):417–428.

[Shandas, 2002] Shandas, R. (2002). Designing the optimal total cavopulmonary connection: pulsatile versus steadyflow experiments. Medical Science Monitor, 8(3):MT41–MT45.

[Sherwin et al., 2003a] Sherwin, S., Formaggia, L., Peiro, J., and Franke, V. (2003a). Computational modelling of 1d blood flow with variable mechanical properties and its application to the simulation of wave propagation in the human arterial system. International Journal for Numerical Methods in Fluids, 43(6-7):673–700.

[Sherwin et al., 2003b] Sherwin, S., Franke, V., Peiró, J., and Parker, K. (2003b). One-dimensional modelling of a vascular network in space-time variables. Journal of Engineering Mathematics, 47(3-4):217–250.

[Smith, 2004] Smith, N. (2004). A computational study of the interaction between coronary blood flow and myocardial mechanics. Physiological Measurement, 25(4):863–877.

[Smith and Kassab, 2001] Smith, N. and Kassab, G. (2001). Analysis of coronary blood flow interaction with myocardial mechanics based on anatomical models. Phil. Trans. R. Soc. Lond. A, 359:1251–1262.

[Smith et al., 2002] Smith, N., Pullan, A., and Hunter, P. J. (2002). An anatomically based model of transient coronary blood flow in the heart. SIAM Journal on Applied mathematics, 62(3):990–1018.

[Spaan et al., 2008] Spaan, J., Kolyva, C., van den Wijngaard, J., ter Wee, R., van Horssen, P., Piek, J., and Siebes, M. (2008). Coronary structure and perfusion in health and disease. Philosophical Transactions of the Royal Society A, 366(1878):3137–3153.

[Spilker et al., 2007] Spilker, R., Feinstein, J., Parker, D., Reddy, V., and Taylor, C. (2007). Morphometry-based impedance boundary conditions for patient-specific modeling of blood flow in pulmonary arteries. Annals of Biomedical Engineering, 35(4):546–559.

[Spilker and Taylor, 2010] Spilker, R. and Taylor, C. (2010). Tuning multidomain hemodynamic simulations to match physiological measurements. Annals of Biomedical Engineering, 38(8):2635–2648.

[Steele et al., 2007] Steele, B. N., Olufsen, M. S., and Taylor, C. A. (2007). Fractal network model for simulating abdominal and lower extremity blood flow during resting and exercise conditions. Computer Methods in Biomechanics and Biomedical Engineering, 10(1):39–51.

[Steinman et al., 2013] Steinman, D. A., Hoi, Y., Fahy, P., Morris, L., Walsh, M. T., Aristokleous, N., Anayiotos, A. S., Papaharilaou, Y., Arzani, A., Shadden, S. C., Berg, P., Janiga, G., Bols, J., Segers, P., Bressloff, N. W., Cibis, M., Gijsen, F. H., Cito, S., Pallares, J., Browne, L. D., Costelloe, J. A., Lynch, A. G., Degroote, J., Vierendeels, J., Fu, W., Qiao, A., Hodis, S., Kallmes, D. F., Kalsi, H., Long, Q., Kheyfets, V. O., Finol, E. A., Kono, K., Malek, A. M., Lauric, A., Menon, P. G., Pekkan, K., Moghadam, M. E., Marsden, A. L., Oshima, M., Katagiri, K., Peiffer, V., Mohamied, Y., Sherwin, S. J., Schaller, J., Goubergrits, L., Usera, G., Mendina, M., Valen-Sendstad, K., Habets, D. F., Xiang, J., Meng, H., Yu, Y., Karniadakis, G. E., Shaffer, N., and Loth, F. (2013). Variability of computational fluid dynamics solutions for pressure and flow in a giant aneurysm: The ASME 2012 Summer Bioengineering Conference CFD Challenge. Journal of Biomechanical Engineering-Transactions of the Asme, 135(2).

[Stergiopulos et al., 1999] Stergiopulos, N., Westerhof, B., and Westerhof, N. (1999). Total arterial inertance as the fourth element of the windkessel model. Am. J. Physiol., 276:H81–H88.

[Stergiopulos et al., 1992] Stergiopulos, N., Young, D. F., and Rogge, T. R. (1992). Computer simulation of arterial flow with applications to arterial and aortic stenoses. Journal of Biomechanics, 25:1477–1488.

[Stewart, 2008] Stewart, S. (2008). Computer methods in cardiovascular device design & evaluation: overview of regulatory best practices.

[Stuhne and Steinman, 2004] Stuhne, G. R. and Steinman, D. A. (2004). Finite-element modeling of the hemodynamics of stented aneurysms. Journal of biomechanical engineering, 126(3):382–387.

[Sturm and Hofmann, 2004] Sturm, R. and Hofmann, W. (2004). Stochastic simulation of alveolar particle deposition in lungs affected by different types of emphysema. Journal of Aerosol Medicine, 17(4):357–72.

[Suga and Sagawa, 1974] Suga, H. and Sagawa, K. (1974). Instantaneous pressure-volume relationships and their ratio in the excised, supported canine left ventricle. Circulation research, 35(1):117–126.

[Sughimoto et al., 2013] Sughimoto, K., Liang, F., Takahara, Y., Mogi, K., Yamazaki, K., Takagi, S., and Liu, H. (2013). Assessment of cardiovascular function by combining clinical data with a computational model of the cardiovascular system. The Journal of thoracic and cardiovascular surgery, 145(5):1367–1372.

[Sweeney et al., 1987] Sweeney, T. D., Brain, J. D., Leavitt, S. a., and Godleski, J. J. (1987). Emphysema alters the deposition pattern of inhaled particles in hamsters. The American journal of Pathology, 128:19–28.

[Tahk and Speyer, 1990] Tahk, M. and Speyer, J. L. (1990). Target tracking problems subject to kinematic constraints. Automatic Control, IEEE Transactions on, 35(3):324–326.

[Taulbee and Yu, 1975] Taulbee, D. B. and Yu, C. P. (1975). A theory of aerosol deposition in the human respiratory tract. Journal of applied physiology, 38(1):77–85.

[Taylor et al., 1998a] Taylor, C., Hughes, T. J., and Zarins, C. K. (1998a). Finite element modeling of three-dimensional pulsatile flow in the abdominal aorta: relevance to atherosclerosis. Annals of Biomedical Engineering, 26(6):975–87.

[Taylor and Figueroa, 2009] Taylor, C. A. and Figueroa, C. A. (2009). Patient-Specific Modeling of Cardiovascular Mechanics, volume 11 of Annual Review of Biomedical Engineering, pages 109–134. Annual Reviews, Palo Alto.

[Taylor et al., 1998b] Taylor, C. A., Hughes, T. J. R., and Zarins, C. K. (1998b). Finite element modeling of blood flow in arteries. Computer Methods in Applied Mechanics and Engineering, 158(1-2):155–196.

[Taylor and Steinman, 2010] Taylor, C. A. and Steinman, D. A. (2010). Image-based modeling of blood flow and vessel wall dynamics: Applications, methods and future directions. Annals of Biomedical Engineering, 38(3):1188–1203.

[Terzaghi, 1943] Terzaghi, K. (1943). Theoretical Soil Mechanics. John Wiley and Sons, New-York.

[Tezduyar et al., 2008] Tezduyar, T., Ramakrishnan, S., and Sathe, S. (2008). Stabilized formulations for incompressible flows with thermal coupling. International Journal for Numerical Methods in Fluids, 57:1189–1209.

[Tezduyar et al., 2010] Tezduyar, T., Takizawa, K., Moorman, C., Wright, S., and Christopher, J. (2010). Space-time finite element computation of complex fluid-structure interactions. International Journal for Numerical Methods in Fluids, 64:1201–1218.

[Thomaseth and Cobelli, 1999] Thomaseth, K. and Cobelli, C. (1999). Generalized sensitivity functions in physiological system identification. Annals of Biomedical Engineering, 27(5):607–616.

[Thurlbeck and Muller, 1994] Thurlbeck, W. M. and Muller, N. L. (1994). Emphysema: Definition, Imaging, and Quantification. American Journal of Roentgenology, 163:1017–1025.

[Torii et al., 2006] Torii, R., Oshima, M., Kobayashi, T., Takagi, K., and Tezduyar, T. E. (2006). Computer modeling of cardiovascular fluid–structure interactions with the deforming-spatial-domain/stabilized space–time formulation. Computer Methods in Applied Mechanics and Engineering, 195(13):1885–1895.

[Urquiza et al., 2006] Urquiza, S., Blanco, P., Vénere, M., and Feijoo, R. (2006). Multidimensional modelling for the carotid artery blood flow. Computer Methods in Applied Mechanics and Engineering, 195(33-36):4002 – 4017.

[Valdez-Jasso et al., 2009] Valdez-Jasso, D., Haider, M., Banks, H., Santana, D. B., Germán, Y. Z., Armentano, R. L., Olufsen, M. S., et al. (2009). Analysis of viscoelastic wall properties in ovine arteries. Biomedical Engineering, IEEE Transactions on, 56(2):210–219.

[van Ertbruggen et al., 2009] van Ertbruggen, C., Corieri, P., Theunissen, R., Riethmuller, M. L., and Darquenne, C. (2009). Validation of CFD Predictions of Flow in a 3D Alveolated Bend with Experimental Data. Journal of Biomechanics, 41(2):399–405.

[Vankan et al., 1997] Vankan, W., Huyghe, J., Janssen, J., and Huson, A. (1997). A finite element mixture model for hierarchical porous media. Int. J. Numer. Meth. Engng., 40:193–210.

[Vaupel, 2004] Vaupel, P. (2004). Tumor microenvironmental physiology and its implications for radiation oncology. Semin Radiat Oncol, 14(3):198–206.

[Veneziani and Vergara, 2005] Veneziani, A. and Vergara, C. (2005). Flow rate defective boundary conditions in haemodynamics simulations. International Journal for Numerical Methods in Fluids, 47:803–816.

[Vuong et al., 2015] Vuong, A.-T., Yoshihara, L., and Wall, W. (2015). A general approach for modeling interacting flow through porous media under finite deformations. Computer Methods in Applied Mechanics and Engineering, 283:1240–1259.

[Walters and Luke, 2011] Walters, D. K. and Luke, W. H. (2011). Computational fluid dynamics simulations of particle deposition in large-scale, multigenerational lung models. Journal of Biomechanical Engineering, 133(1):011003.

[Wan et al., 2002] Wan, J., Steele, B., Spicer, S. A., Strohband, S., Feijo´ o, G. R., Hughes, T. J., and Taylor, C. A. (2002). A one-dimensional finite element method for simulation-based medical planning for cardiovascular disease. Computer Methods in Biomechanics & Biomedical Engineering, 5(3):195–206.

[Wang et al., 2015] Wang, X., Fullana, J.-M., and Lagrée, P.-Y. (2015). Verification and comparison of four numerical schemes for a 1d viscoelastic blood flow model. Computer methods in biomechanics and biomedical engineering, 18(15):1704–1725.

[Ward and King, 1997] Ward, J. and King, J. (1997). Mathematical modelling of avascular-tumor growth. IMA J. Math. App. Med. Biol., 14:39–69.

[Welter et al., 2008] Welter, M., Bartha, K., and Rieger, H. (2008). Emergent vascular network inhomogeneities and resulting blood flow patterns in a growing tumor. J Theor Biol, 250(2):257–80.

[Westerhof et al., 2006] Westerhof, N., Boer, C., Lamberts, R. R., and Sipkema, P. (2006). Cross-Talk Between Cardiac Muscle and Coronary Vasculature. Physiol. Rev., 86(4):1263–1308.

[Wichers et al., 2006] Wichers, L. B., Rowan, W. H., Nolan, J. P., Ledbetter, A. D., McGee, J. K., Costa, D. L., and Watkinson, W. P. (2006). Particle deposition in spontaneously hypertensive rats exposed via whole-body inhalation: measured and estimated dose. Toxicological Sciences, 93(2):400–10.

[Wise et al., 2008] Wise, S. M., Lowengrub, J. S., Frieboes, H. B., and Cristini, V. (2008). Three-dimensional multispecies nonlinear tumor growth–i model and numerical method. J Theor Biol, 253(3):524–43.

[Wolinsky and Glagov, 1969] Wolinsky, H. and Glagov, S. (1969). Comparison of abdominal and thoracic aortic medial structure in mammals. Circulation Research, 25(6):677–686.

[Womersley, 1955] Womersley, J. R. (1955). Xxiv. oscillatory motion of a viscous liquid in a thin-walled elastic tube—i: The linear approximation for long waves. The London, Edinburgh, and Dublin Philosophical Magazine and Journal of Science, 46(373):199–221.

[Wongviriyawong et al., 2013] Wongviriyawong, C., Harris, R. S., Greenblatt, E., Winkler, T., and Venegas, J. G. (2013). Peripheral resistance: a link between global airflow obstruction and regional ventilation distribution. Journal of Applied Physiology, 114(4):504–514.

[Xiao et al., 2014] Xiao, N., Alastruey, J., and Alberto Figueroa, C. (2014). A systematic comparison between 1-D and 3-D hemodynamics in compliant arterial models. International Journal for Numerical Methods in Biomedical Engineering, 30(2):204–231.

[Yang and Smolinski, 2006] Yang, Z. and Smolinski, P. (2006). Dynamic finite element modeling of poroviscoelastic soft tissue. Computer Methods in Biomechanics and Biomedical Engineering, 9(1):7–16.

[Yashiro et al., 2007] Yashiro, K., Shiratori, H., and Hamada, H. (2007). Haemodynamics determined by a genetic programme govern asymmetric development of the aortic arch. Nature, 450(7167):285–288.

[Zhang and Kleinstreuer, 2001] Zhang, Z. and Kleinstreuer, C. (2001). Effect of particle inlet distribution in a triple bifurcation lung airway model. Journal of Aerosol Medicine, 14(1):13–29.

[Zinemanas et al., 1995] Zinemanas, D., Beyar, R., and Sideman, S. (1995). An integrated model of LV muscle mechanics, coronary flow, and fluid and mass transport. Am J Physiol Heart Circ Physiol, 268(2):H633–645.